NMR AND TRANSPORT MEASUREMENTS OF COPPER CHALCOGENIDE AND CLATHRATE COMPOUNDS

A Dissertation

by

ALI SIRUSI ARVIJ

Submitted to the Office of Graduate and Professional Studies of
Texas A&M University
in partial fulfillment of the requirements for the degree of

DOCTOR OF PHILOSOPHY

Chair of Committee,	Joseph H. Ross, Jr.
Committee Members,	Donald G. Naugle
	Artem G. Abanov
	Raymundo Arróyave
Head of Department,	Peter McIntyre

December 2016

Major Subject: Physics

ABSTRACT

Due to limited sources of fossil fuels worldwide and a large percentage wasted as heat energy, searching for efficient thermoelectric materials to convert heat to electricity has gained a great deal of attention. Most of the attempts are focused on materials with substantially lower lattice thermal conductivity and narrow band gaps. Among them, inorganic clathrates and copper-based chalcogenides possess intrinsic low thermal conductivity which makes them promising thermoelectrics. In this work, nuclear magnetic resonance (NMR), transport, and magnetic measurements were performed on clathrates and copper-based chalcogenides to investigate their vibrational and electronic charge carrier properties, as well as the unknown structures of Cu_2Se and Cu_2Te at low temperatures, and the effect of rattling of guest atoms in the clathrates. The NMR results in $Ba_8Ga_{16}Ge_{30}$ indicate a pseudogap in the Ga electronic density of states, superposed upon a surprisingly large Ba contribution to the conduction band. Meanwhile, the phonon contributions to the Ga relaxation rates are large and increase more rapidly with temperature than typical semiconductors due to enhanced anharmonicity of the propagative phonon modes over a wide range. Moreover, the observed NMR shifts in the $Ba_8Cu_5Si_xGe_{41-x}$ clathrates change in a nonlinear way with increasing Si substitution: from $x = 0$ to about 20 the shifts are essentially constant, while approaching $x = 41$ they increase rapidly, demonstrating a significant change in hybridizations vs Si substitution.

NMR studies of Cu_2Se show an initial appearance of ionic hopping in a narrow temperature range above 100 K, coinciding with the recently observed low-temperature phase transition. At room temperature and above, this goes over to rapid Cu-ion hopping and a single motionally narrowed line both above and below the α-β structural transition. Furthermore, the NMR results on Cu_2Te and $Cu_{1.98}Ag_{0.2}Te$ demonstrate unusually large neg-

ative chemical shifts, as well as large Cu and Te s-state contributions in the valence band. The large diamagnetic chemical shifts coincide with behavior previously identified for materials with topologically nontrivial band inversion, and in addition, the large metallic shifts point to analogous features in the valence band density of states, suggesting that Cu_2Te may have similar inverted features.

DEDICATION

To my mother and father.

ACKNOWLEDGMENTS

I would like to thank my advisor Prof. Joseph H. Ross, Jr. for his support and patience throughout my graduate study. I would like to thank all the members of our group for providing a productive environment: Dr. Jing-Han Chen, Dr. Xiang Zheng, Laziz Saribaev. Many thanks to Dr. Daya Rathnayaka, Tyler Morrison, and Dr. Lucia Steinke for helping me in transport and heat capacity measurements of this study. I would like to thank the committee members: Donald Naugle, Artem Abanov, and Raymundo Arroyave for their time and suggestions.

Many thanks to Prof. Ctirad Uher, Dr. Sedat Ballikaya, Prof. Silke Paschen, Prof. Zhifeng Ren, and Dr. Xinlin Yan, for providing samples for NMR measurements.

This work was supported by the Robert A. Welch Foundation, Grant No. A-1526.

TABLE OF CONTENTS

Page

LIST OF FIGURES

FIGURE Page

LIST OF TABLES

1. INTRODUCTION AND LITERATURE REVIEW*

1.1 Background and Review of Recent Studies

1.1.1 Thermoelectric Materials

T. J. Seebeck, in the 1820s [1, 2], discovered the basis of the thermocouple which is that an electromotive force is generated when the junction between two dissimilar metals heat up. A few years later, Peltier [3] identified that the electrical current, depending on the current direction, can heat up or cool down the junction. Despite the knowledge of these effects for a long time, the practical usage of thermoelectric materials started in 1950s [4]. Recently, due to the importance of heat recovery and limited source of the fossil fuels, many new studies have been done to increase the efficiency of these effects, particularly since 1990.

Figure 1.1(a) shows that a voltage (V) will appear around a conductor A in the presence of a temperature gradient (ΔT) between two different junctions. The voltage is related to

*Part of this section is reprinted with permission from "Pseudogap and anharmonic phonon behavior in $Ba_8Ga_{16}Ge_{30}$: An NMR study," A. A. Sirusi and J. H. Ross, Jr., *J. Chem. Phys.*, vol. 145, p. 054702, 2016. Right managed by AIP publishing LLC.

*Part of this section is reprinted with permission from "NMR study of $Ba_8Cu_5Si_xGe_{41-x}$ clathrate semiconductors," A. A. Sirusi *et al.*, *Phys. Chem. Chem. Phys.*, vol. 17, p. 16991, 2015. Reproduced by permission of the PCCP Owner Societies.

*Part of this section is reprinted with permission from "Synthesis, transport and magnetic properties of Ba-Co-Ge clathrates," A. A. Sirusi and J. H. Ross, Jr., *J. Electron. Mater.*, vol. 45, p. 1094, 2016. Copyright (2015), The Minerals, Metals & Materials Society.

*Part of this section is reprinted with permission from "Low-temperature structure and dynamics in Cu_2Se," A. A. Sirusi *et al.*, *J. Phys. Chem. C*, vol. 119, p. 20293, 2015. Copyright (2015) American Chemical Society.

*Part of this section is reprinted with permission from "Band ordering and dynamics of $Cu_{2-x}Te$ and $Cu_{1.98}Ag_{0.2}Te$," A. A. Sirusi *et al.*, *J. Phys. Chem. C*, vol. 120, p. 14549, 2016. Copyright (2016) American Chemical Society.

the difference between two Seebeck coefficients of two conductors ($S_{\mathrm{AB}} = S_{\mathrm{A}} - S_{\mathrm{B}}$) [5]:

$$S_{\mathrm{AB}} = -\frac{V}{\Delta T}. \tag{1.1}$$

In general, the Seebeck coefficient is negative (positive) in materials with electron (hole) carriers. For example, in an *n*-type semiconductor the Seebeck coefficient is negative since electrons are the main carriers.

Typically only the single Seebeck coefficients ($S = S_{\mathrm{A}}$) of materials are given even though measured in pairs. Furthermore, to compare the efficiencies of thermoelectric materials, the figure of merit, zT, can be used. It is defined as

$$zT = \frac{\sigma S^2 T}{\kappa}, \tag{1.2}$$

where σ is the electrical conductivity, and κ the thermal conductivity. The thermal conductivity is $\kappa = \kappa_{ph} + \kappa_{el}$, where κ_{ph} and κ_{el} are the phonon and electron contributions, respectively. In application, thermoelectric materials can be used as thermoelectric generators and refrigerators. They require both *n*- and *p*-type semiconductors. Figure 1.1(b) shows schematics of both a thermoelectric generator and refrigerator. Also, it has been shown [5] that the figure of merit reflecting the total performance of the system is close to the average of zT_n and zT_p, where zT_n and zT_p are the figure of merits of the n and p legs (Figure 1.1(b)). Besides these schemes, it is possible to have cryogenic Peltier cooling with only one thermoelectric compound if the compound has an anisotropic Seebeck coefficient ($S_{xy} \neq 0$) [6]. For materials to be considered as promising thermoelectrics, $zT \geq 1$ is required. Therefore, it is found beneficial to have materials with high power factors (σS^2) and then reduce their thermal conductivities. Many ideas for reducing the thermal conductivity have been implemented. Nano-inclusion and nanostructuring can yield zT of 1.5 $-$

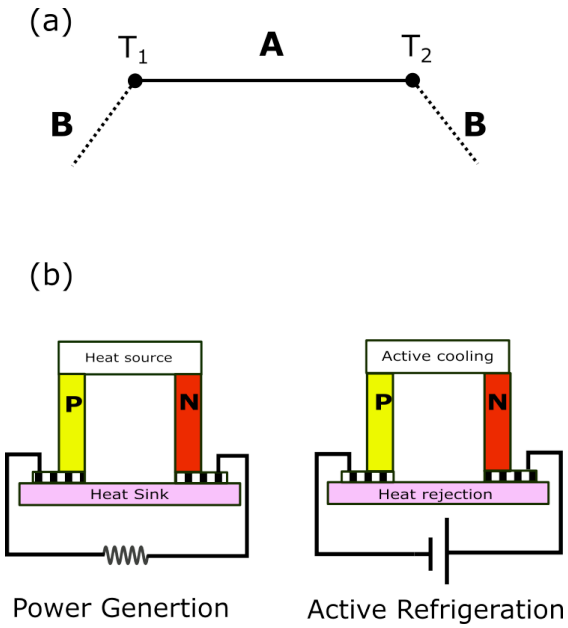

Figure 1.1: (a) A voltage (V) can be detected in the presence of temperature gradient across metal **A** ($T_1 \neq T_2$) (b) Schematics of both thermoelectric generator and refrigerator are shown.

1.8 at 750− 900 K in several materials [7, 8, 9, 10, 11, 12, 13] and, by adding mesoscale grain boundaries, $zT = 2.2$ K at 915 K had been achieved [14] in PbTe. Charge density waves [15] can also reduce the thermal conductivity along with the enhancement of the Seebeck coefficient through strong electron-phonon coupling. It is noteworthy to mention that some bulk materials have intrinsically low thermal conductivities due to their strong anharmonicities. Moreover, the lone-pair idea can reduce the thermal conductivity [16] through electrostatic repulsion with neighboring ions. The electron lone-pair concept is realized in the natural mineral tetrahedrites ($Cu_{12}Sb_4S_{13}$) [17]. Furthermore, the anharmonicities in SnSe and PbTe [18, 19] have proven to have substantial roles in their low thermal conductivities and thereby their high zT.

One can also reduce the thermal conductivity using complex structures [20]. Clathrate and filled skutterudite compounds have complex structures with guest atoms enclosed in

their framework cages. Both of these structures obey the phonon-glass electron-crystal (PGEC) concept where the compounds behave like a glass for phonons and like a crystal for electrons. An extension of PGEC is the phonon-liquid electron-crystal (PLEC) [21] in which the sublattice of the crystal is melted and behaves like a liquid. PLEC is a new way to have a reduced thermal conductivity. Copper-based chalcogenides seem to comply with the PLEC concept, in which the Cu atoms can move freely (like a liquid) in a crystal at high temperatures.

1.1.2 Transport of Carriers

The electrical conductivity, the Seebeck coefficient, and the thermal conductivity of materials (in this case for electrons) can be derived by using the Boltzmann transport equations [5]. In the calculations below, the relaxation time τ_e is presumed to follow the behavior $\tau_0 E^r$, where E is the energy. It is noted that r and τ_0 are determined by the scattering process; if $r = -1/2$, the lattice vibrations are a predominant source of scattering and if $r = 3/2$, the ionized impurities are the main scattering process. Therefore, using the Boltzmann transport equations along with the electric current and the heat flux density one can obtain [5]

$$\sigma = \frac{e^2}{T} K_1, \tag{1.3a}$$

$$\kappa_{el} = \frac{1}{T^2}\left(K_2 - \frac{K_1^2}{K_0}\right), \tag{1.3b}$$

$$S = \pm\frac{1}{eT}\left(E_F - \frac{K_1}{K_0}\right), \tag{1.3c}$$

where E_F is the Fermi energy (relative to the conduction band edge) and K_s for $s = 0$ to 2 is given by,

$$
\begin{aligned}
K_s &= \frac{-2T}{3m^*}\int_0^\infty g(E)\tau_e E^{s+1}\frac{df_0(E)}{dE}dE \\
&= \frac{8\pi}{3}\left(\frac{2}{h^2}\right)^{3/2}(m^*)^{1/2}T\tau_0\left(s+r+3/2\right)(k_BT)^{s+r+3/2}F_{s+r+1/2},
\end{aligned}
\tag{1.4}
$$

where $F_n(\xi) = \int_0^\infty \xi^n f_0(\xi)d\xi$ is the Fermi-Dirac integral, f_0 the Fermi-Dirac distribution function, m^* the effective mass, and $\xi = E/k_BT$.

For degenerate semiconductors ($E_F \gg k_BT$) to first order, in which case Eqns. 1.3 result in

$$
S = \pm\frac{\pi^2}{3}\frac{k_B}{e}\frac{r+3/2}{\eta}, \tag{1.5a}
$$

$$
L = \frac{\kappa_{el}}{\sigma T} = \frac{\pi^3}{2}\left(\frac{k_B}{e}\right)^2, \tag{1.5b}
$$

where $\eta = E_F/k_BT$ (the reduced Fermi energy). L is denoted the Lorenz number, and Eqn. 1.5b is called the Wiedemann-Franz law. In a metallic system, a large η gives a low Seebeck coefficient. Therefore, metallic materials cannot be suitable for thermoelectric applications.

For the non-degenerate semiconductors with fewer impurities and $\eta < -2$, the Seebeck coefficient can be written as

$$
S = \pm\frac{k_B}{e}(\eta - (r+5/2)). \tag{1.6}
$$

It can be seen that by increasing η, the Seebeck coefficient increases. In general, extrinsic semiconductors can possess high Seebeck coefficients on the order of several hundreds of μV/K.

It should be mentioned that one effect that makes the Seebeck coefficient low is the

bipolar effect when both electrons and holes participate in the transport effects. In this case, Eqns. 1.3 result in

$$\sigma = \sigma_n + \sigma_p, \tag{1.7a}$$

$$\kappa_{el} = \kappa_n + \kappa_p + \frac{\sigma_n \sigma_p}{\sigma_n + \sigma_p}(S_n - S_p)^2 T, \tag{1.7b}$$

$$S = \frac{S_n \sigma_n + S_p \sigma_p}{\sigma_n + \sigma_p}. \tag{1.7c}$$

While the bipolar effect give rises to a large electrical conductivity, it reduces the Seebeck coefficient because of opposite signs of S and increases the thermal conductivity.

Moreover, a high value of $\mu(m^*)^{3/2}$ [22] is required for a large zT, where μ is the mobility and m^* the density-of-states effective mass. For the case of scattering by phonons $\mu(m^*)^{3/2} \propto N_\nu/m_I$ where N_ν is the number of valleys in the first Brillouin zone, and $m_I = 3/(1/m_1 + 1/m_2 + 1/m_3)$ is the carrier inertial mass, where $m_1, m_2, \text{ and } m_3$ are the effective masses along the axes of symmetry. Thus, to enhance zT, one needs to have a large number of valleys and low inertial mass (m_I) as well. Note that the high zT materials tend to have small band gaps, which results in low Seebeck coefficients ($E_g \simeq S_{max} 2eT$), however, they have high $\mu(m^*)^{3/2}$ [22].

The total thermal conductivity is a sum of both carrier and lattice parts. The lattice thermal conductivity is expressed as [23]

$$\kappa_{ph} = \frac{1}{3} C_v \nu l, \tag{1.8}$$

where C_v is the heat capacity, l the phonon mean free path, and ν the speed of sound.

Besides the effort to decrease the lattice thermal conductivity, it is possible to improve the power factor as well. The improvement can be realized through several ways such as enhancing the density of states, utilizing impurity bands, and band convergence [24, 25].

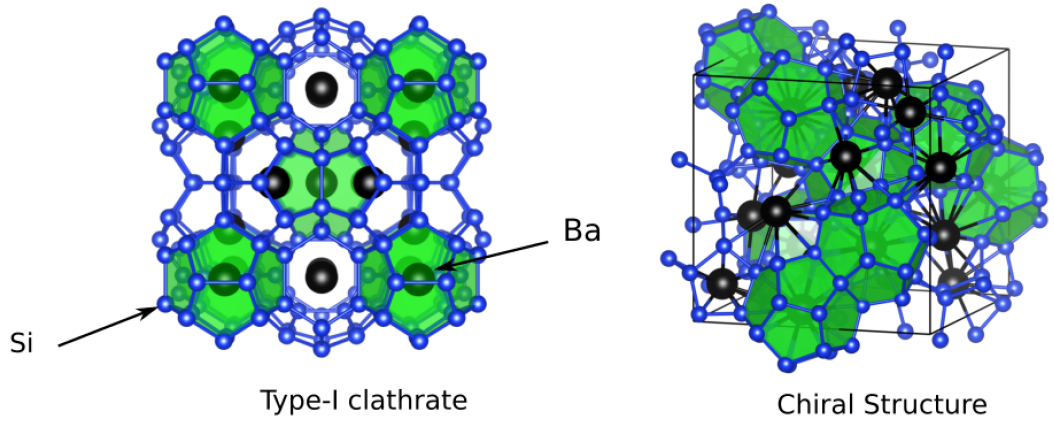

Figure 1.2: Type-I clathrate structure of Ba_8Si_{46} and chiral structure of $Ba_{24}Ge_{100}$.

1.1.3 Intermetallic Clathrate

Intermetallic clathrates, due to their unique structures, can fulfill the PGEC concept and show interesting physical properties, especially the low thermal conductivity [20, 26, 27, 28, 29]. Type-I clathrates have gained attention because of their higher zT and stable structure [30, 31, 32, 29, 33] at high temperatures. The general formula for type-I is M_8X_{46} (structure shown in Figure 1.2), where M is the guest or "rattler"atom, such as Ba, Sr, Eu encapsulated in the framework constructed of X atoms (X = Ge, Si, or Sn). The framework atoms have three Wyckoff crystallographic sites: 6*c*, 16*i*, and 24*k*. Due to the low thermoelectric efficiency of binary clathrates, it is customary to substitute framework atoms by the transition metals to expand the cages and optimize the electron density. Several groups used quaternary compounds [34, 35, 36] as well. Another type of clathrates, including a set of materials whose transport and magnetic properties are reported in this thesis, is the chiral structure (shown in Figure 1.2). The general formula for the chiral structure is $M_{24}X_{100}$.

Type-I has 54 atoms in its unit cell. The unit cell contains two small cages (dodecahe-

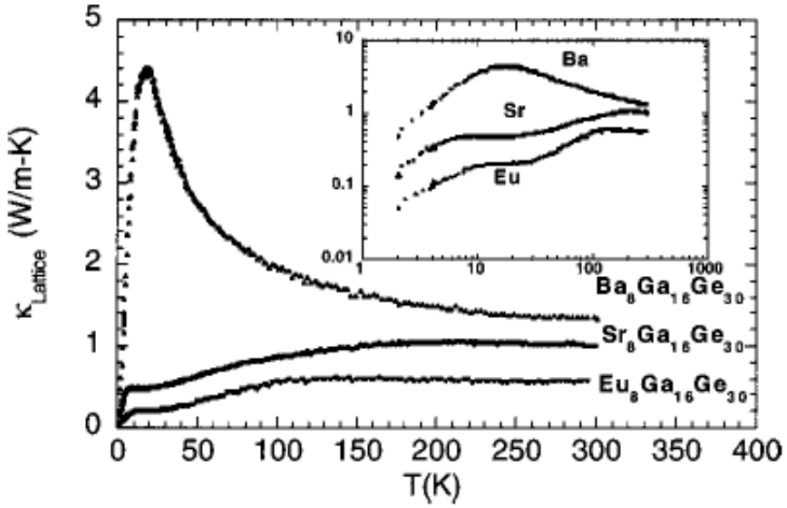

Figure 1.3: The on-center *n*-type $Ba_8Ga_{16}Ge_{30}$ illustrates a crystal-like behavior, while the off-center $Sr_8Ga_{16}Ge_{30}$ and $Eu_8Ga_{16}Ge_{30}$ show glass-like behaviors. Reprinted with permission from [37]. Copyright (2001) American Physical Society.

dron) and six large ones (tetrakaidecahedron) [29]. The guest atoms inside the dodecahedron (2*a* site) and tetrakaidecahedron (6*d* site) are designated in this thesis as (1) and (2). Neutron scattering of $\mathcal{R}_8Ga_{16}Ge_{30}$ ($\mathcal{R}$ = Ba, Sr, Eu) samples showed that Sr(2) and Eu(2) have a large atomic displacement in the cage center but Ba(2) does not [38, 37]. However, Christensen *et al.* [39], via x-ray and neutron diffractions, showed that Ba(2) atoms indeed have a small off-center position.

Based on such behavior, it is possible to classify type-I clathrates in two ways: on-center and off-center classes. The thermal conductivities of on-center and off-center type-I clathrates are quite different. The on-center (or small off-center) type-I clathrates (such as n-type $Ba_8Ga_{16}Ge_{30}$) exhibit crystal-like thermal conductivities [37, 40, 41] (Figure 1.3). In contrast, the off-center type-I clathrates (such as $Sr_8Ga_{16}Ge_{30}$ and $Eu_8Ga_{16}Ge_{30}$) exhibit glass-like features (Figure 1.3) due to rattling and tunneling states. Although off-center guest atom positions can provide a good explanation for glass-like features, they cannot

explain the glass-like behavior of the p-type $Ba_8Ga_{16}Ge_{30}$, which has the same structure as the n-type $Ba_8Ga_{16}Ge_{30}$. Anders Bentien *et al.* [42] suggested that the phonon-charge carrier interaction would be the source of the glass-like property. Moreover, the off-center guest atoms can exhibit dipole moments at the center of cages based on which the dipole-dipole interactions can give rise to glass-like behavior [29]. In this dipole-dipole interactions picture, the small off-center displacement in p-type $Ba_8Ga_{16}Ge_{30}$ can make small dipole moments which cannot be shielded by electrons. This is in contrast to n-type $Ba_8Ga_{16}Ge_{30}$ in which extra electrons can shield the dipole moments. Therefore, the results of antishelding (having a long-range order) would be the reason for the presence of the glass-like thermal conductivity features.

Despite significant developments in understanding, the underlying physics of low thermal conductivity in the clathrates and the roles of guest atoms are still controversial. In one picture, the guest atom rattling can resonantly scatter phonons and make the thermal conductivity low [43]. In another scenario, it is the hybridization of the guest atom modes with the framework acoustic modes, which results in an avoided crossing [44], causing flat bands that can reduce the phonon velocity. In addition, Pailhès *et al.* [45], by using inelastic x-ray diffraction and DFT calculations, showed that the localization phonon modes in a single crystal of Ba_8Si_{46} are the source of the low thermal conductivity, not the phonon scattering by guest atoms. Moreover, recent studies using *ab-initio* calculations [46] have connected the low thermal conductivity of $Ba_8Ga_{16}Ge_{30}$ to nonresonant phonon scattering and a significant reduction of phonon relaxation times compared to the unfilled clathrates.

Our group has done plenty of NMR measurements on the intermetallic clathrates, such as $Ba_8Ga_{16}Sn_{30}$ and $Sr_8Ga_{16}Ge_{30}$ [47, 48]. The NMR results of the type-I $Ba_8Ga_{16}Sn_{30}$ clearly revealed a rattling peak in T^{-1} at low temperatures as a result of anharmonic motion of guest atoms [47].

1.1.4 Copper-Based Chalcogenide Compounds

Copper-based chalcogenides $Cu_{2-x}X$ (X = S, Se, Te) have been well-known as superionic conductors for a long time [49, 50]. These compounds are potentially useful for solar [51], thermoelectric [52, 53, 21, 54], and battery [55] applications. Study also shows that the structures of these materials indicate 2D features, which can give rise to new physics [56]. Thus, there has been a great deal of recent work on these materials. However, in many cases, these materials, in spite of their simple formula units, have very complicated and controversial structures [57, 58, 59, 60, 61, 62, 63].

As a semiconductor, $Cu_{2-x}Se$ is a *p*-type self-doped material dominated by native Cu vacancies, which are associated with the observed Cu-deficient stoichiometry. The Se ions form a relatively immobile lattice, while Cu ions have a very high mobility, resulting in its well-known superionic behavior [49]. The ionic mobility increases rapidly with temperature, and then near 390 K, the Se ions exhibit a crystallographic transformation to give a high temperature antifluorite structure (β-phase), in which Se atoms are on the FCC sites and the Cu atoms are randomly distributed among the interstitial sites (tetrahedral 8*c*, trigonal 32*f*, and a small fraction on octahedral 4*b* sites [64, 65]) as shown in Figure 1.4(c). The transformation has been shown to have a large positive effect on the thermoelectric figure of merit [66]. The room-temperature α-phase is structurally complex and there are other changes apparent at low temperatures, with recent results indicating a transformation to an additional phase (α' phase) near 100 K [52, 67, 56]. Many different structures have been proposed for the α phase, tetragonal [68], pseudo-orthorhombic [69], monoclinic [62, 70, 71], and superlattice [57]. Gulay *et al.* [62] gave a monoclinic structure with space group $C2/c$ with the unit cell of 144 atoms (Figure 1.4(a)). In addition, the newest structure (space group $P2_1/c$) at low temperatures introduced Cu_2Se as a layered structure [56, 63] as shown in Figure 1.4(b). It also has been shown through

transmission electron microscopy (TEM) [72] that Cu_2Se is a combination of there structures at room temperature, consist of two triclinic and monoclinic structures. There have also been several related reports of metastability and vacancy-ordering transitions in the low temperature phase. Another interesting feature of $Cu_{2-x}Se$ is that the phase transition temperature reduces to lower temperatures when x increases until $x = 1.8$, above which the phase transition does not exist [73, 74]. More importantly the transition temperature can be controlled by doping with silver and iodine [52, 75, 53].

The origin of the high Seebeck coefficient around a phase transition is not clear. Mahan [76] ascribed the enhanced Seebeck coefficient to the width broadening of the conduction band and Liu *et al.* [53] explained the results as due to the critical scattering around the phase transition. In a different scenario, Brown *et al.* [50] explained this enhancement through additional "structural entropy" coupling with the charge carriers. A similar idea of entropy coupling which can enhance the Seebeck coefficient can be seen in Na_xCoO_2 [77] in which the spin entropy couples to the charge carriers. Furthermore, Kang *et al.* [78] provided different explanations for the Seebeck enhancement based on a first order phase transition, coexistence of α and β phases, and reduction of the holes which make Cu_2Se to be at an optimum condition to have a large Seebeck coefficient.

Interestingly, above the phase transition, the heat capacity (C_V) of Cu_2Se also approaches to a value $2R$ [21], where R is the gas constant. The $2R$ value corresponds to a liquid feature in which the phonons transverse modes cannot propagate. Therefore, it leads to lower thermal conductivity at high-T and thus higher zT. On the other hand, despite the measured large zT, Cu_2Se suffers from several practical issues, such as Se loss, degradation, and chemical processes [79].

The closely related material, $Cu_{2-x}Te$ shows metallic features [80, 81, 82] but with an apparent optical band gap of order 1 eV [83]. These results correspond to its heavily-doped semiconducting behavior, with the transport dominated by holes due to native Cu vacan-

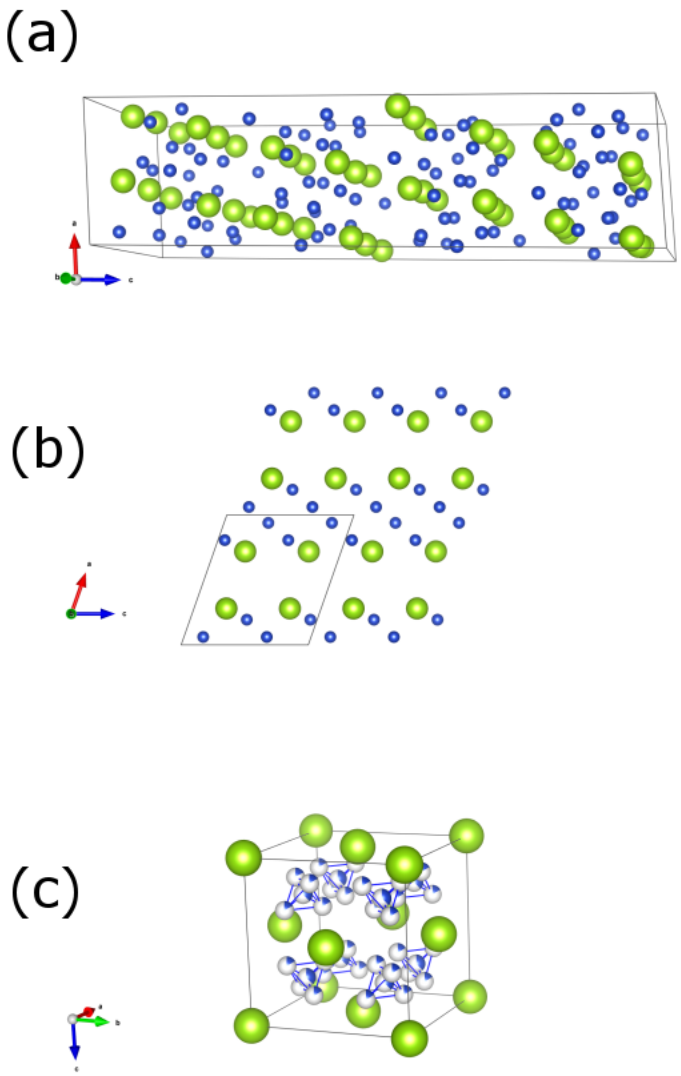

Figure 1.4: Cu_2Se structures (Se: large spheres, Cu: small spheres); (a) a monoclinic (space group $C2/c$) at room temperature [62], (b) a monoclinic structure (space group $P2_1/c$) as a layered structure [56, 63], and (c) a cubic structure above phase transition.

cies. It should be noted that an intrinsic insulating behavior is expected for the ideal Cu_2Te stoichiometry. These are the same general features as found in Cu_2Se. Cu_2Te. also has a complicated crystal structure at room temperature, including reported hexagonal [84] and orthorhombic [85, 86] structures and a mixture of both hexagonal and orthorhombic structures [87], and more recently Nguyen *et al.* [63] with an adaptive genetic algorithm in combination with first-principles density functional theory proposed a monoclinic (space group $C2/m$) structure including 4 Cu_2Te formula unit per unit cell. Furthermore, $Cu_{2-x}Te$ goes through additional phase transitions at high temperatures. For example, it is reported that Cu_2Te has five successive phase transitions at 453 K, 540 K, 573 K, 635 K, and 821 K [85], although the structures can also change with vacancy density. At the highest transition it changes to a FCC structure. In addition, it has been shown [88] that the zinc-doped Cu_2Te ($Cu_{1.5}Zn_{0.5}Te$) has most of the phase transitions suppressed except the highest one which occurs at 811 K.

These compounds have a decreased thermal conductivity attributed to the phonon-liquid electron-crystal (PLEC) mechanism, which as described above is the extension of PGEC, decreasing the thermal conductivity. Thereby, Cu_2Te along with other copper-based chalcogenides are considered as prospective thermoelectric materials [21, 52, 89, 66, 54].

2. INTRODUCTION TO SOLID STATE NMR AND EXPERIMENTAL TECHNIQUES

2.1 Nuclear Magnetic Resonance

Nuclear Magnetic Resonance (NMR) is a powerful local spectroscopy. It can measure the spectrum of the polycrystallines, single crystals, and powder samples. It also can be implemented on metallic, semiconductor and insulating materials. We can obtain a great deal of information from NMR: determination of complex materials structures, hyperfine couplings (internal magnetic fields seen by the particular spin, giving chemical shifts and Knight shifts), motional narrowing due to motion of the spin or its surroundings, excitation of collective spin, etc. Most of the studies reported in this thesis used these techniques.

Most nuclei have a spin $\vec{I}$ and a magnetic moment $\vec{\mu} = \gamma_n \hbar \vec{I}$, where γ_n is the nuclear gyromagnetic ratio. The Hamiltonian of a nucleus in an external magnetic field $\vec{H}$ is

$$\mathcal{H} = -\vec{\mu} \cdot \vec{H}. \tag{2.1}$$

If the magnetic field $\vec{H} = H_0 \hat{z}$, then the eigenvalues (or the Zeeman energy levels) are

$$E = -m\gamma_n \hbar H_0, \qquad m = I, ..., -I. \tag{2.2}$$

By applying radio frequency (rf) pulses, one can make transitions between the Zeeman energy levels or couple different energy levels and withdraw much information about the materials.

2.2 Equations of Motion

Although the nature of NMR spectroscopy is governed by quantum mechanics, the classical descriptions can provide a suitable understanding of many NMR phenomena. The corresponding equations, which can nicely describe the dynamics of the magnetization ($\vec{M}$) in the presence of the applied field ($\vec{H}$), are the Bloch equations:

$$\frac{dM_z}{dt} = \gamma_n \left(\vec{M} \times \vec{H}\right)_z - \frac{M_z - M_0}{T_1}, \tag{2.3a}$$

$$\frac{dM_{x,y}}{dt} = \gamma_n \left(\vec{M} \times \vec{H}\right)_{x,y} - \frac{M_{x,y}}{T_2}, \tag{2.3b}$$

where T_1 is the spin-lattice relaxation time (or longitudinal relaxation time), and T_2 is the spin-spin relaxation time (or transverse relaxation time) relating to the component of $\vec{M}$ in the x-y plane. T_1 relaxation is caused by transferring spin energy to the phonons or conduction electrons (the lattice). In contrast, T_2 processes in a static magnetic field conserve the energy. In addition, as defined here, T_2 corresponds to the dephasing of the spin by one radian (although later will be discussed other processes involving a Gaussian decay).

One can describe the NMR experiments in a much simpler way in a rotating frame (axes denoted x', y', z'). In the rotating frame, the effect of the static magnetic field is eliminated. Assuming the magnetization is fixed relative to the magnetic field ($\vec{H_0}$), $\vec{M}$ will precess about the field direction following the equation $d\vec{M}/dt = \vec{M} \times \gamma\vec{H_0}$. If we move to the rotating frame with an arbitrary angular frequency $\vec{\Omega}$, then the rate of change of the magnetization in the rotating frame will be $\delta\vec{M}/\delta t = d\vec{M}/dt - \vec{\Omega} \times \vec{M} = \gamma\vec{M} \times (\vec{H_0} + \vec{\Omega}/\gamma) = \gamma\vec{M} \times \vec{H_{eff}}$. It can be seen that at resonance ($\Omega = -\gamma H_0$), the magnetization is constant. In NMR, when applying an rf pulse (H_1) in the x' direction, the magnetization will precess about the x' axis. In other words, the magnetization can be

placed on the y' axis by a 90° pulse ($\pi/2 = \gamma H_1 t$) about the x' axis.

After turning off the 90° rf pulse, the magnetization will rotate in the x-y plane in the lab frame and induce a voltage in the pick-up coil. The voltage signal will decay exponentially as e^{-t/T_2^*}, where $1/T_2^* = 1/T_2 + \gamma \Delta H_0$, where ΔH_0 is the magnetic field inhomogeneity and T_2 is the spin-spin relaxation time. This process is called the free induction decay (FID), as shown in Figure 2.1. In our experiments, we usually used the spin-echo technique (explained later) to remove ΔH_0.

2.3 Knight Shift

In metallic samples, the conduction electrons interact with nuclei through hyperfine interactions. The Hamiltonian coupling a single electron and the nucleus is [90]

$$\mathcal{H} = -2\mu_B \gamma_n \hbar \vec{I} \cdot [\frac{8\pi}{3} \vec{s} \delta(\vec{r}) + [\frac{3\vec{r}(\vec{r} \cdot \vec{s})}{r^5} - \frac{\vec{s}}{r^3}] - \frac{\vec{l}}{r^3}], \tag{2.4}$$

where μ_B is the Bohr magneton, $\vec{s}$ is the electron spin, and $\vec{l}$ is the orbital angular momentum of the electrons. The first term is the Fermi contact. For the s-state electrons, only the Fermi contact term will remain after averaging. In the presence of a magnetic field, the effective contact term can be written [90] as

$$\mathcal{H} = -\gamma_n \hbar I_z \big[\frac{8\pi}{3} \left\langle |\Psi_s(0)|^2 \right\rangle_{E_F} \chi_p H_0\big], \tag{2.5}$$

where χ_p is the Pauli paramagnetic spin susceptibility and $\Psi_s(0)$ is the electron wave function at the nucleus. From Eqn. 2.5 the Knight shift (K) can be derived:

$$K = \frac{\Delta H}{H_0} = \frac{8\pi}{3} \left\langle |\Psi_s(0)|^2 \right\rangle_{E_F} \chi_p, \tag{2.6}$$

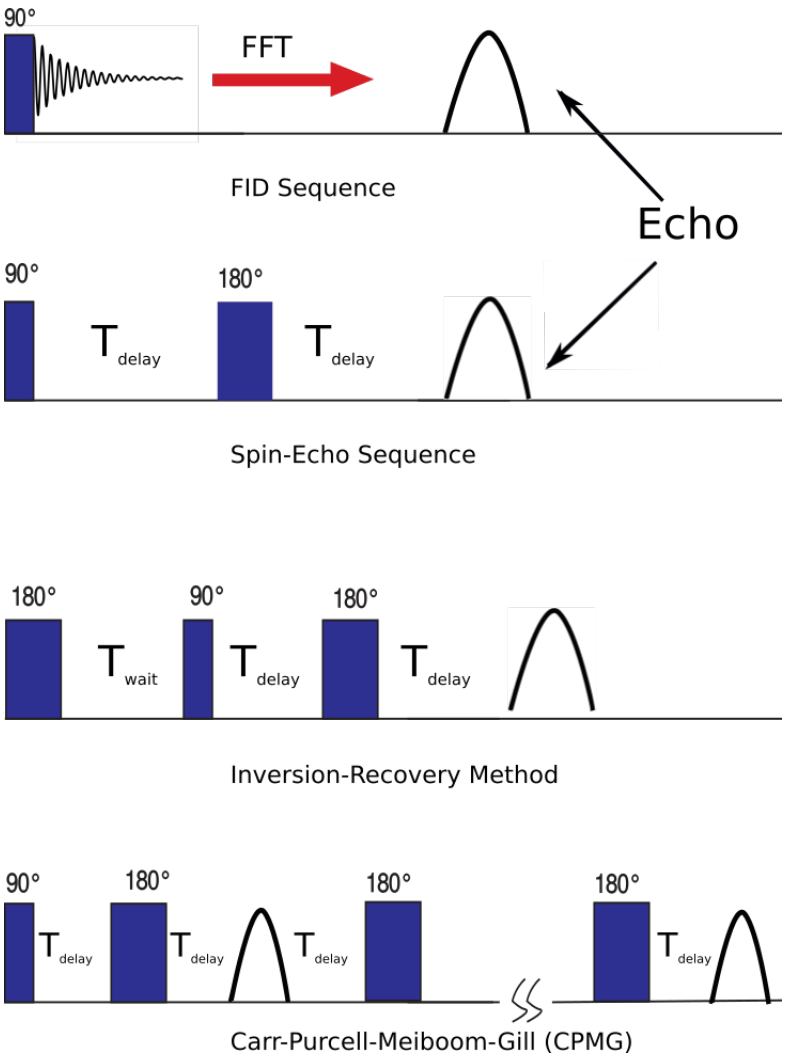

Figure 2.1: Free induction decay (FID), spin echo, inversion-recovery, and CPMG sequences.

or

$$K = \frac{\Delta H}{H_0} = H^{HF}\chi_{\rm p}/\mu_B, \tag{2.7}$$

where H^{HF} is the hyperfine coupling. Elsewhere in the thesis we have used standard values of H^{HF} to estimate Knight shifts; this rests upon the observed results that the features of the atom-based wave functions near the core change relatively little among different solids, at least for simple metallic systems. In paramagnetic metals, the relaxation time (T_1) can be related to the Knight shift through the Korringa relation [90]:

$$K^2 T_1 T = \frac{\hbar}{4\pi k_B}\frac{\gamma_e^2}{\gamma_n^2}, \tag{2.8}$$

where γ_e is the electron gyromagnetic ratio and k_B is the Boltzmann constant, although the electron-electron interactions will modify the Korringa relation. In addition, core polarization (K_{core}), orbital contributions of conduction electrons (K_{orb}), and the presence of rare earth atoms in the samples (K_{loc}) can have contributions to the total Knight shift. Therefore, by analyzing these various effects the Knight shift can provide information about hyperfine interactions.

2.4 Chemical Shift

The chemical shift (δ) is due to an induced magnetic field that a particular spin sees when the sample is put in the applied magnetic field [91], generally distinguished from K by being due to filled shells and orbital-dominated. The mechanism of the chemical shift is shown in Figure 2.2. The chemical shift Hamiltonian is defined as

$$\mathcal{H}_{cs} = \gamma \vec{I} \cdot \sigma \cdot \vec{H}, \tag{2.9}$$

where the σ is a second-rank tensor and called the chemical shielding (and $\delta = -\sigma$). In the principal axes system, the chemical shift has a diagonal form with three compo-

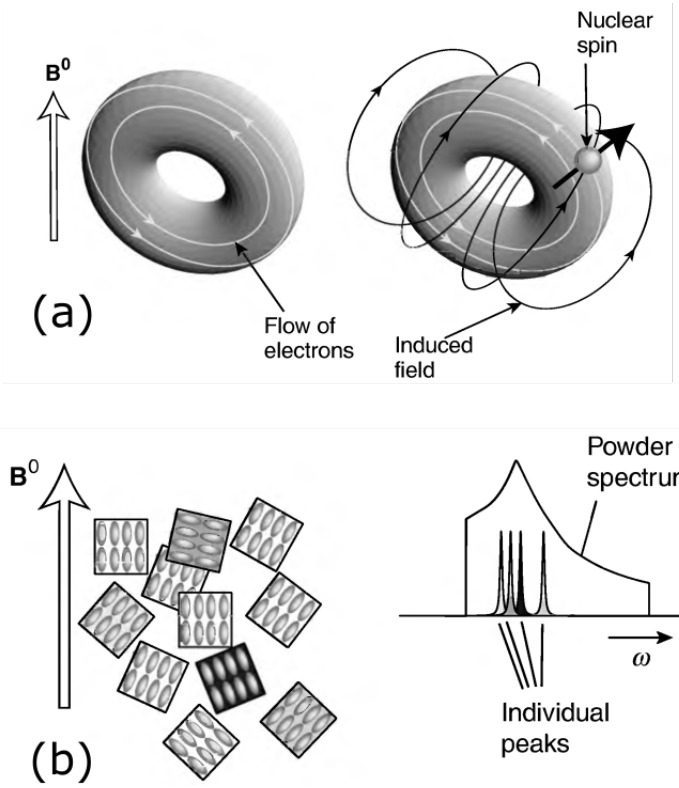

Figure 2.2: (a) Chemical shift mechanism: currents can be induced by an applied magnetic field and the induced currents will affect the nucleus. (b) Chemical shift powder pattern which stems from the superposition of many individual peaks at different frequencies due to different crystal orientation, shown schematically at left. Reprinted with permission from [91]. Copyright (2008) John Wiley and Sons.

nents ($\delta_{XX}, \delta_{YY}, \delta_{ZZ}$). The powder pattern line shapes (see Figure 2.2(b)) dominated by the chemical shift interaction are usually described by the isotropic chemical shift $\delta_{iso} = (\delta_{XX} + \delta_{YY} + \delta_{ZZ})/3$, the chemical shift anisotropy $\delta_{aniso} = \delta_{ZZ} - \delta_{iso}$ with δ_{ZZ} the largest term, and the asymmetry $\eta = (\delta_{YY} - \delta_{XX})/\delta_{aniso}$. The anisotropic chemical shift Hamiltonian has an angular momentum $l = 2$, and it is proportional to the $3\cos^2\theta - 1$ term. Moreover, the anisotropic chemical shift can be eliminated partially by the using spin-echo sequence (a technique which will be described later).

2.5 Quadrupole Interaction

Nuclei with $I \geq 1$ have non-zero quadrupole moments (Q). The sign of Q depends on the nuclear shape. Therefore, the spin ($I \geq 1$) in an environment with a symmetry lower than the cubic symmetry will experience an electrostatic field and will have energy level splittings.

The energy of the charge distribution ($\rho(r)$) in the presence of an electrostatic potential $V(r)$ is

$$E = \int \rho(r)V(r)d\tau. \tag{2.10}$$

We can expand $V(r)$ around the origin:

$$V(r) = V(0) + \sum_{\alpha} x_\alpha V_\alpha|_{r=0} + \frac{1}{2!}\sum_{\alpha,\beta} x_\alpha x_\beta V_{\alpha\beta}|_{r=0} + ..., \tag{2.11}$$

where

$$V_\alpha \equiv \left.\frac{\partial V}{\partial x_\alpha}\right|_{r=0},\ V_{\alpha\beta} \equiv \left.\frac{\partial^2 V}{\partial x_\alpha \partial x_\beta}\right|_{r=0}. \tag{2.12}$$

After some calculations and definitions and using the Wigner-Eckart theorem along with the Laplace equation ($\sum_{\alpha} V_{\alpha\alpha} = 0$) [90], the quadrupole Hamiltonian (due to the third terms in Eqn. 2.11) can be obtained:

$$\mathcal{H}_Q = \frac{eQ}{4I(2I-1)}[V_{zz}(3I_z^2 - I^2) + (V_{xx} - V_{yy})(I_x^2 - I_y^2)], \tag{2.13}$$

where Q is an electric quadrupole moment. By convention, the largest $V_{\alpha\alpha}$ component is defined as $eq = V_{zz}$, and the asymmetry parameter is written as

$$\eta = \frac{V_{xx} - V_{yy}}{V_{zz}}, \tag{2.14}$$

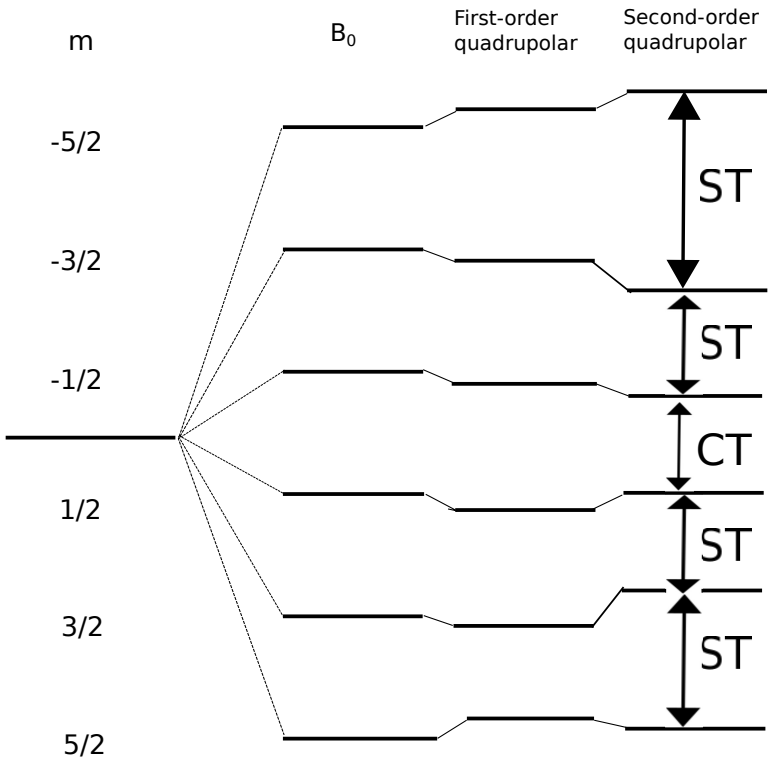

Figure 2.3: Zeeman levels due to magnetic-only interaction, and with the addition of first and second order quadrupole interaction. The central transition (CT) splitting does not change due to the first order quadrupole interaction in contrast to the satellite transitions (ST).

where $V_{\alpha\alpha}$ components are in the principal axis coordinate system. In the lab coordinates, when $H_Z \gg H_Q$, one can use perturbation theory. Figure 2.3 indicates schematically the Zeeman energy levels and effects of the first and second-order quadrupole interactions on them.

Assuming high symmetry systems (axial symmetry with $\eta = 0$) in the calculations, the combined first and second-order shifts can be written [92] as

$$\nu(m \leftrightarrow m-1) = \nu_0 + \frac{\nu_Q}{2}(3\mu^2 - 1)(m - 1/2) + \frac{\nu_Q^2}{32\nu_0}(1-\mu^2)\times$$
$$\{[102m(m-1) - 18I(I+1) + 39]\mu^2 - [6m(m-1) - 2I(I+1) + 3]\}. \tag{2.15}$$

where $\mu = \cos(\theta)$, where θ is the angle between the external field and the principal axis, and $\nu_Q = 3e^2qQ/(2I(2I-1)h)$. The first-order contribution vanishes for the central transition (1/2,−1/2), and only the second-order quadruple has an affect on the central transition. A more general relation can be expressed when $\eta \neq 0$, and as a result the two parameters ν_Q and η can be used to analyze a given spectrum.

2.6 Motional Narrowing

If the spin or its surroundings moves, then the NMR spectrum will be narrowed in the case of fast motion compared to the time scale of the inverse static linewidth. In this discussion I will follow the discussion from Kittel's book [93] which provides great insight. Assume an atom experiences a fluctuating field and the magnetic field goes from B_i to $-B_i$ in the average time τ. Therefore, the spin phase will vary by $\delta\phi = \pm\gamma B_i\tau$ in time τ ($\delta\phi \ll 1$). Using the random walk analogy, the mean square dephasing angle in a fixed field after n steps is $< \phi^2 >= n\gamma^2 B_i^2\tau^2$. The number of steps, n, to produce a 1 radian phase shift is $n = 1/(\gamma^2 B_i^2\tau^2)$. Therefore, the time in which this occurs for n steps is

$$T_2 = n\tau = \frac{1}{\gamma^2 B_i^2 \tau}. \tag{2.16}$$

In the rigid lattice, the linewidth is $\Delta\omega_0 = \gamma B_i$. Hence, since $\Delta\omega = 1/T_2$ then $\Delta\omega = \Delta\omega_0^2\tau$ (when $\tau \ll 1$). Note that the motional narrowing linewidth normally will actually not go to zero due to the inhomogeneity of the magnetic field. For typical activated

processes the rate of ion hopping, $1/\tau$, is related to the attempt frequency ($1/\tau_0$) and the activation energy (U) through an Arrhenius relation:

$$1/\tau = 1/\tau_0 e^{-U/kT}. \tag{2.17}$$

Usually the attempt frequency values are in the range of the optical phonon frequencies ($10^{12} - 10^{13}$ s^{-1}).

2.7 NMR Technique

When a sample is inserted in a magnetic field, according to the Boltzmann distribution the nuclei align themselves with the field direction. By applying a proper rf pulse, one can send the spins to the x'-y' plane (by a 90° pulse) or $-z'$ direction (by a 180° pulse). In our experiments the spectra and T_1 (spin-lattice relaxation time) were normally determined by the spin echo sequence and inversion-recovery methods, respectively (see Figure 2.1). It should be noted that since ^{137}Ba has a low gyromagnetic ratio and natural abundance (11%), we have also implemented the CPMG sequence (see Figure 2.1) and summed the echoes for enhanced signal.

Depending on the spin value ($I = 1/2, 3/2, 5/2, 7/2, 9/2$), different multi-exponential equations were used to fit the inversion-recovery data. The inversion-recovery sequence is shown in see Figure 2.1. For example, the equation for spin 3/2 in the case of multiple exponential recovery for excitation of the central transition, magnetic only [47] is

$$M(T_{wait}) = M(0)\left[1 - B\left(0.1e^{\frac{-T_{wait}}{T_1}} + 0.9e^{\frac{-6T_{wait}}{T_1}}\right)\right], \tag{2.18}$$

where $M(0)$ and B can be determined from the fit. To measure T_2, we used a spin-echo

sequence and fit the data to

$$M(2T_{delay}) = M(0)\left[\alpha e^{-\frac{2T_{delay}}{T_{2e}}} + (1-\alpha)e^{-\left(\frac{2T_{delay}}{T_{2g}}\right)^2}\right]. \tag{2.19}$$

Note that we also used a stretched-exponential recovery function $M(T_{wait})/M(0) = 1 - B(0.1e^{-(T_{wait}/T_1)^\beta} + 0.9e^{-(6T_{wait}/T_1)^\beta})$ for calculating T_1 of Ga NMR for the $Ba_8Ga_{16}Ge_{30}$ sample at the central transition, where the exponent β is presumed to be due to a distribution of local environments.

2.8 Magic Angle Spinning NMR

Magic angle spinning (MAS) is a technique to narrow the line. In this technique, the powder sample rotates at the 54.74° angle respect to the applied field. By this rotation, the Hamiltonian becomes time dependent, and those Hamiltonian terms which contain $3\cos^2\theta - 1$, average to zero if the rotation is fast enough. The dipole-dipole coupling, chemical shift, chemical shift anisotropy, first order quadruple interaction, and a part of the second-order quadrupole interaction contain the $3\cos^2\theta - 1$ term. For intermediate rotation speeds, the rotor rotation will cause the spectrum to have side bands with spacing equal to the rotation frequency, within a spectral range approximately equal to the static line shape. Therefore, to have the side bands out of the range of interest, one needs to rotate the rotor with a frequency larger than the static linewidth. Standard measurement probes are available for measurements now. I used the Chemistry Department's MAS NMR system to measure Cu MAS NMR in $Ba_8Cu_6Ge_{40}$ [94] and Si NMR in the $Ba_8Cu_5Si_{41}$ sample.

3. EXPERIMENTAL APPARATUS

3.1 NMR System

For almost all cases the NMR experiments were carried out using a custom-built pulse spectrometer made by Prof. Ross and previous students at a fixed field close to 9 T. Figure 3.1 shows a diagram of the NMR spectrometer. The NMR spectrometer consists of two main parts: a transmitter and a receiver. The transmitter guides the rf pulses to the pick-up coil. It includes a frequency synthesizer, a power amplifier, and a pulse sequence generator (PSG). The transmitter, through the pulse phase circuitry, can position the rf pulse (H_1) along the x', $-x'$, y', and $-y'$ directions in the rotating frame (quadrature phases). Note that the power required for NMR is in the range of 100 to 1000 watts.

The NMR receiver, first, amplifies the microvolt signals from the pick-up coil by a series of pre-amplifiers. The receiver, then, uses the quadrature detection to remove the rf carrier signals. In the quadrature detection scheme, the pick-up signal is split into two channels (X and Y). The Y channel changes the phase by 90°. Then, the signals in the X and Y channels are mixed with the reference frequency and passed through the low pass filters. To bring the signals to the desired level of a digitizer, more amplifiers are used as well.

The NMR spectrometer has also a cryostat chamber and is able to perform NMR from 4.2 K to 500 K using various probes. Liquid helium and nitrogen are used for temperatures below and above 77 K, respectively.

In this work, I have conducted NMR on the Cu, Ga, Te, Se, Ba, and Co nuclei. For each of the nuclei, I have made different LC circuits. In addition, magic angle spinning measurements on Cu clathrate sample [94] was carried out using a Bruker Avance 400 MHz instrument with a solid CuCl as a reference.

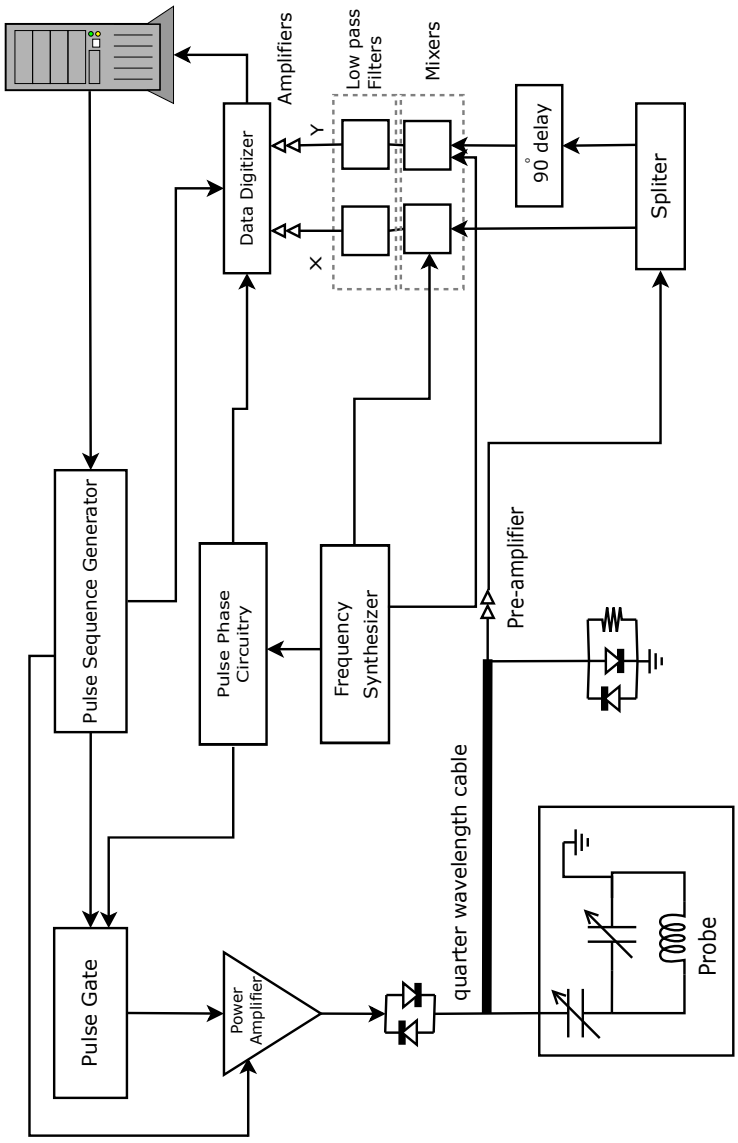

Figure 3.1: Block diagram of the NMR system.

3.2 PPMS, SQUID, XRD, and WDS

Powder x-ray diffraction (XRD) data were measured at room temperature using a Bruker D8 x-ray Powder Diffractometer in Department of Chemistry, and in some cases by our collaborators using separate instruments. When carried out locally, these measurements utilized facilities maintained by several researchers, However, Rietveld refinement was carried out using EXPGUI [95, 96] by myself. Wavelength dispersive spectroscopy (WDS) measurements were performed on at least four points on many of the samples in a Cameca SXFive Electron Microprobe. Resistivity, Hall coefficient, Seebeck coefficient, heat capacity, and thermal conductivity measurements were conducted in a Quantum Design Physical Property Measurement System and these data were also analyzed by myself. A Quantum Design SQUID magnetometer was used to measure magnetic properties. Moreover, I have built a separate Hall measurement setup as explained in the Appendix.

3.3 Computations

Ab-initio calculations were done using a WIEN2k package [97] by Dr. Jing-Han Chen, a former group member, and in some cases by myself. I have also fitted the NMR spectra with the Dmfit package [98] as well as the QuadFit package [99]. For displaying the crystal structures, we used the VESTA package [100]. I have done some follow up WIEN2k calculations to be published later, not described in this thesis.

3.4 Sample Preparation

In this work, most samples were synthesized by an arc melter or solid state reaction, and some followed by SPS. Copper-based chalcogenides were synthesized by Dr. Sedat Ballikaya and Alexander Page in Prof. Uher's group at University of Michigan. A series of clathrate samples $Ba_8Cu_5Si_xGa_{41-x}$ came from Prof. Paschen's group from Vienna University of Technology and were prepared by Dr. Xinlin Yan. $Ba_8Ga_{16}Ge_{30}$ and Co-

doped clathrates were synthesized by myself. I also measured ^{63}Cu and ^{65}Cu NMR on a series of $Ba_8Cu_xGe_{46-x}$ samples prepared by the former group members and the results were published elsewhere [94] but not described in this thesis.

4. EXPERIMENTAL RESULTS AND DISCUSSIONS*

4.1 Type-I $Ba_8Ga_{16}Ge_{30}$ Clathrate

It has been shown in our group that in type-I $Ba_8Ga_{16}Sn_{30}$ [47] a low-temperature broad peak in the Ga NMR spin-relaxation rates is associated with a mechanism due to strongly anharmonic off-center Ba rattling. Analyzing the corresponding behavior was one of the main motivations for this study to examine the vibrational behavior in the analogous material $Ba_8Ga_{16}Ge_{30}$, known for its high thermoelectric zT. Here, I synthesized a $Ba_8Ga_{16}Ge_{30}$ sample and utilized the same procedure as in Ref. [47] for the $Ba_8Ga_{16}Ge_{30}$ NMR measurements to separate the quadrupole and magnetic contributions to the relaxation rates. Although $Ba_8Ga_{16}Ge_{30}$ is also believed to have anharmonic behavior [33, 29], the results indicate rather different behavior in the NMR with an enhanced contribution at high temperatures. In addition, Ba NMR shows a large contribution of Ba orbits to the conduction band. A report of this work was already published and the results are reprinted from [101].

*Part of this section is reprinted with permission from "Pseudogap and anharmonic phonon behavior in $Ba_8Ga_{16}Ge_{30}$: An NMR study," A. A. Sirusi and J. H. Ross, Jr., *J. Chem. Phys.*, vol. 145, p. 054702, 2016. Right managed by AIP publishing LLC.

*Part of this section is reprinted with permission from "NMR study of $Ba_8Cu_5Si_xGe_{41-x}$ clathrate semiconductors," A. A. Sirusi *et al.*, *Phys. Chem. Chem. Phys.*, vol. 17, p. 16991, 2015. Reproduced by permission of the PCCP Owner Societies.

*Part of this section is reprinted with permission from "Synthesis, transport and magnetic properties of Ba-Co-Ge clathrates," A. A. Sirusi and J. H. Ross, Jr., *J. Electron. Mater.*, vol. 45, p. 1094, 2016. Copyright (2015), The Minerals, Metals & Materials Society.

*Part of this section is reprinted with permission from "Low-temperature structure and dynamics in Cu_2Se," A. A. Sirusi *et al.*, *J. Phys. Chem. C*, vol. 119, p. 20293, 2015. Copyright (2015) American Chemical Society.

*Part of this section is reprinted with permission from "Band ordering and dynamics of $Cu_{2-x}Te$ and $Cu_{1.98}Ag_{0.2}Te$," A. A. Sirusi *et al.*, *J. Phys. Chem. C*, vol. 120, p. 14549, 2016. Copyright (2016) American Chemical Society.

4.1.1 Sample Preparation

I prepared a polycrystalline $Ba_8Ga_{16}Ge_{30}$ sample from pure elements [Ge (pieces, 5N), Ga (ingot, 4N), and Ba (rod, 2N5)] with excess (4%) barium, and arc melted in an argon environment following by annealing in a BN crucible for one day at 950°C and then three days at 700°C in an evacuated sealed quartz tube. Figure 4.1 shows the powder XRD pattern and refinement. The structure of the major phase is type-I clathrate (space group $Pm\bar{3}n$ with a lattice constant $a = 10.7841$ Å) with only a small amount of Ge impurity. Wavelength dispersive spectroscopy (WDS) measurements were carried out on four points in one piece of the pulverized sample. The average results of WDS yielded the composition $Ba_{7.89}Ga_{15.21}Ge_{30.79}$.

Hall coefficient and resistivity measurements were performed in a Quantum design Physical Property Measurement System. Based on the Hall results, a simple one-band model results in $n = 3.95 \times 10^{20}$ cm^{-3} at room temperature. If we apply the Zintl concept [102] (Ba^{2+}, Ga^{-1}) to the WDS results we obtain $n = 4.5 \times 10^{20}$ cm^{-3} in good agreement with the Hall measurement result. The resistivity vs temperature (inset in Figure 4.1) shows behavior characteristic of an n-type heavily doped semiconductor.

For comparison of the Ba contribution to the conduction band, we also have measured Ba NMR on a $Ba_8Ga_{16}Sn_{30}$ sample. The sample preparation method for the $Ba_8Ga_{16}Sn_{30}$ sample was reported in Ref. [47] and this sample was the same as measured in that reference.

4.1.2 NMR Results and Analysis

Figure 4.2 shows ^{71}Ga spectra of the $Ba_8Ga_{16}Ge_{30}$ sample obtained at 4.2 K, 77 K, and 290 K. Similar spectra (not shown) were obtained for ^{69}Ga. The line shapes are superpositions of $m = 1/2$ to $-1/2$ transitions of the three different Ga sites (6*c*, 16*i*, 24*k* in the type-I structure).

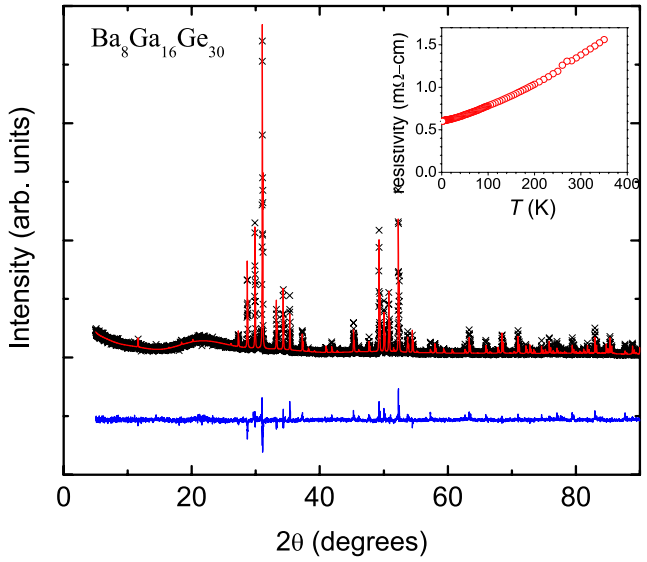

Figure 4.1: Powder XRD spectrum at room temperature for $Ba_8Ga_{16}Ge_{30}$ along with results of refinement and difference plots. Inset: resistivity vs T. Reprinted from [101].

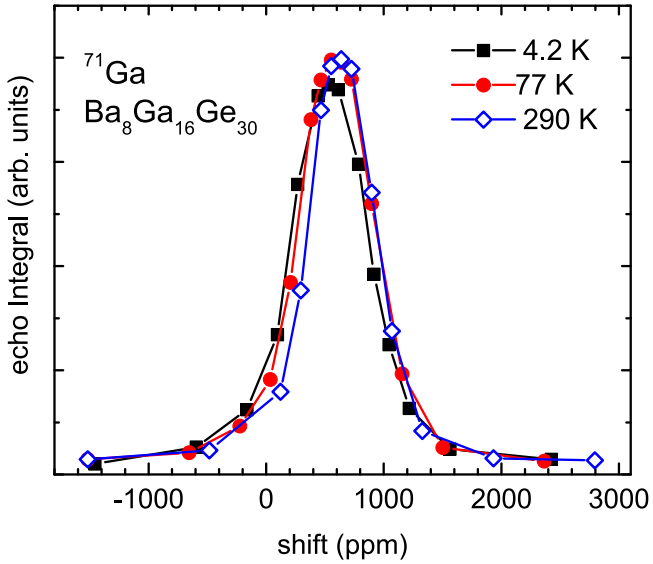

Figure 4.2: ^{71}Ga spectra measured at 4.2 K, 77 K, and 290 K for the $Ba_8Ga_{16}Ge_{30}$ sample. Reprinted from [101].

Table 4.1: ^{71}Ga magnetic NMR shifts (δ_{total}), Knight shift (K), magnetic relaxation time (T_{1M}), and Korringa values at 4.2 K, 77 K, and 290 K for the $Ba_8Ga_{16}Ge_{30}$ sample. Reprinted from [101].

	4.2 K	77 K	290 K
δ_{total} (ppm)	597	616	665
K	305	326	375
T_{1M} (s)	7.12	0.36	0.07
$K^2T_{1M}T$ (sK)	2.65 $\times 10^{-6}$	2.94 $\times 10^{-6}$	2.85 $\times 10^{-6}$

The magnetic and quadrupole shift contributions were extracted from the line shape centers of mass for each nucleus using $\Delta f/f_0 = \delta_{total} + BQ^2$, where δ_{total} is the magnetic shift, B is a constant, and Q is the nuclear quadrupole moment.

Table 4.1 shows the resulting magnetic shifts at different temperatures. The quadrupole shifts due to the second-order quadrupole mechanism give small negative shifts less than -3 kHz (-26 ppm) for ^{71}Ga, similar to the results for Cu NMR in the $Ba_8Cu_5Si_yGe_{41-y}$ samples [103] (see Section 4.2). For determining contributions in the magnetic shifts, we used the 4.2 K value of this shift to calculate the difference at other temperatures. The resulting magnetic shift δ_{total} can be further separated [92, 104] into a Knight shift and chemical shift ($\delta_{total} = K + \delta_{cs}$), where here we identify δ_{cs} as the contribution due to orbital effects, vs K which is due to conduction electron spins (and which will depend on sample doping). To separate the latter contribution we utilized the relaxation times as described below.

As was mentioned in Section 2.7 the relaxation times (due to a distribution of local environments) were obtained by fitting the nuclear magnetization recovery curve to a stretched multi-exponential function. The stretched multi-exponential function exponent is β. The initial results for both ^{71}Ga and ^{69}Ga relaxation times showed that the β values for all temperatures could be fitted to 0.64 (within the range of ± 0.04). Therefore, we used

the fixed $\beta = 0.64$ for all Ga relaxation recovery curve fittings.

The extracted spin-lattice relaxation rates can be separated into magnetic ($1/T_{1M}$) and quadrupole [47] terms ($1/T_{1Q}$) by using the characteristic Q and γ dependencies: $1/^{69,71}T_1 = A\gamma^2_{69,71} + BQ^2_{69,71}$, where A and B are constants to be fitted at each temperature, while γ and Q are known constants. The phonon contribution (quadrupole mechanism) and carrier dominated term (magnetic) obey $1/T_{1Q} \propto Q^2$ and $1/T_{1M} \propto \gamma^2$, respectively, thus measurements for the two nuclei can be used to obtain the separated values with the uncertainties determined by those of the T_1 measurements. $1/T_{1M}$ and 1/T_{1Q} obtained from this procedure are shown in Figure 4.3.

Note that in Ref. [105], the T_1 curves for the $Ba_8Ga_{16}Ge_{30}$ sample were fitted to a sum of multi-exponential curves attributed to crystallographic site occupancies of Ga. The resulting curves are similar to a stretched multi-exponential, and we find for example that our fitted T_1 is very close to the mean T_1 value obtained by fitting the data to a sum of two multi-exponential functions. However, we focused on the additional information obtained by separation the magnetic and quadrupolar parts, as described below.

The magnetic relaxation rates can be fitted to a parabolic pseudogap [106, 107] equation,

$$1/T_{1M} = aT + bT^3, \tag{4.1}$$

where $a = 0.0351$ $\mathrm{K^{-1}s^{-1}}$ and $b = 1.7 \times 10^{-7}$ $\mathrm{K^{-3}s^{-1}}$ obtained from the fit. Equation 4.1 can be derived by expanding the density of states, $g(E) = g_0 + g'(E - E_F) + \frac{1}{2}g''(E - E_F)^2$ in the vicinity of the Fermi energy (E_F) for the *s*-electrons [108]:

$$1/T_{1M} = \beta_S g_0^2 k_B T + \beta_S g_0 g'' \frac{\pi^2}{3}(k_B T)^3, \tag{4.2}$$

where $\beta_S = (64/9)\pi^3\hbar^3\gamma_e^2\gamma_n^2\left\langle\left|\Psi_s(0)\right|^2\right\rangle^2_{E_F}$, and $\left\langle\left|\Psi_s(0)\right|^2\right\rangle_{E_F}$ is the averaged square of

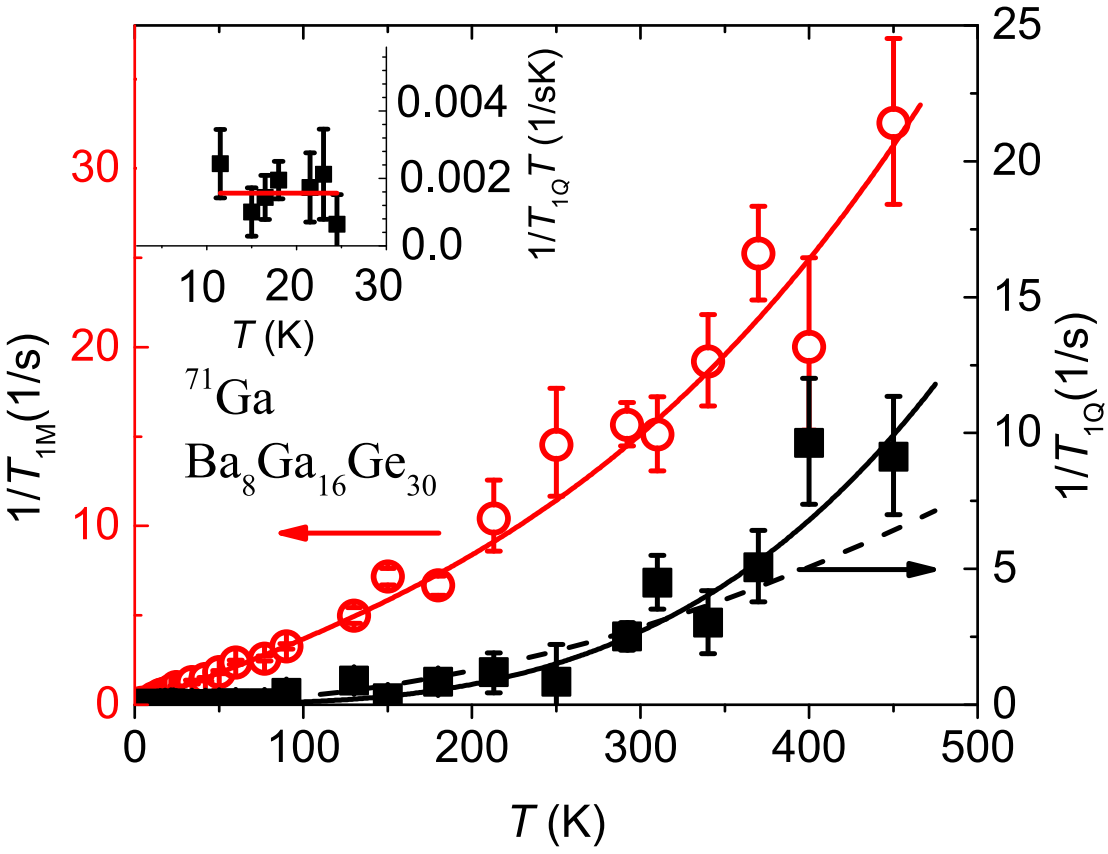

Figure 4.3: $1/T_{1M}$ (magnetic spin-lattice relaxation contributions) and $1/T_{1Q}$ (quadrupole contributions) as a function of temperature. The lines are fitted curves as explained in the text. The dashed line is the T^2 fit. The inset shows $1/TT_{1Q}$ below 30 K. Reprinted from [101].

the wave function at the nucleus over the Fermi surface. The magnetic relaxation rates indicate a parabolic dependence of $g(E)$ around E_F with $g_0 = 0.0087$ 1/(eV atom) and $g''/g_0 = 198$ eV^{-2} (note that we used the Ga Fermi-contact hyperfine field [92] H_s^{HF} 6.2 MG). The Knight shifts also can be expressed as [108]

$$K = K_0\Big(1 + \frac{\pi^2}{6}(k_B T)^2\Big[\frac{g''}{g_0} - \Big(\frac{g'}{g_0}\Big)^2\Big]\Big), \tag{4.3}$$

where $K_0 = (4/3)\pi\hbar^2\gamma_e\big\langle\big|\Psi_s(0)\big|^2\big\rangle_{E_F} g_0$. Note that equation 4.3 contains a term which depends on g', whereas Eqn. 4.2 is independent of g'. Furthermore, only when $g' = 0$ is the product $K^2T_{1M}T$ generated from these two expressions temperature-independent, and in that case the product reduces to the usual Korringa product [90, 92], which is $K^2T_{1M}T = 2.8 \times 10^{-6}$ sK for ^{71}Ga. To test for this condition, we first assumed the Korringa product to have this value, and obtained the chemical shift ($\delta_{cs} = \delta_{total} - K$) using the resulting K along with the experimental δ_{total}. This procedure yielded nearly identical values of δ_{cs} as expected (variation of 3%), an indication that indeed $g' = 0$ is a good model in this case, with the temperature dependence coming from the g'' term. Finally we replaced δ_{cs} by the mean value obtained this way, $\delta_{cs} = 290$ ppm, yielding values for K and $K^2T_{1M}T$ given in Table 4.1. The chemical shift thus extracted is very close to that (Ref. [47]) of $Ba_8Ga_{16}Sn_{30}$ [Table 4.2]. From the positive T^3 coefficient b [Eqn. 4.1], we thereby determine that E_F is at a minimum point in $g(E)$, corresponding to a pseudogap configuration. As a characterization of the shape of this pseudogap, the fitted parabolic rise in $g(E)$ would reach $2g_0$ at energies corresponding to a width of 0.2 eV.

Note that an increase in T_1^{-1} vs temperature comparable to our ^{71}Ga results was displayed for ^{71}Ga NMR in a similarly doped $n = 2 \times 10^{20}$ cm^{-3} sample [105], although the result was not analyzed for pseudogap in that work. This behavior thus appears to be a general feature of $Ba_8Ga_{16}Ge_{30}$ materials with these doping levels. On the other hand,

Table 4.2: Lattice constants (a), Ga NMR chemical shifts ($^{\mathrm{Ga}}\delta_{cs}$), ^{137}Ba T_1 (for 77 K at the peak positions), and total Ba shift ($^{\mathrm{Ba}}\delta_{total}$) for $Ba_8Cu_5Ge_{41}$ obtained from two-site quadrupole fit, $Ba_8Ga_{16}Ge_{30}$, and $Ba_8Ga_{16}Sn_{30}$ [47] obtained by fitting to single Gaussians. Reprinted from [101].

compounds	a (Å)	$^{\mathrm{Ga}}\delta_{cs}$ (ppm)	^{137}Ba T_1 (ms)	$^{\mathrm{Ba}}\delta_{total}$ (ppm)
$Ba_8Cu_5Ge_{41}$	10.692	–	1042	1390
$Ba_8Ga_{16}Ge_{30}$	10.784	290	140	1690
$Ba_8Ga_{16}Sn_{30}$	11.585	300	3220	515

in a sample with [109] $n = 8.7 \times 10^{19}$ cm^{-3}, $1/T_{1M}$ instead was observed to increase with decreasing temperature, with temperature dependence comparable to what has been reported for GaAs at doping levels just below the metal-insulator transition [110]. Thus we assume the mobility edge is close to the latter value of carrier density based on the similarity to what is observed in GaAs, whereas for the present more heavily doped sample the Korringa behavior indicates more standard metallic behavior. Turning to the quadrupole contribution, $1/T_{1Q}T$, also plotted in Figure 4.3, we see that there is no low-temperature peak in relaxation rate, such as was observed in the rattler system $Ba_8Ga_{16}Sn_{30}$, which exhibits a broad peak [47, 111] near 10 K. Since atomic vibrations are coupled most strongly to the nuclei through the electric quadrupole hyperfine fields, the separated $1/T_{1Q}T$ contribution provides a particularly sensitive test for such oscillations. As seen in the inset of Figure 4.3, $1/T_{1Q}T$ does remain unexpectedly nonzero at the lowest observed temperatures, however the values are quite small, and the results approach a constant rather than exhibiting a rattler peak.

In contrast to the lack of a low-temperature rattler peak, at high temperatures $1/T_{1Q}T$ rises quite rapidly, a result which may signify strong anharmonicity for the propagating phonons, as shown below. In order to characterize the behavior, we fitted $1/T_{1Q}T$ to a

function T^n, giving the curve shown in Figure 4.3. This fitting gives $1/T_{1Q} \propto T^{3.2\pm0.3}$. This temperature dependency does not follow the usual power law as expected in a Debye model [112]:

$$\frac{1}{T_{1Q}} \propto Q^2 \Big(\frac{T}{\Theta_D}\Big)^7 \int_0^{\Theta_D/T} \frac{e^x x^6}{(e^x-1)^2} dx, \tag{4.4}$$

where Θ_D is the Debye temperature. Eqn. 4.4 approaches a T^2 limit. Van Van Kranendonk and Walker [113] also showed that the anharmonic Raman process yeilds T^2 temperature dependance but with an stronger amplitude. However it has been shown [112, 114] that with the presence of further anharmonic terms the usual 2-phonon relaxation process can also become superseded at high temperatures by a multi-phonon term with $1/T_{1Q}$ proportional to T^3 or T^4. Note that the original Khutsishvili [115] (T^4) term has been shown to be not correct, but little work bas been done based on the Zamar *et al.* [114] proposal for molecular crystals. The latter model applies to systems with asymmetric bonding such as the clathrates as described here, therefore it should apply, but these seem to be some open questions here. In cubic semiconductors, T^2 behavior is typically observed over a wide temperature range, for example [116] through 1000 K in InAs. Thus, the fitted $1/T_{1Q} \propto T^{3.2\pm0.3}$ is anomalous, and we assign this result to a crossover to an enhanced high-temperature anharmonic term. In addition, the magnitude of the high-temperature $1/T_{1Q}$ is large compared to other semiconductors, which helps to confirm the presence of an additional quadrupole relaxation mechanism. To compare magnitudes, we replaced the multi-exponential appropriate for magnetic relaxation with a stretched single-exponential, essentially giving the mean T_1 exponent. The ^{71}Ga result, for example at 300 K, is $1/T_{1Q} = 13$ s^{-1}, which can be compared to ^{71}Ga rates in GaAs [117], GaSb [117], and GaN [118] of $1/T_{1Q} = 3$, 2.5, and 1 s^{-1} respectively.

A ^{137}Ba NMR spectrum for the $Ba_8Ga_{16}Ge_{30}$ sample, at 77 K, is shown in Figure 4.4 by the solid triangles. This spectrum is a superposition of two types of Ba cage (sites

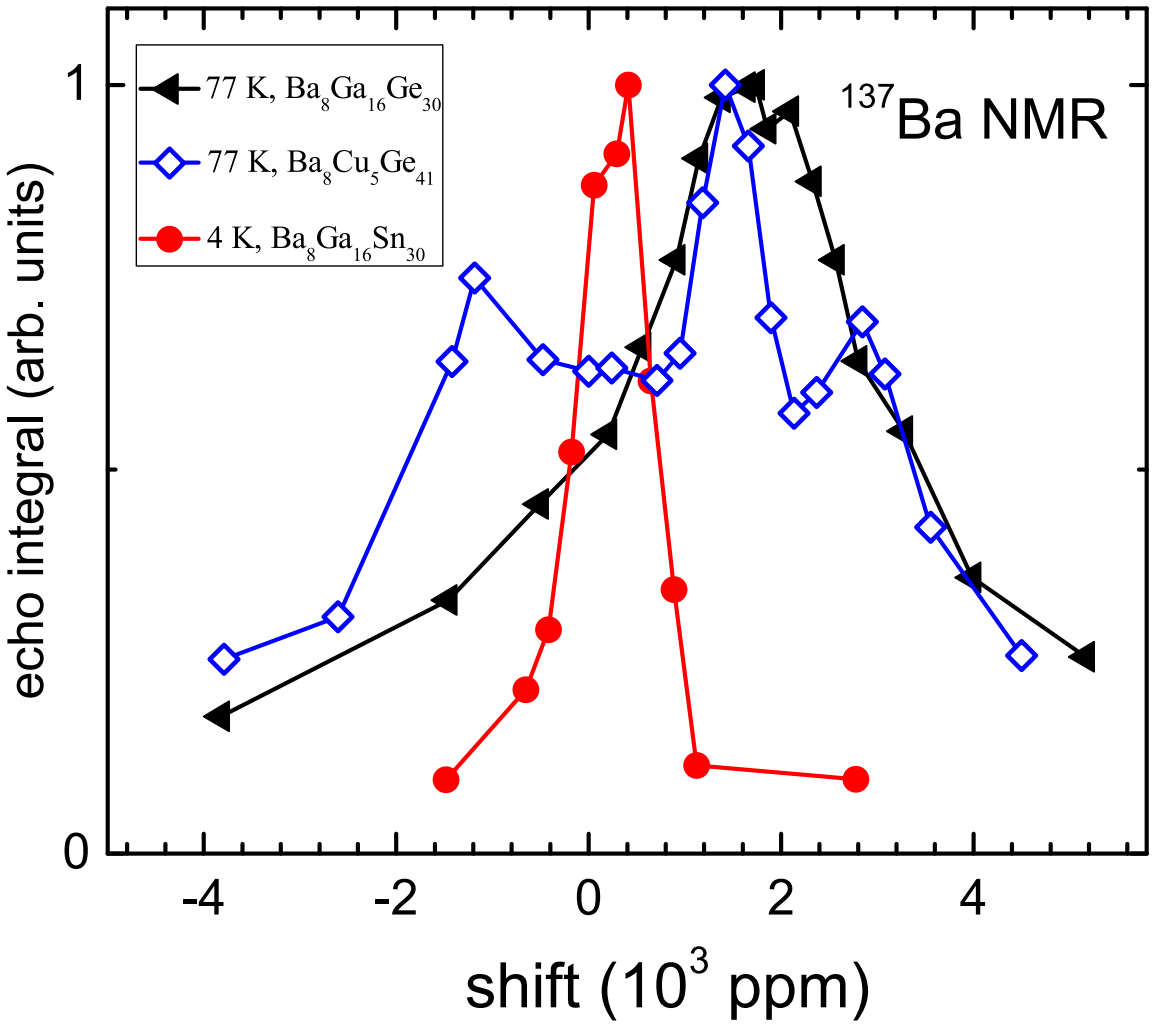

Figure 4.4: ^{137}Ba NMR spectrum measured at 77 K for $Ba_8Ga_{16}Ge_{30}$, along with that of $Ba_8Ga_{16}Sn_{30}$ at 4 K and results for $Ba_8Cu_5Ge_{41}$ at 77 K. Reprinted from [101].

2*a* and 6*d*). To compare with this line shape, we also measured the 4 K ^{137}Ba spectrum of $Ba_8Ga_{16}Sn_{30}$ (filled circles in the figure; sample characteristics reported in Ref. [47]), and we also display the ^{137}Ba spectrum of a $Ba_8Cu_5Ge_{41}$ sample (open diamonds: see Section 4.2).The smaller shift and narrow Ba resonance for $Ba_8Ga_{16}Sn_{30}$ corresponds to its larger lattice constant, clearly showing the weak interaction of Ba with the framework atoms, and thereby the smaller quadrupole broadening. $Ba_8Cu_5Ge_{41}$ has small cages and an ordered arrangement of Cu atoms [103], and exhibits a superposition of two well-defined spectra for the two cages as shown in Section 1.1.3, including a large quadrupole broadening for the 6*d* site. A detailed fit for this spectrum is described in Section 4.2. By contrast, the lack of structure for the case of $Ba_8Ga_{16}Ge_{30}$ presumably reflects a superposition of many arrangements of Ga ion neighbors, while the large shift reflects a significant participation of Ba in the conduction band, as shown below.

The ^{137}Ba relaxation times sampled at the center of each spectrum of Figure 4.4 at 77 K are given in Table 4.2. T_1 is the largest for $Ba_8Ga_{16}Sn_{30}$, and while we have not assessed the size of its rattling-type quadrupole contribution [47] in the Ba NMR, clearly the carrier-related Korringa contribution for this sample is small. By contrast, the much shorter T_1 for $Ba_8Ga_{16}Ge_{30}$ indicates a much larger Korringa contribution. This is made clear by noting that typical Ba chemical shifts [119] are between 100 to 500 ppm which means the large shift for $Ba_8Ga_{16}Ge_{30}$ is largely due to carriers (Knight shift). For $Ba_8Ga_{16}Ge_{30}$ the 77 K quadrupole contribution to T_1^{-1} is expected to be very small (compare the Ga NMR results in Figure 4.3), so we also assume that the observed T_1 is entirely magnetic in origin. Using the Korringa product $K^2T_1T = 21 \times 10^{-6}$ sK for the ^{137}Ba nucleus, we obtain $K = 1400$ ppm, so that the remainder of the observed shift, 460 ppm, can be assigned as a chemical shift. These results are sensible but with some uncertainties due to assumed lack of Korringa enhancement.

4.1.3 Discussion

The Korringa T_1^{-1} (and corresponding Knight shift), identified above, can also be used to obtain the Ba *s*-electron contribution to the local density of states, using the Ba hyperfine field [120] $H_s^{HF} = 3.6$ MG. Since [92] $K = H_s^{HF}\mu_B g_s(E_F)$, we obtain $g_s(E_F) = 0.067$ (eV atom)$^{-1}$. Compared to $g_0(E_F) = 0.0087$ (eV atom)$^{-1}$ at the bottom of the pseudogap, obtained for the Ga sites as noted above, the *s*-contribution for Ba is 7.7 times larger, implying a very large fractional contribution due to Ba *s*-states in the conduction band. As was discussed before, estimating the *s*-contribution for Ba by using H^{HF} values from the literature involves some uncertainty (on order of 10-20%) due to assumed lack of Korringa enhancement and constancy of H^{HF} [121, 122]. The Ba contribution is significantly larger than that of Ga, outside this range of uncertainty.

Previous electronic structure calculations [123] for $Ba_8Ga_{16}Ge_{30}$ have indicated a large Ba contribution to the conduction band density of states, including [124] a Ba *d*-dominated peak in a relatively narrow energy region. A recent result [125] also indicates that Ba *s*-states play a significant role in the region just above the gap. The present results confirm a large Ba contribution, and show that the framework contribution (at least that of Ga atoms) is in fact considerably smaller than that of the Ba states. A large Ba $g(E_F)$ peak, combined with the pseudogap observed in the framework states, has the characteristics typically associated with *s*-*d* hybridization gap behavior [126], which may further depress the framework contribution in this case. The observed pseudogap must have a significant effect on the thermoelectric properties.

Returning to the enhanced phonon contribution to the Ga quadrupole T_1, the mechanism [114] relies on enhanced anharmonicity of the propagative phonon modes, throughout *k*-space rather than a single localized mode, with no dependence on phonon velocity. Recently several reports have focused on the contributions of these effects toward lowering

the thermal conductivities. In silicon clathrates [127] model calculations have shown that the clathrate structure itself tends to induce enhanced anharmonicity as well as lowered propagation velocity, while in $Ba_8Ga_{16}Ge_{30}$ [46] it has been proposed that presence of the Ba filler atoms strongly enhances the anharmonic contribution. A previous neutron scattering study [44] of $Ba_8Ga_{16}Ge_{30}$ focused on the anti-crossing of phonon levels near the frequency of the Ba vibrational mode, and showed that scattering by this mode alone could not account for the reduced thermal conductivity. On the other hand, a recent inelastic neutron study [128] of $Ba_8Ge_{40+x}Ni_{6-x}$ indicated a further hybridization of Ba-centered vibrational modes with propagative modes across a wide range of phonon energies, leading to a filtering effect which may contribute to the low thermal conductivity. This is similar to recent findings for a Si clathrate [45] based on computational and inelastic X-ray studies. By contrast to phonon hybridization processes, the mechanism [112, 114] leading to an enhanced phonon-contributed NMR T_1^{-1} relies upon a multi-phonon mechanism which depends specifically upon an inelastic phonon-phonon interaction. It is not clear from this how large is the contribution to the reduced thermal conductivity, however the present results indicate an enhancement of such anharmonic processes relative to the behavior of ordinary semiconductors. The NMR results provide experimental evidence for such an anharmonic contribution, while the contrast with the behavior of $Ba_8Ga_{16}Sn_{30}$ [47] illustrates directly the different contributions of localized vs propagating phonon modes in these materials.

4.2 Type-I $Ba_8Cu_5Si_xGe_{41-x}$ Clathrates

The NMR measurements of $Ba_8Cu_5Si_xGe_{41-x}$ compounds reported here are on samples that came from Prof. Silke Paschen's group at the Vienna University of Technology . These are from the same batch for which the preparation and characterization were done by Dr. Xinlin Yan and described in reference [35]. The motivation to perform

NMR on these samples has been the presence of earth-abundant elements and possibility that the Si-based clathrates can be used for solar cell applications [129]. Therefore, we carried out NMR measurements to better understand the changes in electronic behavior with increasing Si content. This also followed our previous work [94] on $Ba_8Cu_yGe_{46-y}$ ($y = 4, 5.3, 6$), which are not described in this thesis. NMR shifts can be particularly sensitive to hybridization effects in the conduction and valence bands, and we find that in the $Ba_8Cu_5Si_xGe_{41-x}$ materials with x increasing from zero through the $x = 18$ composition there is very little change in such behavior. However on further increase of x approaching $Ba_8Cu_5Si_{41}$ the behavior changes rapidly as the framework becomes more metallic as observed both by Cu and Ba NMR. A report of this work was already published and the results are reprinted from Ref. [103].

4.2.1 Sample Preparation

The synthesis involved melting the pure-elements, followed by annealing and hot pressing. Powder X-ray diffraction (XRD) and analysis provided full structural details of the samples, and dispersive X-ray spectroscopy was measured to determine the compositions of the samples (nominally $x = 0, 3, 6, 10, 13, 18, 25, 35, 41$) as reported in reference [35]. In this work, we will denote the samples as Si(x) according to these nominal compositions, although in analysis we used the WDS-measured compositions. The type-I clathrate structure, common to all compositions examined here, has 46 Cu/Ge/Si framework atoms per unit cell. In addition, 8 Ba guest atoms are situated on two cage sites: $2a$ (smaller dodecahedral cages) and $6d$ (tetrakaidecahedral cages) [29], this is the same as the $Ba_8Ga_{16}Ge_{30}$ structure discussed in the previous section. It has been shown [35, 130] at least for the end compositions ($x = 0, 41$), that Cu atoms occupy exclusively the $6c$ framework site (sometimes alternatively denoted as $6d$, Ref. [35]).

The previous measurements [35] also included detailed transport results, among which

the Hall-effect carrier densities will be used here. Note that the X-ray refinements show that the low Si content samples include small densities of vacancies, in contrast to the Si-rich side where there are no vacancies. This is typical of Si and Ge clathrates; the spontaneous vacancies tend to enforce electron balance (Zintl concept [102]) and thereby leading to reduced carrier concentration in Ge-based materials, although not as readily for Si clathrates. They also showed that, while the lattice constants of the compounds decease linearly with increasing Si content, some internal parameters such as Si occupation at the $24k$ site show nonlinear behavior vs composition.

4.2.2 NMR Results and Discussion

Figure 4.5 shows ^{63}Cu spectra of the nine $Ba_8Cu_5Si_xGe_{41-x}$ samples obtained at room temperature. Similar spectra (not shown) were obtained at 77 K, and for ^{65}Cu at both temperatures. The line shapes are $m = 1/2$ to -1/2 transitions as reported in previous studies on $Ba_8Cu_yGe_{46-y}$ [94] for $I = 3/2$ Cu nuclei. By examination of ^{63}Cu and ^{65}Cu line shapes we separated the magnetic and quadrupole shift contributions for each sample. Center of mass magnetic and quadrupole shifts were separated by using both the ^{63}Cu and ^{65}Cu centers of gravity and the relation $\Delta f/f_0 = \delta + BQ^2$, where δ is the magnetic shift (paramagnetic sign, by convention [131]), B is a constant, and Q is the nuclear quadrupole moment. Figure 4.6 shows the resulting magnetic shifts. The quadrupole shifts due to the second-order quadrupole mechanism give small negative shifts less than -3 kHz (or -30 ppm), similar to the results of Ref. [94] for $Ba_8Cu_yGe_{46-y}$ samples. The net magnetic shift δ can be further separated [92, 104] into a Knight shift and chemical shift ($\delta = K + \delta_{cs}$), where here we identify δ_{cs} as the contribution due to orbital effects, whereas K is due to conduction electron spins (and which will depend on sample doping). Separation of these terms will be discussed further below. As seen in Figure 4.6, δ is approximately independent of x up to Si(25), but it increases rapidly with x approaching the Si(41) composition,

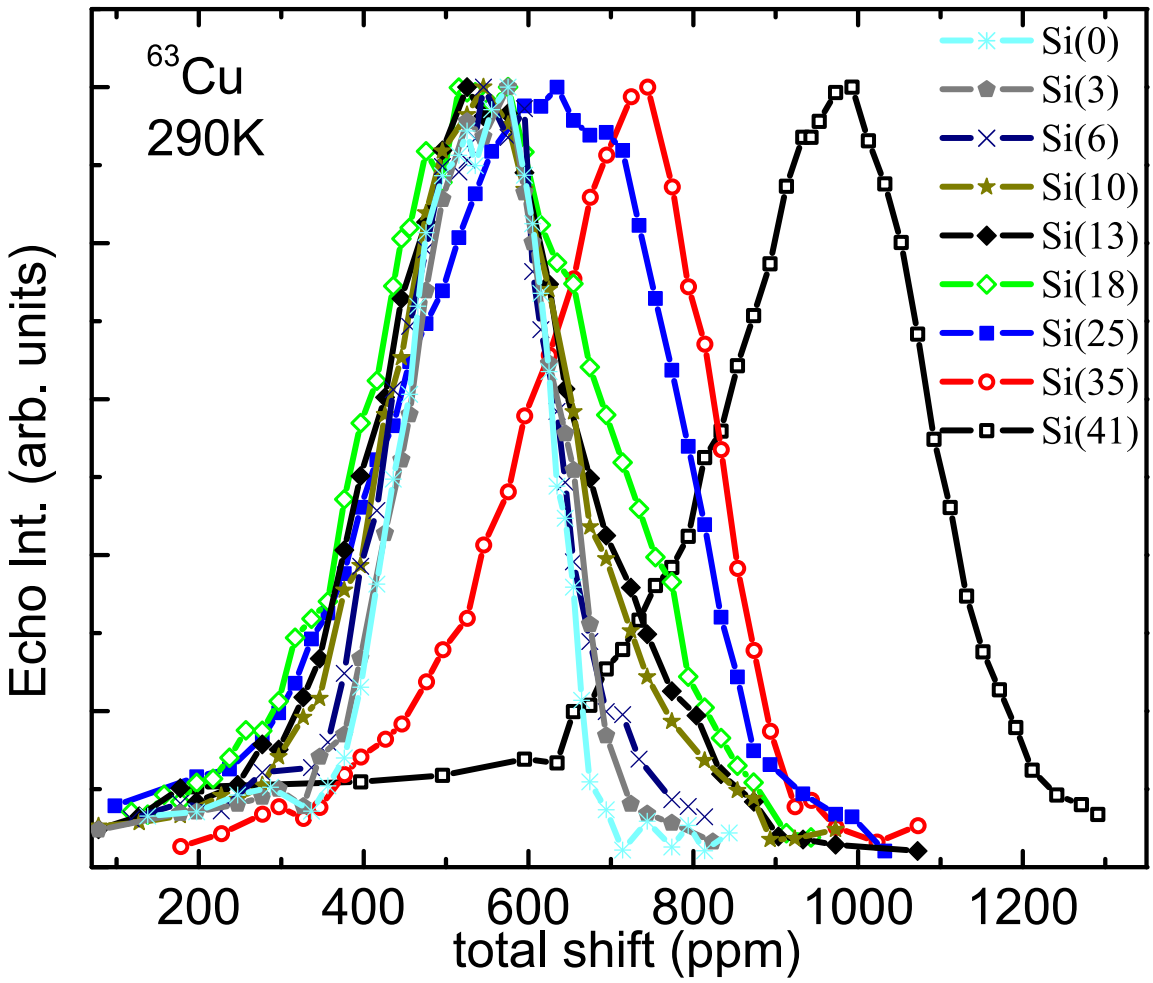

Figure 4.5: ^{63}Cu spectra measured at room temperature for all investigated $Ba_8Cu_5Si_xGe_{41-x}$ samples. Reproduced from Ref. [103].

indicating electronic behavior that is very sensitive to x close to this composition extreme.

The extracted spin-lattice relaxation rates ($1/T_1$) (as was mentioned in the previous section) can also be separated into two terms [47, 94], the magnetic and quadrupole relaxation rates as shown in Figure 4.7(a). The inset in this figure shows ${}^{63}T_1/{}^{65}T_1$ plus the limiting ratios of nuclear constants which indicate the dominant relaxation mechanism (horizontal lines labeled M and Q). If the quadrupole mechanism dominates, ${}^{63}T_1/{}^{65}T_1$ will be close to $({}^{65}Q/{}^{63}Q)^2$, and the inset shows that this occurs for Si(0) up to Si(18) at 290 K. Figure 4.7(b) shows the separated $1/T_{1Q}T$ for Si(0), Si(6), and Si(18) along with data for $Ba_8Cu_yGe_{46-y}$ ($y = 4, 5.3, 6$) as reported in Ref. [94]. The quadrupole rates are comparable in size and are typical for normal phonon behavior, which rise with temperature as shown schematically by the dashed line.

It is noted that the relaxation rates used in the analysis were obtained at the maximum intensity points of the line shapes although we do observe that T_1 changes across the lines. This is shown in Figure 4.8 for Si(41) and Si(18), giving the measured T_1 as a function of frequency. These frequency dependencies can be understood as due to distributions of Si/Ge and Cu atoms in the vicinity of the Cu sites. These random distributions of framework atoms also cause line shape broadening. To quantify this aspect the FWHMs of the ^{65}Cu line shapes obtained by fitting to a Gaussian function at room temperature are shown in Figure 4.9. The widths increase with increasing Si content up to Si(25) which is related to the random distribution of Si/Ge atoms on the 24k site which is the position of the nearest neighbors to Cu at the 6c site. The width is the largest for Si(25) since based on the WDS results it has an equal Si/Ge 24k occupancy ratio consistent with a random distribution. There is also an overall increase in width going from Si(0) to Si(41), due to increased electric field gradients (EFG)'s related to the gradual decrease in the lattice parameter.

$1/T_{1M}$ at the line-center position was separated at 77 K and at room temperature for

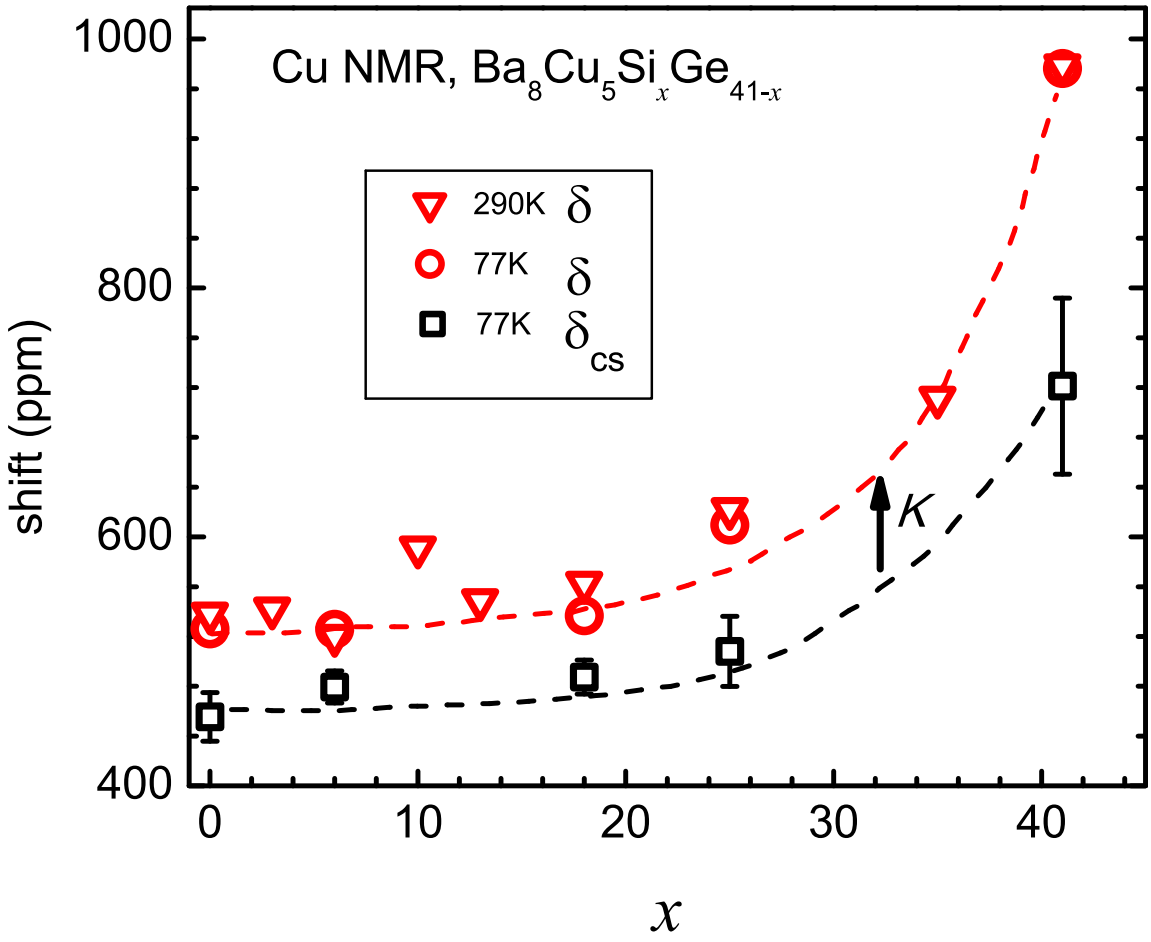

Figure 4.6: Magnetic shifts (δ, open circles and triangles at 77 K and 290 K respectively) and chemical shift component (δ_{cs}, open squares) as a function of Si content, plotted for Cu NMR in $Ba_8Cu_5Si_xGe_{41-x}$ at 77 K. Note that, the Knight shift is defined $K = \delta - \delta_{cs}$ (vertical arrow) as described in the text. The dashed lines are guides to the eyes. Reproduced from Ref. [103].

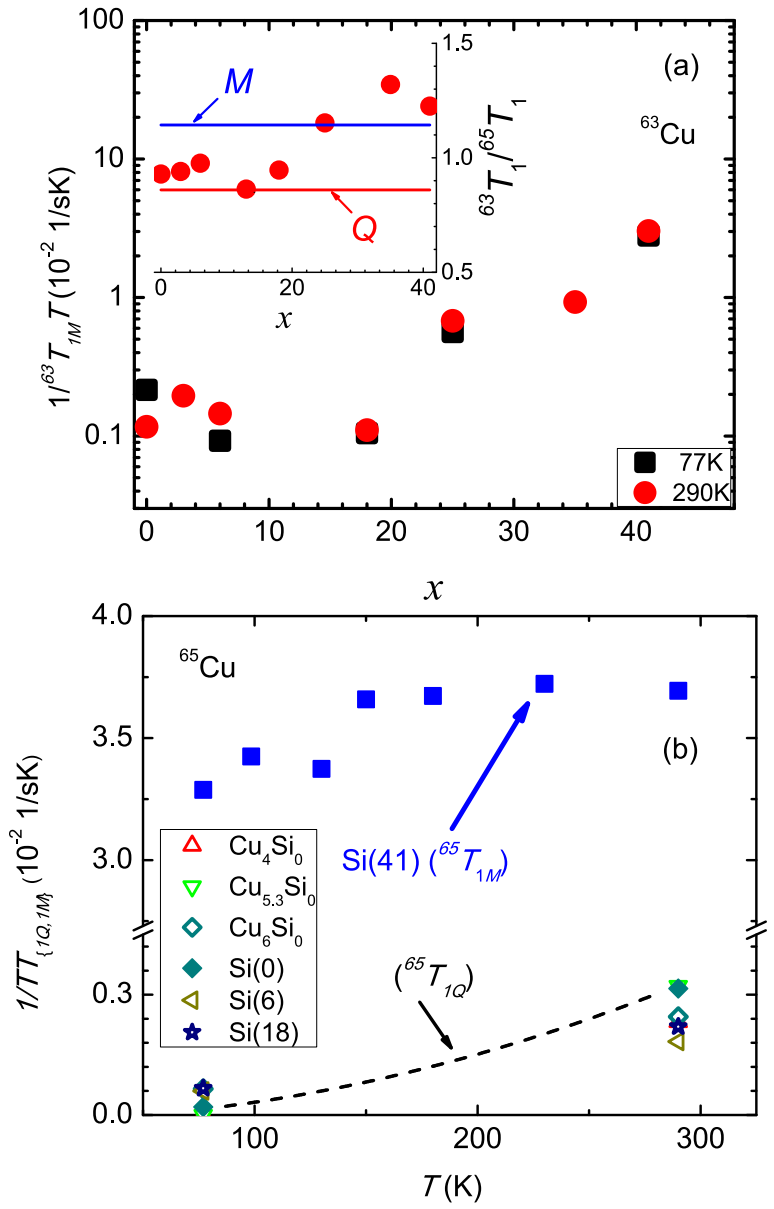

Figure 4.7: (a) magnetic spin-lattice relaxation contribution $1/TT_{1M}$ as function of Si content in $Ba_8Cu_5Si_xGe_{41-x}$ at 77 K and 290 K. The inset shows the $^{63}T_1/^{65}T_1$ ratio at 290 K with the magnetic ($^{63}T_1/^{65}T_1 = (^{65}\gamma/^{63}\gamma)^2$) and quadrupolar ($^{63}T_1/^{65}T_1 = (^{65}Q/^{63}Q)^2$), labeled M and Q, respectively. Horizontal lines are the magnetic and quadrupoar limits. (b) Quadrupole contribution $1/TT_{1Q}$ vs temperature for Si(0), Si(6), Si(18) samples and $Ba_8Cu_yGe_{46-y}$ ($y = 4, 5.3, 6$) samples from Ref. [94]. For comparison $1/TT_{1M}$ of the Si(41) sample is also plotted. Reproduced from Ref. [103].

the 5 samples for which the carrier densities were also previously measured [35]. The results show that $T_{1M}T \approx$ constant, as expected for a relaxation mechanism dominated by conduction electrons. Previously [94] it was shown that for 3 samples of $Ba_8Cu_yGe_{46-y}$ ($y = 4, 5.3, 6$) with different carrier densities, the shift could be treated as $\delta = \delta_{cs} + K$, with $\delta_{cs} = 475$ ppm, and with the product $K^2T_{1M}T \approx 1.2 \times 10^{-6}$ sK. The latter is the Korringa product [90] for metallic NMR shifts, with the measured value somewhat reduced relative to the value $K^2T_{1M}T = 3.73 \times 10^{-6}$ sK for metals in the absence of electron-electron interactions. The small difference is similar to results in Si:P, where it was attributed to the presence of a small amount of disorder at the bottom of the conduction band [132]. For the present $Ba_8Cu_5Ge_{41}$ sample (Si(0)), assuming $\delta_{cs} = 475$ ppm (77 K data) also yielded $K^2T_{1M}T = 1.2 \times 10^{-6}$ sK, identical to the results obtained for previous samples. Using this value for the Korringa product, and thereby calculating K from the extracted T_{1M} values, we find that δ_{cs} increases with the Si content to 536 ppm for Si(25), and to 790 ppm for Si(41). Alternatively, assuming a non-reduced $K^2T_{1M}T = 3.73 \times 10^{-6}$ sK, somewhat smaller δ_{cs} values are obtained; the resulting two sets of values are plotted in Figure 4.6 as the error-bar limits. Clearly, both δ_{cs} and K are nearly constant as the Si content increases to $x = 25$, indicating similar electronic behavior for these samples. On the other hand, significantly larger shifts in Si(41) indicate a modification of the conduction/valence band configuration involving Cu orbitals. This is true for both the metallic shift and δ_{cs} contributions for Si(41) (K is seen as the difference between δ and δ_{cs} plotted in Figure 4.6 illustrated by the vertical arrow).

^{137}Ba NMR spectra for the Si(0) and Si(41) samples at 77 K are shown in Figure 4.10. A comparison of the Si(41) spectrum to other Ba-containing clathrates was also given in the last section. These spectra were fitted as powder patterns assuming two sites: a narrow line (labeled site A) and a broad line (site B). Similar to the Cu NMR results, these fits yield separate magnetic shifts (δ) and second-order quadrupole components. Due to the

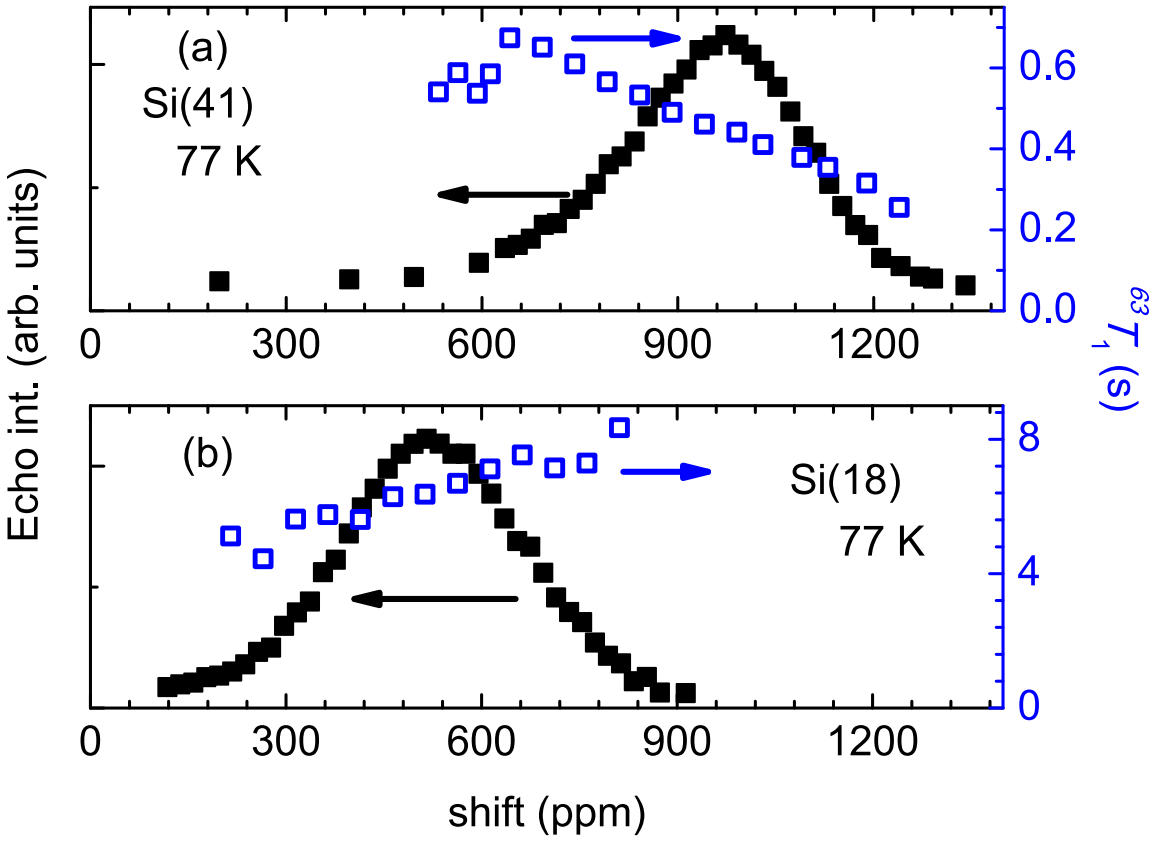

Figure 4.8: ^{63}Cu NMR Spectra and $^{63}T_1$ data vs shift for (a) Si(41) and (b) Si(18) samples at 77 K. Reproduced from Ref. [103].

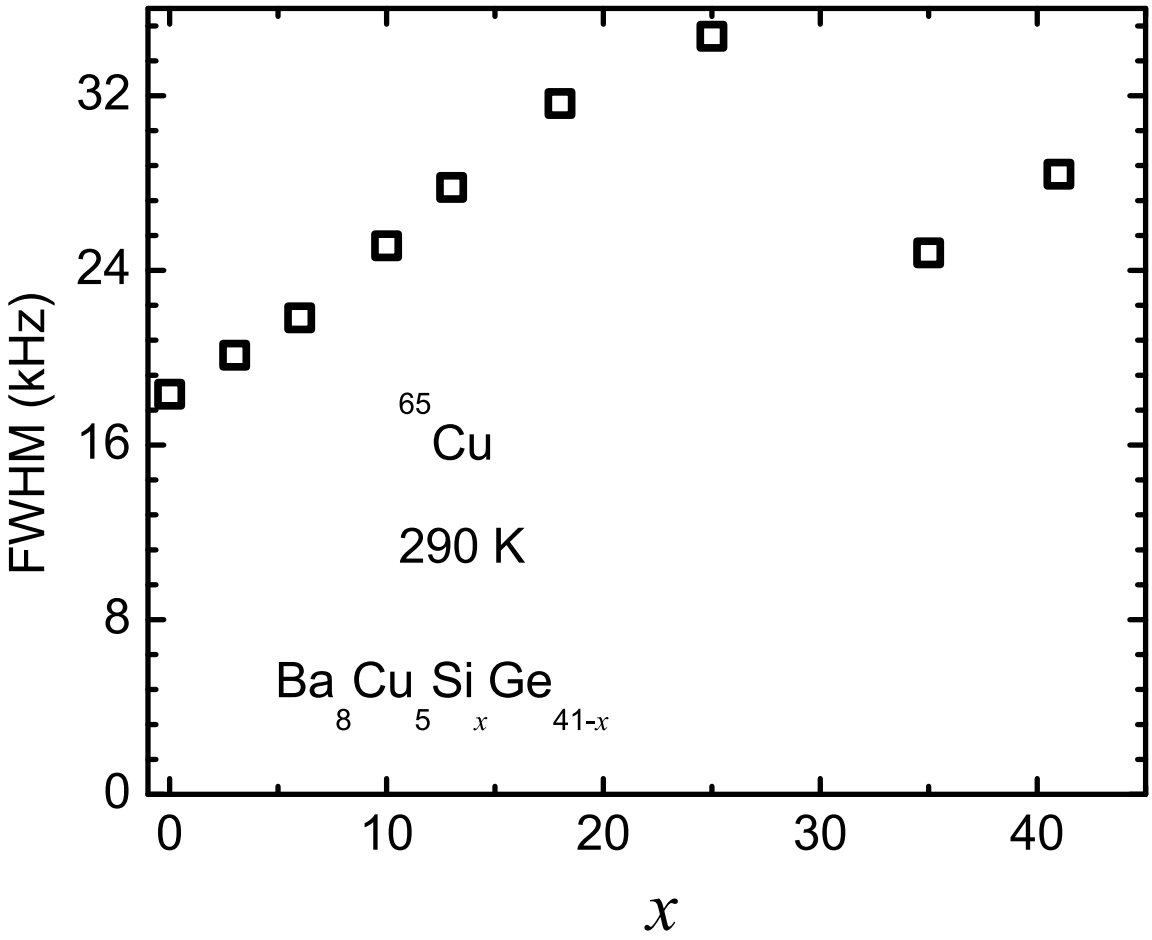

Figure 4.9: FWHM of ^{65}Cu NMR line of $Ba_8Cu_5Si_xGe_{41-x}$ samples at room temperature. Reproduced from Ref. [103].

Table 4.3: ^{137}Ba NMR parameters obtained from fitting Si(0) and Si(41) results at 77 K, along with the measured T_1. The definitions of the parameters are given in the text. Reproduced from Ref. [103].

	δ (ppm)	site	ν_Q (MHz)	η_Q	$^{137}T_1$ (ms)
Site A Si(0)	$2a$	1393	0	0	1042
Site B Si(0)	$6d$	1294	4±0.05	0.18±0.02	
Site A Si(41)	$2a$	1890	4.8±0.05	0.7±0.02	180
Site B Si(41)	$6d$	1825	11.77±0.06	0.71±0.02	

linewidths we included only isotropic magnetic shifts in the fits. The Si(0) middle peak is narrow so we assumed site A to have zero EFG, and fit it to a Lorentzian function. The extracted spectral weight ratios A/B of the two fitted lines for Si(0) and Si(41) are 0.337 and 0.319. In type-I clathrates the expected ratio for Ba sites 2a and 6d is $2/6 = 0.333$, in agreement with the fitted ratios if site A is assigned to Ba atoms in the smaller cage. The fitting parameters are given in Table 4.3 where ν_Q, is related to the EFG through $\nu_Q = 3eQV_{zz}/[2I(2I-1)h]$ and where V_{zz} is the largest principal EFG tensor component and I is the nuclear spin, while η_Q is defined as $\eta_Q = [V_{xx} - V_{yy}]/V_{zz}$. Note that the smaller EFGs for site A in both cases match the more symmetric environment of the smaller cage as expected. Moreover, the larger EFGs obtained for Si(41) correspond to its lower lattice constant compared to Si(0).

The Ba NMR T_1 values at the narrow peak positions are also given in Table 4.3. Similar to measured ^{135}Ba and ^{137}Ba relaxation rates in type-I $Na_xBa_ySi_{46}$ and chiral $Ba_{24}Ge_{100}$ clathrates, we assume that $^{137}T_1$ is dominated by the Korringa magnetic behavior [133, 134]. The larger shift and shorter $^{137}T_1$ for Si(41) clearly indicates more metallic behavior for this composition. Assuming that the 500 ppm Ba NMR shift difference between Si(0) and Si(41) samples is entirely due to a Knight shift for the Si(41) sample, using $^{137}T_1$ given

in Table 4.3 the Korringa product $K^2T_1T = 3.5\times10^{-6}$ sK is obtained, slightly smaller than 21×10^{-6} sK expected for ^{137}Ba without electron-electron interactions. These results are sensible but with some uncertainties due to assumed lack of Korringa enhancement. It is worth to mention that the magnetic shifts of the Si(0) and Si(41) samples are much smaller than in the superconducting [133] clathrate $Na_xBa_ySi_{46}$ (5930 ppm at 4.2 K) [133] and Ba metal [135, 136] (4030 ppm at room temperature). However, the enhanced Korringa contribution for Ba in $Ba_8Cu_5Si_{41}$ demonstrates a significantly greater participation of Ba in the conduction band in this material than in $Ba_8Cu_5Ge_{41}$.

As noted above, there is a small vacancy density in the Ge-rich compositions. XRD analysis showed that this occurs appreciably only in the Si(0) and Si(3) samples [35], for both of which compositions there are 0.1 vacancies per cell on 6c framework sites based on the XRD site occupations. This will affect the NMR resonance for ions in the close vicinity of vacancies. The immediate neighbors of these sites are 24k framework sites, which are not occupied by Cu, however those Ba and Cu ions occupying the same cage might also exhibit a weak split-off resonance. This was not seen in measurements for these two compositions, and it could be these sites are out of measurement range, as sometimes occurs near defects, however the main NMR shifts will not be affected.

The Knight shift for metals can be calculated according to (same as the first term of Eqn. 4.3 for the usual case with no pseudogap) [92]

$$K_{th} = \mu_B g_{tot}(E_F) H_s^{HF} \frac{g_s}{g_{tot}}, \tag{4.5}$$

where H_s^{HF} is the hyperfine field, assumed dominated by the s-contact interaction, $g_{tot}(E_F)$ is the density of states at the Fermi level and g_s/g_{tot} is the ratio of partial density of states of the local s orbital to the total $g(E_F)$. In the effective-mass approximation, assuming a parabolic band edge, $g_{tot}(E_F) = (3n/\pi^4)^{1/3} m^*/\hbar^2$. Here we used the atomic-

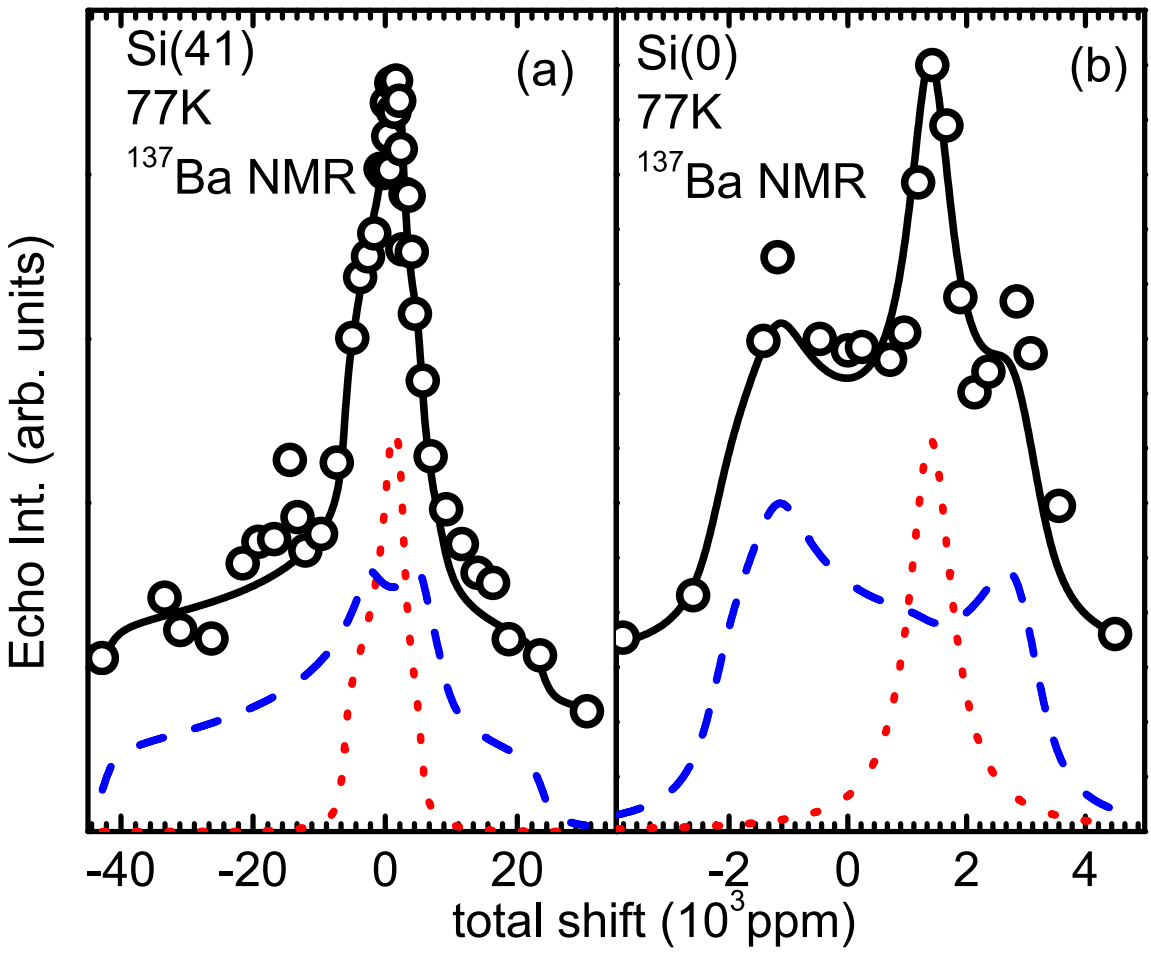

Figure 4.10: ^{137}Ba NMR spectra measured at 77 K, along with fitted spectra (solid curves), showing two fitted sites: 1) the dotted curve (site A) and 2) the dashed curve (site B) as explained in the text. (a) Spectrum of Si(41) sample. (b) Spectrum of Si(0) sample. Reproduced from Ref. [103].

Table 4.4: Measured carrier densities (n) and effective masses (m^*) from Ref. [35] with calculated Fermi energies (E_F), theoretical Cu Knight shifts (K_{th}), and K/K_{th} ratios from experiment. The latter is equivalent to g_s/g_{tot}, as explained in the text. Reproduced from Ref. [103].

compounds	n (10^{21}cm^{-3})	m^*/m_e	E_F (eV)	K_{th} %	K/K_{th} (g_s/g_{tot})
Si(0)	0.278	1.13	0.137	5.6	0.0013
Si(6)	0.855	1.44	0.228	10.2	0.0004
Si(18)	0.179	1.16	0.100	4.7	0.0010
Si(25)	0.809	1.35	0.235	8.9	0.0011
Si(41)	2.142	1.65	0.367	14.5	0.0017

based [92] $H_s^{HF} = 260$ T for Cu.

Table 4.4 shows E_F and Cu Knight shift (K_{th}) values obtained from this calculation, the latter made with the assumption that $g_s/g_{tot} = 1$ in equation (1), and with g_{tot} calculated per unit cell. Using K from the analysis above ($\delta - \delta_{cs}$, values plotted in Figure 4.6), we obtain the ratio K/K_{th} given in Table 4.4. K/K_{th} therefore corresponds to g_s/g_{tot}, the density of s states for a given Cu atom relative to the density of conduction states in the cell as a whole. For example, assuming that conducting states have the ideal sp^3 hybridization and equally distributed among the 46 framework atoms, this ratio will be $(1/4/46) = 0.0054$. The smaller values displayed in Table 4.4 indicate a reduced Cu s-contribution to the conduction band edge.

Previously from results in our group [94], g_s/g_{tot} was calculated to be 0.0014 based on first-principles methods for $Ba_8Cu_{5.3}Ge_{40.7}$; the value 0.0013 found here for $Ba_8Cu_5Ge_{41}$ (Si(0) sample) is in excellent agreement. The calculation for $Ba_8Cu_{5.3}Ge_{40.7}$ also indicated [94] that up to about 0.2 eV above the conduction band edge the effective mass approximation works well, with little change in the partial densities of states, while at higher energies multiple bands begin to participate. As shown in Table 4.4, this condition applies

to the Si(0) and Si(18) compositions since they have sufficiently low carrier densities; similar values of K/K_{th} for these compositions, as well as of m^*/m_e, provide an indication that the conduction states remain essentially unchanged with Si substitution up to at least $x = 18$. This behavior matches the nearly-constant Cu chemical shifts (Figure 4.6) across this range.

For Si(41) the measured carrier densities place E_F further into the conduction band than for the other samples, and the measured Cu K is correspondingly considerably larger. Note that DFT calculations [35] for $Ba_8Cu_6Si_{40}$ do not show a semiconducting gap as is found for $Ba_8Cu_{6-x}Ge_{40+x}$ results (Refs. [94, 137]). The accurate estimation of band gaps in such calculations can be difficult, and therefore experimental confirmation is important. Tentatively we conclude that the more metallic properties of Si(41) are indeed an indication of semimetallic behavior, and that the upturn in NMR shift close to full Si substitution corresponds to a crossing of states near E_F for compositions in this range. The chemical shifts reinforce this conclusion as discussed below.

The Cu chemical shift $\delta_{cs} \approx 700$ ppm for Si(41) is at the upper range of shifts observed in Cu molecular systems [138]. There are not many semiconductors for which a Cu δ_{cs} has been identified unambiguously, however, the cubic phase Cu_2Se has a vanishing K contribution by symmetry, and exhibits [139, 140] $\delta_{cs} = 220$ ppm (see Section 4.4.2.2 later in the thesis), significantly smaller than the results found here. The enhanced δ_{cs} in $Ba_8Cu_5Si_{41}$ is due to the paramagnetic mechanism as described below.

The chemical shift can be expressed to include a diamagnetic (shielding) and paramagnetic term [104], of which the latter is expressed as

$$\delta_{para} = \frac{\mu_B^2}{2} \sum_{i,j} \frac{\{\langle\psi_j|L_z|\psi_i\rangle \langle\psi_i|L_z/r^3|\psi_j\rangle + c.c.\}}{E_i - E_j}, \tag{4.6}$$

where ψ_i is a state in the conduction band, ψ_j is a filled state, and E_i and E_j are the

corresponding energies. The angular momentum matrix elements in the numerator are nonzero when states including the same local orbital are connected. This corresponds to hybridization of states across the gap. Hence, the enhanced δ_{cs} in Si(41) shows that Cu p states become more distributed between conduction and valence bands. This gives a more specific picture of the electronic changes responsible for the non-monotonic electronic transport previously observed.

We plot the Cu-ion nearest neighbor distances and bond angles extracted from the XRD reported results [35] in Figure 4.11, illustrating changes in the Cu local environment. With Cu atoms on the 6c sites, each enclosed by 4 nearest neighbors on 24k sites, the symmetry is nearly that of a regular tetrahedron (ideal bond angle 109.5°) distorted to give one smaller and one larger angle; the larger angle of these two is plotted in the figure. Strong non-linearity in both plots is related to previously identified structure features [35] connected to a change in the transport properties in going from Si(0) to Si(41). The monotonic decrease in bond length for most of the range corresponds to the decrease in the measured lattice constant. However this trend is reversed for large x with a longer bond on Si(41), apparently a weakening of the bond which coincides with the framework becoming more metallic, and the large increase in Cu NMR shifts. This also coincides with a stronger Ba participation in the conduction band, as seen from enhanced Ba NMR shifts and $1/T_1$.

4.3 Type-I and Chiral Ba-Co-Ge Clathrates

Co-doped clathrates have not been investigated as heavily as $Ba_8Ga_{16}Ge_{30}$ due in part to difficulties in the syntheses. In this study, I synthesized type-I and chiral Ba-Co-Ge clathrates. This section focuses on an analysis of physical properties from 2 K to 300 K. A report of this work was already published and parts are reprinted from [141].

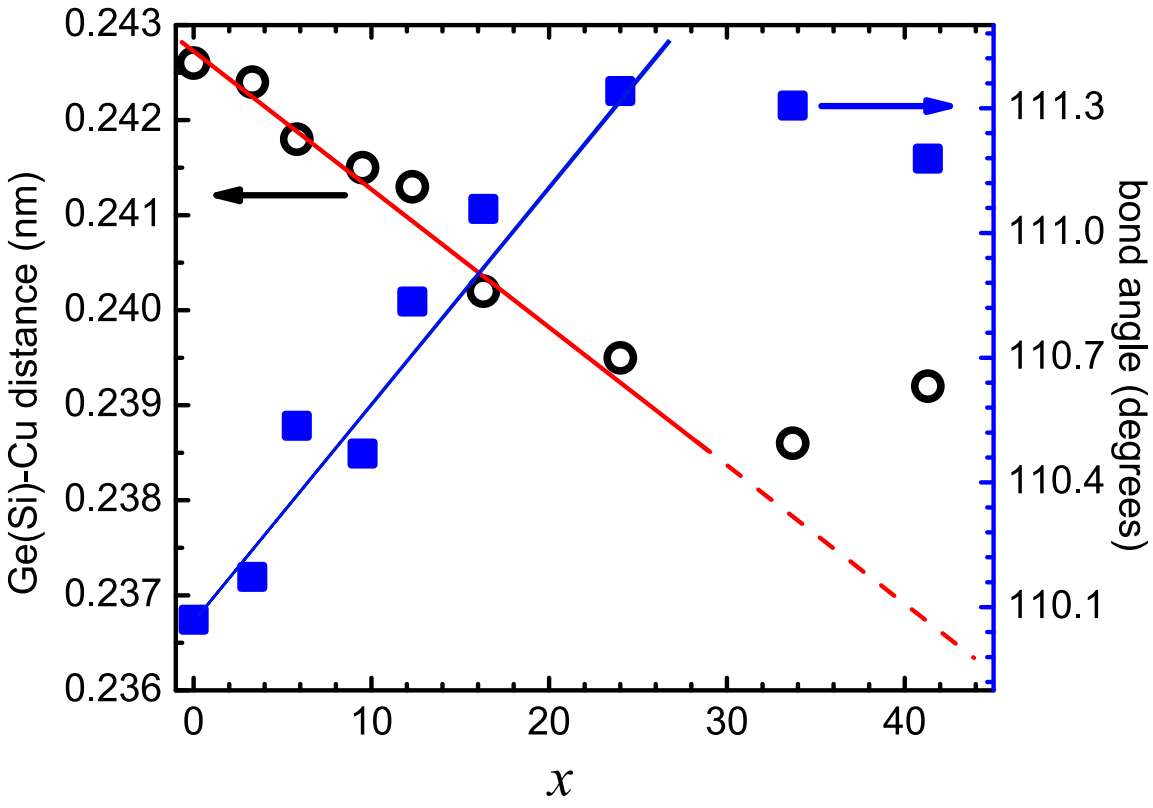

Figure 4.11: Cu-nearest neighbor distance (open circles) and bond angle (solid squares). Angles are the larger of two values as explained in the text. Values from Ref. [35]. The dashed and solid lines are guides to the eyes. Reproduced from Ref. [103].

4.3.1 Sample Preparation

Several samples of Ba-Co-Ge clathrates were prepared from pure elements [Ge (pieces, 5N), Co (ingot, 4N), and Ba (rod, 2N5)] with excess (4%) barium to compensate for evaporation, and arc melted in an argon environment followed by annealing in a BN crucible in an evacuated sealed quartz tube for one week. Three of these polycrystalline ingots were selected for further study as described below. The type-I sample was annealed at 800 °C followed by quenching in water and the chiral samples were annealed at 750 °C and slowly cooled to room temperature. Powder X-ray diffraction (XRD) measurements and Rietveld refinement along with wavelength dispersive spectroscopy (WDS) measurements were performed on the samples. Resistivity, Hall coefficient, Seebeck coefficient, heat capacity, and thermal conductivity measurements were conducted in a Quantum Design Physical Property Measurement System. A Quantum Design SQUID magnetometer was used to measure magnetic properties. Note that although for some of the other materials described in this thesis, sample preparations were done by collaborators, in this case I did all sample preparations and analysis as well as characterization measurements, except that I did not run the shared instruments used to collect the magnetization and heat capacity data.

4.3.2 Transport, Magnetic Measurements, and Discussion

Powder XRD measurements on the nominal $Ba_8Co_3Ge_{43}$ sample showed the material to have the type-I clathrate structure (space group $Pm\bar{3}n$, with Ba in cage-centered positions). Nominal $Ba_6Co_2Ge_{23}$ and $Ba_6Co_5Ge_{20}$ samples were shown to have the chiral structure (space group $P4_132$) with small extra phases, $CoGe_2$ and Ge. Figure 4.12 shows the XRD results and fits for the $Ba_8Co_3Ge_{43}$ and $Ba_6Co_5Ge_{20}$ samples. See Table 4.5 for lattice constants from the XRD refinements.

The detailed compositions of all samples from WDS are given in Table 4.5. The com-

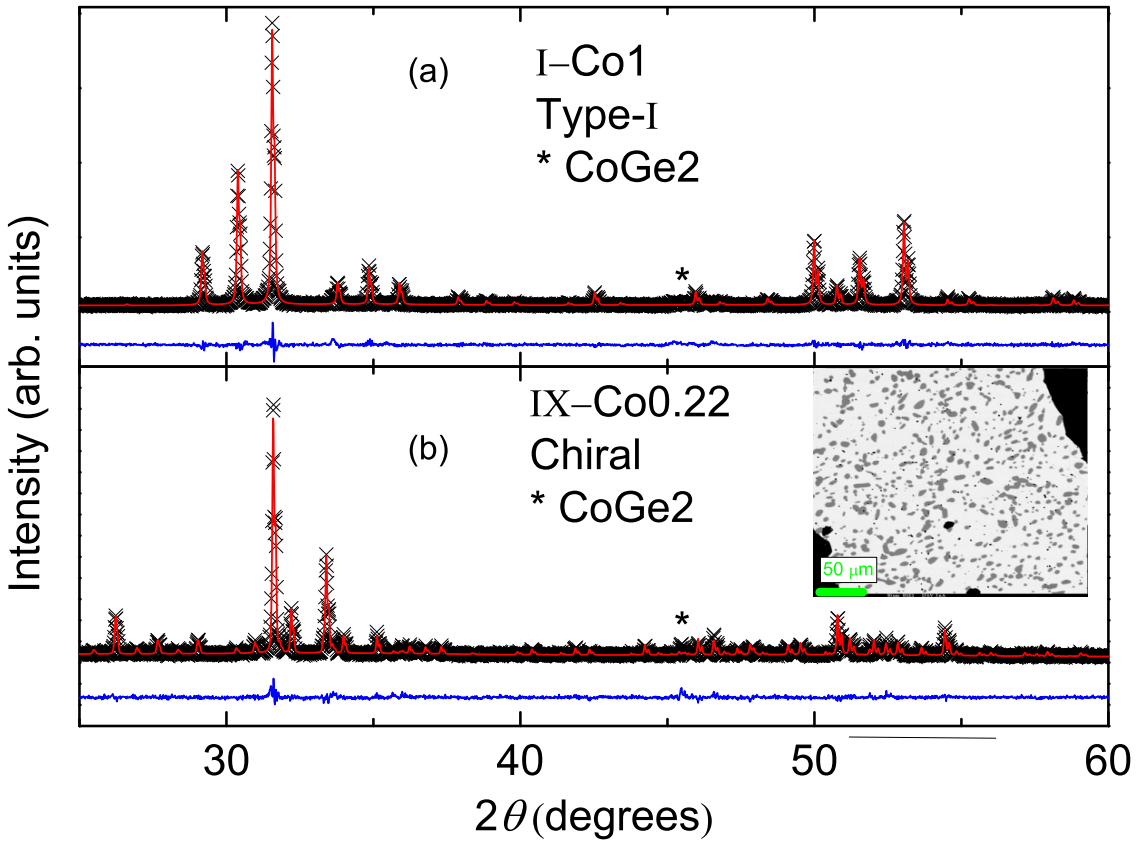

Figure 4.12: X-ray data with Rietveld refinement profile (red lines) and the difference (blue lines) for a) $Ba_8Co_3Ge_{43}$ (sample I-Co1) b) $Ba_6Co_5Ge_{20}$ (sample IX-Co0.22), showing also a back-scattered electron image. Reprinted with permission from [141].

Table 4.5: Sample compositions and lattice constants extracted from WDS and powder XRD, respectively, with carrier densities (n) from Hall measurements (with minus sign denoting n-type). Reprinted with permission from [141].

nominal	Ba	Co	Ge	a (nm)	n (cm^{-3})
$Ba_8Co_3Ge_{43}$ (I-Co1)	8.00	0.96	42.41	1.0671	-4×10^{21}
$Ba_6Co_5Ge_{20}$ (IX-Co0.22)	5.94	0.22	24.77	1.4144	-8×10^{21}
$Ba_6Co_2Ge_{23}$ (IX-Co0.27)	6.00	0.27	24.71	1.4542	4×10^{21}

position of the type-I sample is $Ba_8Co_1Ge_{42.5}$. This composition has a vacancy concentration of 2.6 per cell, slightly reduced from that of unsubstituted $Ba_8Ge_{43}\square_3$, which has a superstructure with space group $Ia\bar{3}d$, however, we did not observe superstructure peaks for the substituted material. The $Ba_6Co_{0.27}Ge_{24.71}$ and $Ba_{5.94}Co_{0.22}Ge_{24.77}$ chiral clathrates have no framework vacancies according to the WDS measurements. We denoted the type-I sample as I-Co1, and the chiral (type-IX) samples as IX-Co0.27 and IX-Co0.22. The lattice constants of IX-Co0.22 and IX-Co0.27, also in Table 4.5, are slightly reduced from the reported value [142] $a = 1.45564(2)$ nm for Ba_6Ge_{25}. On the other hand, the I-Co1 lattice constant is slightly larger (when doubled) than of the [143] type-I $Ba_8Ge_{43}\square_3$ which has a $2 \times 2 \times 2$ supercell with $a = 2.1307(1)$ nm. These results are consistent with those of Ref. [144], and also in line with results for type-I Ba-Ge clathrate substitution by Cu and Ni [145, 35, 146], which also induce an expansion of the lattice.

Note that the amount of Co substituted in the type-I sample is smaller than the maximum reported in reference [144], where it was found that the solubility of Co in the type-I and chiral structures can be up to 2.5 and 1 per unit cell, respectively. The samples measured here came from a number of trial syntheses, and these compositions were the largest Co concentrations yielding continuous clathrate phases allowing transport measurements to be performed. While in Cu type-I clathrates the Zintl condition is found to strongly stabilize the composition [145, 35, 147], Ni clathrates allow more variation in composition [146, 147], an apparent indication that the stabilization is lessened. For Co substitution (with Zintl condition corresponding to 2.5 per cell for type I) this trend of apparently lower stability for the Zintl composition continues and competes with $CoGe_2$ phase formation [144]. Here, a portion of the Co remained in the ingots as $CoGe_2$; for example for the Co0.22 sample which had the largest initial Co concentration, a back-scattered electron image is shown in Figure 4.12. In other samples the second phase is correspondingly reduced (see star positions in the XRD spectra, Figure 4.12). With further increased

substitution, approaching the Zintl compositions, the clathrate phases were found to be nonuniform and unsuitable for measurements of physical properties.

The Hall coefficient R_H was obtained by measuring the Hall resistivity (ρ_H) versus field ($\rho_H = R_H B$). Assuming a one-band model, the carrier density, n, was determined according to $n = 1/(R_H e)$. Results are given in Table 4.5. The type-I carrier density is affected by vacancies, formed spontaneously in many clathrates [39, 148] for electron balance. This follows the Zintl condition, promoting a 4-bonded framework as noted earlier. In the observed I-Co1 composition, eight Ba^{2+} ions can be considered to donate a total of 16 electrons per formula unit, each Co requires 5 electrons to satisfy 4 framework bonds (with d-shells filled, consistent with the diamagnetic behavior described below), and 4 electrons per vacancy are needed to fill dangling bonds. The observed I-Co1 composition (Table 4.5) includes 2.6 vacancies per cell, so 15.3 electrons per formula unit are needed to complete the sp^3 framework, leaving 0.7 electrons to go into the conduction band. However, the Hall results correspond to a larger apparent concentration of about 4.8 electrons per cell. This is similar to results for $Ba_8Ni_xGe_{46-y}$ [146], in which for small x samples multiple vacancies per cell were observed to form, implying small expected carrier densities, yet Hall measurements indicated very large carrier density comparable to what is observed here. It appears that the Fermi-level electronic structure in the present case, as well as for low-Ni substitution, is characterized by multiple band crossings, as evidenced originally in [149] Ba_8Ge_{43}, and although multiple vacancies are formed this does not serve to reduce significantly the carrier density as might be expected.

With no vacancies in the chiral samples according to the measured compositions, a similar calculation based on framework bonding [150] yields about 12 electrons per cell above the Zintl condition for both cases, a strongly metallic situation as expected for such materials. The large observed Hall carrier densities are therefore not surprising, however similar to the above result, a multi-band condition at the Fermi energy is also expected

for these materials, so that the Hall carrier densities do not necessarily reflect the number of carriers above the Zintl condition. Indeed, calculations have shown [151] an electronic density of states for Ba_6Ge_{25} characterized by a number of sharp peaks in the vicinity of the Fermi energy, a condition which may explain the observed n and p type behavior associated with small changes in composition.

Figure 4.13 shows resistivities from 2 K to room temperature. For type-I the magnitude and behavior is similar to that of Ba_8Ge_{43} [149] and low-x $Ba_8Ni_xGe_{46-y}$ [146], reinforcing the similar electronic behavior of these materials as noted above. The resistivities of the chiral samples are generally metallic-like, however they increase with deceasing temperature below 120 K, due to the low temperature phase transition. There is also a small slope change near 220 K corresponding to the second phase transition (compared to 215 K in unsubstituted Ba_6Ge_{25}), seen more distinctly in other properties as described below. Sample IX-Co0.22 with lower Co concentration shows the trend more clearly. Since the resistivities show thermal hysteresis below 120 K, these must correspond to first-order phase transitions. This low-temperature anomaly is suppressed to lower temperatures compared to the transition observed [142] near 180 K in Ba_6Ge_{25}, while the other transition occurs at about the same temperature but with a much smaller effect on transport properties. Qualitatively, this is similar to the effect of Eu substitution [142] for Ba in Ba_6Ge_{25}, although Co substituents are nonmagnetic, and substitute on the framework rather than in guest sites.

The lattice thermal conductivities (κ_L) and Seebeck coefficients (S) of the I-Co1 and IX-Co0.27 samples are shown in Figure 4.14. For κ_L we subtracted the electronic contribution from the measured values using the Wiedemann-Franz law. κ_L of I-Co1 shows a crystal-like peak and reaches 1.7 W/(K-m) at room temperature. Thus with Co substitution the phonon mobility for this sample remains high, although reduced from that of Ba_8Ge_{43} [143]. While vacancy scattering will affect the thermal conductivity, it was recently indicated that the order or disorder of the vacancies may make surprisingly little difference

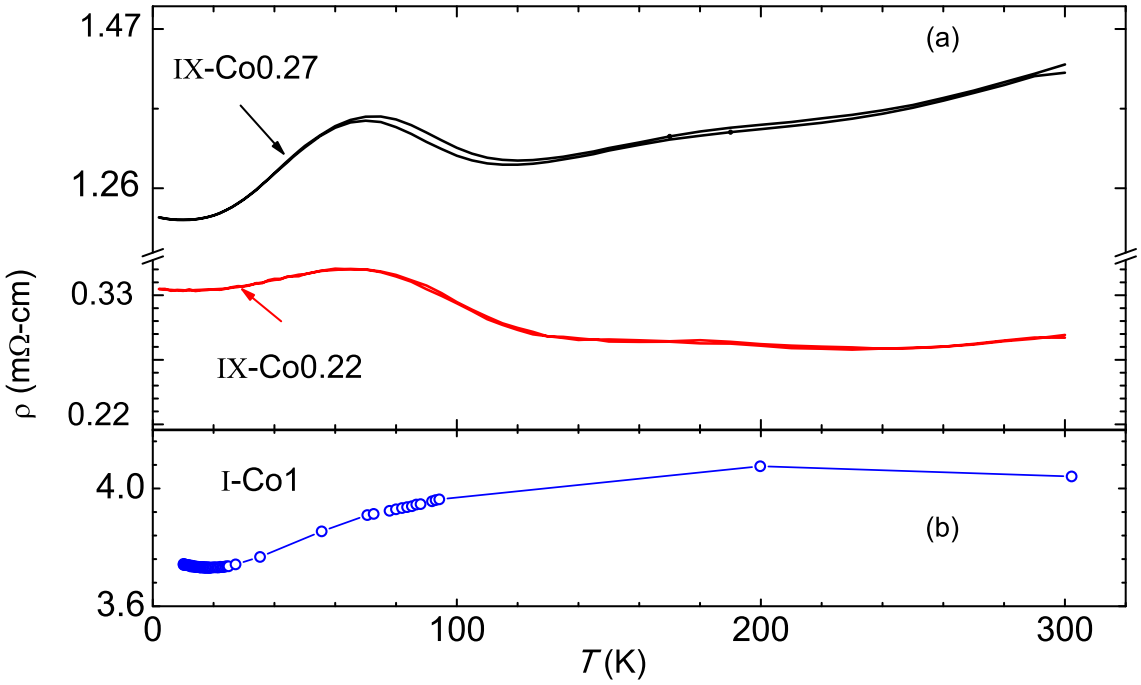

Figure 4.13: Resistivities of Ba-Co-Ge clathrates as a function of temperature a) IX-Co0.27 and IX-Co0.22 measured both for heating and cooling b) I-Co1. Reprinted with permission from [141].

[152]. However note that the thermal conductivity is larger than that of $Ba_8Ga_{16}Ge_{30}$ presumably due to reduced alloy scattering [29].

The IX-Co0.27 sample does not exhibit a crystalline-type peak in thermal conductivity, and the magnitude of κ_L , reaching 1.48 W/K-m at room temperature, qualifies as glass-like behavior. Slope changes are also seen in its κ_L at the temperatures of both phase transitions. The Seebeck coefficient for IX-Co0.27 is negative in spite of it being p-type at room temperature, presumably due to multiband behavior as noted above. Its magnitude, $S = -20$ μV/K at room temperature, is relatively small consistent with the metallic behavior.

A notable feature of the Seebeck coefficient of IX-Co0.27 is the changes in slope at about 90 K and 230 K, consistent with the transitions seen in resistivity. This is shown by the straight lines in Figure 4.14(b). The fitted slopes change from -0.076 μV/K^2 at low temperatures to -0.056 μV/K^2 between 120 and 220 K, and -0.113 μV/K^2 above 240 K.

The heat capacity of IX-Co0.27 vs temperature is shown in Figure 4.15. The electronic contribution, γ, was determined by fitting the low temperature data to a straight line according to $C_p/T = \gamma + \beta T^2$. Results are $\gamma = 23$ mJ/mol K^2 for IX-Co0.27, and 29 mJ/mol K^2 for IX-Co0.22, where mole values refer to the Ba_6X_{25} formula unit, while a similar measurement for I-Co1 yields $\gamma = 42$ mJ/mol K^2 (per mole Ba_8X_{46})

To model the results, we fitted the chiral data using Debye and Einstein models. Since the low-temperature phase transition is suppressed to near 100 K by Co substitution, this fit runs through the transformations, and thus provides only a qualitative measure of the localized oscillator behavior, however the difference curve based on this fitted curve allows the effects of transformations on the specific heat to be seen more clearly. We considered two Einstein terms (C_E) with parameters Θ_{E1} and Θ_{E2}, one Debye term (C_D) with parameter Θ_D, plus the electronic term $C_{el} = \gamma T$, with γ from the low-temperature fit. These

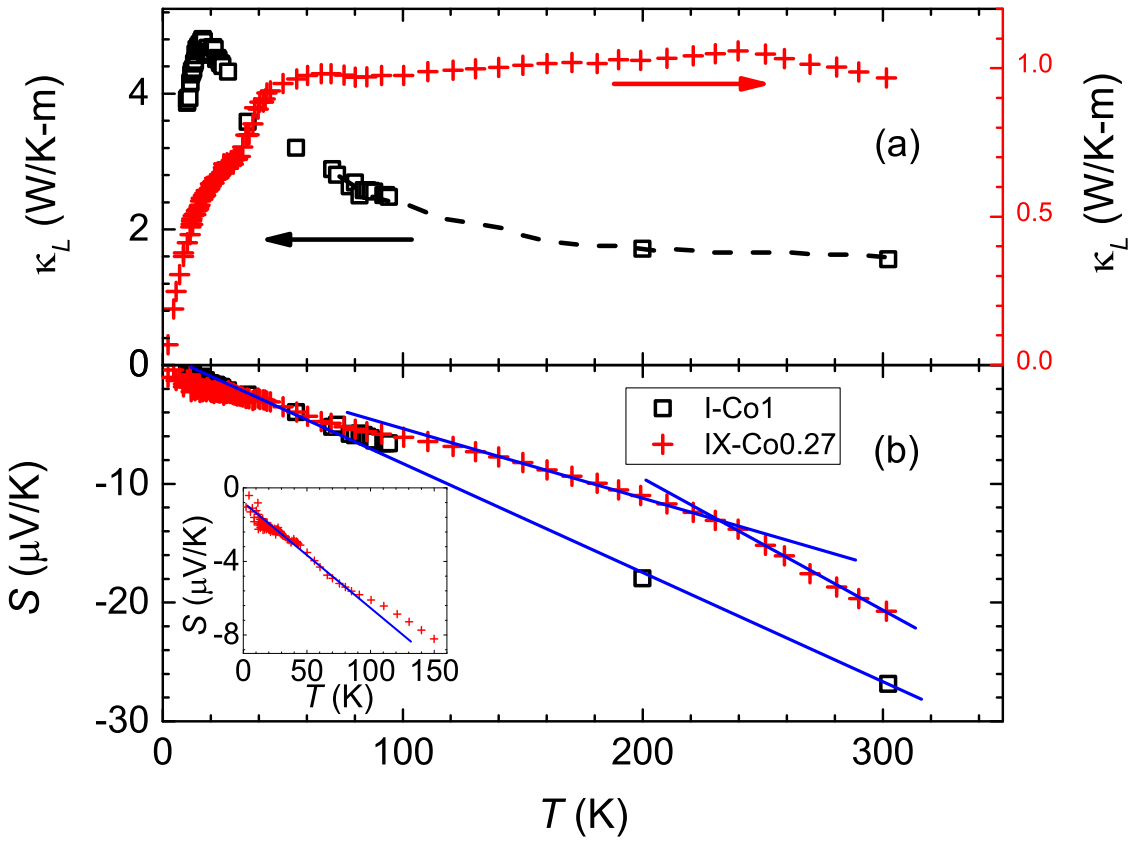

Figure 4.14: (a) Thermal conductivity and (b) Seebeck coefficient vs temperature for I-Co1 (open squares) and IX-Co0.27 (open circles). Inset shows Seebeck coefficient below 160 K for IX-Co0.27 sample. Solid lines are fitted straight lines. Reprinted with permission from [141].

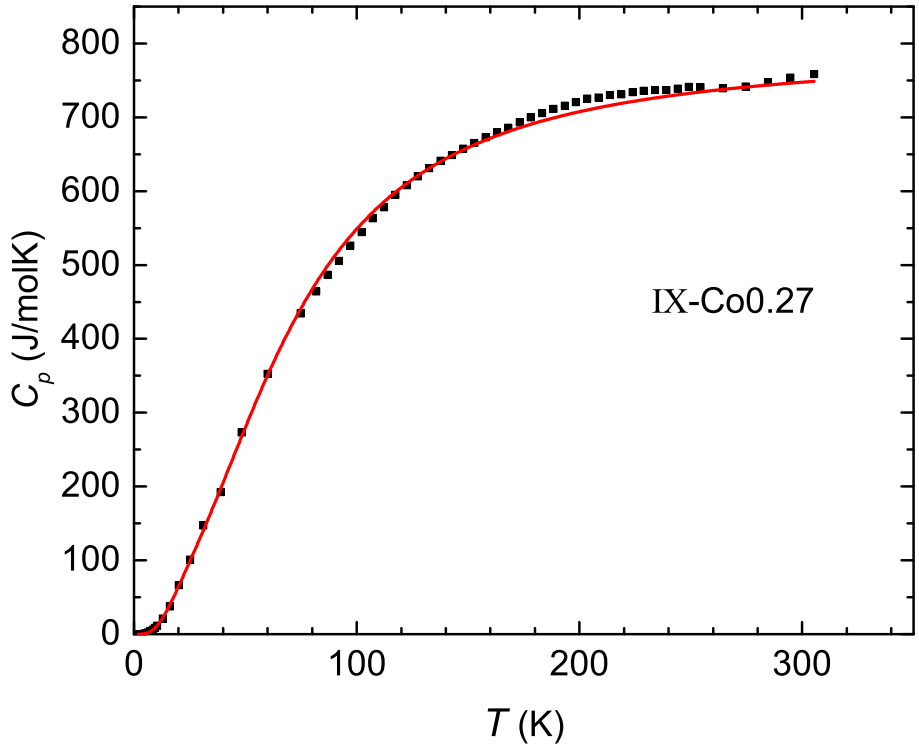

Figure 4.15: Heat capacity (C_P) for sample IX-Co0.27. Solid curve fit to the model described in text. Data are normalized per mole formula unit of Ba_6X_{25}. Reprinted with permission from [141].

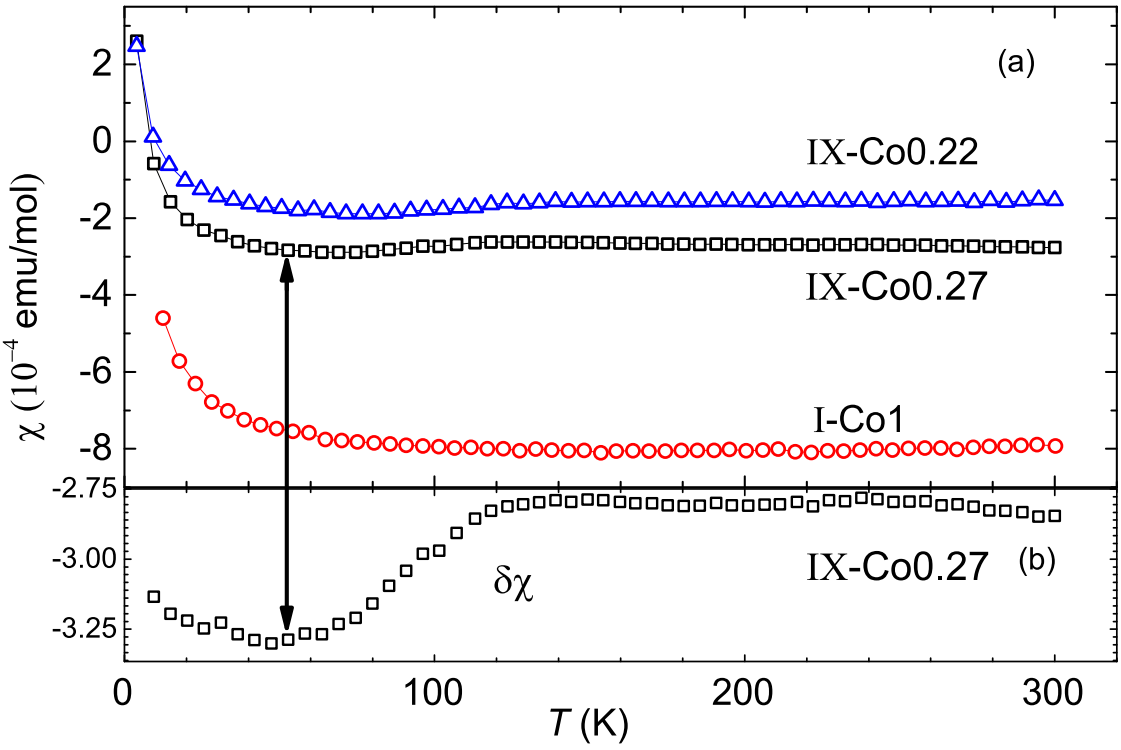

Figure 4.16: Temperature dependence of magnetic susceptibility of (a) IX-Co0.27 (squares), IX-Co0.22 (triangles) and I-Co1(open circles). (b) IX-Co0.27 results after removing small Curie paramagnetism as explained in the text. Values per mole formula unit (Ba_6X_{25}, or Ba_8X_{46}). Reprinted with permission from [141].

Table 4.6: Heat capacity fitting parameters. Reprinted with permission from [141].

sample	Θ_D (K)	Θ_{E1} (K)	Θ_{E2} (K)	γ (mJ/mol K^2)
IX-Co0.27	308	84	43	23
IX-Co0.22	301	80	60	29

are:

$$C_E = 3N_E R \left(\frac{\Theta_E}{T}\right)^2 \frac{e^{\Theta_E/T}}{(e^{\Theta_E/T}-1)^2}, \tag{4.7a}$$

$$C_D = 9N_D R(\frac{T}{\Theta_D})^3 \int_0^{\Theta_D/T} \frac{x^4 e^x dx}{(e^x-1)^2}, \tag{4.7b}$$

where N_D and N_E are the number of oscillators per formula unit, which should correspond to the number of framework atoms and guest atoms, respectively.

Table 4.6 shows the parameters from least squares fitting. For the chiral structures we used $N_D = 25$, $N_{E1} = 5$, and $N_{E2} = 1$. Although we have three Ba sites, this corresponds to combining two guest sites to make N_{E1}. The fitted curve [Figure 4.15] deviates slightly as expected in the region of the low-temperature transition near 100 K, while the high-temperature transition is more obvious in the results.

Figure 4.16(a) shows the magnetic susceptibilities measured at 5000 Oe. All samples exhibit diamagnetism, a normal case for most intermetallic clathrates. I-Co1 has $\chi = -7.9 \times 10^{-4}$ (emu/mol) at room temperature, compared to the calculated core diamagnetism,-5.2×10^{-4} (emu/mol) [153]. In all cases the small Curie-like low-temperature upturn corresponds to very dilute moments, rather than intrinsic magnetism. This was confirmed by $M - H$ measurements at low temperatures; for example in sample IX-Co0.27 the $M - H$ results (not shown) could be fitted almost entirely due to isolated moments with effective paramagnetic moment 6.1 μ_B and concentration $5{\times}10^{-4}$ per for-

mula unit. Subtracting this fitted contribution, we obtain the net result ($\delta\chi$) shown in Figure 4.16(b), where the effects of the two transitions can be seen more clearly as small slope changes in χ. Therefore, the large diamagnetism is suggested to be due to structural diamagnetism of the clathrates [142].

Assuming that the electron-phonon enhancement is small, the electronic heat capacity term is [23], $\gamma = (k_B\pi)^2 g(E_F)/3$. Based on this relation and the results quoted above for γ, we obtain the low-temperature densities of states $g(E_F) = 12.3$ and 9.9 states/(eV-mole Ba_6X_{25}) for IX-Co0.22 and IX-Co0.27, respectively. These are similar to results for the low-temperature Ba_6Ge_{25} phase from DFT calculations [154], though a factor of about 4 larger than an experimental estimate for Ba_6Ge_{25} obtained by other means [155].

From $g(E_F)$ we also obtain the low temperature Pauli contribution to the susceptibility using $\chi_{\rm Pauli} = \mu_B^2 g(E_F)$, giving $\chi_{\rm Pauli} = 4.0\times10^{-4}$ and 3.2×10^{-4} emu/(mole Ba_6X_{25}) for IX-Co0.22 and IX-Co0.27 respectively. The difference in calculated values is comparable to the observed difference between the two samples, $\Delta\chi \approx 1.2\times10^{-4}$ emu/(mole Ba_6X_{25}), nearly independent of temperature, as shown in Figure 4.16.

We thus assume that the diamagnetic background term ($\chi_{\rm dia}$) is the same for both chiral compositions, with the observed temperature dependences due to changes in $\chi_{\rm Pauli}$. (We assume the Landau term also to be temperature independent; a similar assumption was made in Ref. [155].) Starting with the low temperature baseline susceptibility for IX-Co0.27 (Figure 4.16(b)) and extrapolating to $\chi_{\rm Pauli} = 0$ we obtain $\chi_{\rm dia} = -6.4 \times 10^{-4}$ emu/(mole Ba_6X_{25}), comparable to the value -8×10^{-4} emu/mole extracted in Ref. [155] for unsubstituted Ba_6X_{25}.

The small observed changes in χ at the phase transformations in the chiral samples indicate that $g(E_F)$ does not change substantially at the phase transitions. This is in contrast to results [156, 155] for unsubstituted Ba_6Ge_{25}. The changes in χ can be seen most clearly in the difference curve for IX-Co0.27, Figure 4.16(b): the low-temperature transition is

accompanied by a change $\Delta\chi \approx -5 \times 10^{-5}$ (emu/mole Ba_6X_{25}), or about 10% of the low-temperature $\chi_{\rm Pauli}$ value. This corresponds to a 10% change in $g(E_F)$, in contrast with the factor of 4 reduction estimated [156, 155] for Ba_6Ge_{25}. This small change is in line with the much smaller effect observed in resistivity. Thus this transformation is reduced in temperature in the Co-substituted material, and is also accompanied by a greatly reduced effect on the electronic density of states.

The loss of carriers in the structural distortion in Ba_6Ge_{25} has been connected through crystallography to breaking of bonds [157], and thus the results seen here are presumably due to a reduced-magnitude displacement of Ba ions associated with the substituted framework. Similar effects may accompany Eu substitution [142], which as we noted produces quite similar changes in the observed transport behavior. Indeed, the observed resistivity behavior and also the reduction in as well as broadening of the low temperature phase transformation observed here is quite similar to the results displayed [142] for a $Eu_{0.8}$ substituted sample, results which were explained as consistent with a chemical pressure effect due to the decreased lattice constant, as also observed for Co substitution.

Per framework atom, the measured γ for I-Co1 is quite close to that of the chiral-materials, which reinforces its strongly metallic behavior of this composition as also evidenced by the transport results. As noted above, comparing the similar transport results for Ba_8Ge_{43} indicates that the Co-substituted composition presumably also exhibits complicated bands cutting E_F leading to multiple carrier types. The observed γ can also be used to estimate the Pauli susceptibility of the type-I composition. Using the relationships described above yields $\chi_{\rm Pauli} = 5.8 \times 10^{-4}$ (emu/mol Ba_8X_{46}) for I-Co1. Subtracting this from the measured result we obtain a bare diamagnetic contribution of $\chi_{\rm dia} = -14 \times 10^{-4}$ emu/(mole Ba_8X_{46}), more diamagnetic by about -9×10^{-4} emu/(mole Ba_8X_{46}) than the calculated core diamagnetism. The origin for this large contribution remains unclear, although sometimes this contribution is attributed to a ring current in the clathrate frame-

work. Note also that per framework atom, the results for the two structures are similar: we find that with $\chi_{\rm Pauli}$ removed, $\chi_{\rm dia} = -2.6 \times 10^{-5}$ emu/(mole-X-atom) for both chiral compositions and $\chi_{\rm dia} = -3.1 \times 10^{-5}$ emu/(mole-X-atom) for the type-I. Results quoted [155] above for Ba_6Ge_{25} correspond to the similar value, $\chi_{\rm dia} = -3.1 \times 10^{-5}$ emu/(mole-X-atom). Thus it is may be that a ring current or related electronic feature per framework atom underlies this behavior.

4.4 Cu_2Se

Long known as a superionic conductor, Cu_2Se has also attracted significant recent interest as an electronic material for several potential applications. As described in the introduction, one reason has been the observation of large thermoelectric figure of merit, and the resulting possibilities for thermoelectric applications based on Cu_2Se and related alloys. Additional interest has been based on its potential use as an active material for photoelectric devices [158]. Here, I measured Cu NMR in Cu_2Se to address the structural changes and Cu-ion dynamics. In Cu_2Se the rapid ion motion at high temperatures is manifested through strongly narrowed NMR line shapes, while at lower temperatures, we show that the hopping motion persists down to the structure change at 100 K, below which there are large local variations in electronic behavior indicative of impurity band behavior. A report of this work was already published and these results are reprinted with permission from [140].

4.4.1 Sample Preparation

Samples for the measurements were from the same preparation batch as described in Ref. [52], with synthesis using a combination of melting and annealing followed by spark plasma sintering for compaction. As reported in this reference, the structure was investigated with powder X-ray diffraction (XRD), and the homogeneity and composition was investigated by electron microprobe measurements including wavelength dispersive spec-

troscopy (WDS). WDS measurements were carried out using a Cameca SX50 equipped with four spectrometers by Dr. Ballikaya. The resulting images showed the samples to be uniform in composition, with no detectable second phases. The previously reported Hall measurements [52] correspond to a hole concentration of $5.16 \times 10^{20}\,\mathrm{cm}^{-3}$ at 300 K, with small changes observed vs. temperature including a shallow minimum of $4.8 \times 10^{20}\,\mathrm{cm}^{-3}$ near 120 K, and an increase to $5.0 \times 10^{20}\,\mathrm{cm}^{-3}$ below that. Assuming each hole is associated with one Cu vacancy, the 300 K value corresponds to a composition of $Cu_{1.974}Se$ where the volume (2414 $\mathrm{\AA}^3$) and $Z = 48$ were used as reported in ref. [62] to calculate the density. From WDS measurements, the mean composition obtained from probing 12 different positions was $Cu_{1.95}Se$, which is consistent with the composition estimated from Hall measurements within the 1-2% accuracy of the WDS analysis.

Powder XRD was performed both at room temperature and at 473 K with Cu Kα radiation, as described previously [52]. These temperatures encompass the $\alpha - \beta$ phase transition [49, 50, 159], which occurs near 390 K in $Cu_{2-x}Se$ for $x \simeq 0$, decreasing somewhat vs x. Here we used Rietveld refinements (obtained using GSAS software [96, 95]) to further characterize the structures. For the β phase we fitted using site occupations of the cubic $Fm - 3m$ structure reported in Ref. [62], yielding a lattice constant a = 0.58278 nm. A fit of the room temperature spectrum to the reported monoclinic α phase structure is shown in the inset plot of Figure 4.17; the structure with 144 atoms/unit cell, space group C2/c, as in Ref. [62], yielded good agreement. However, the XRD is not definitive; and there is still no general agreement on the structure. This refinement yielded a = 0.71392 nm, b = 1.23823 nm, c = 2.73772 nm, and β = 94.3°.

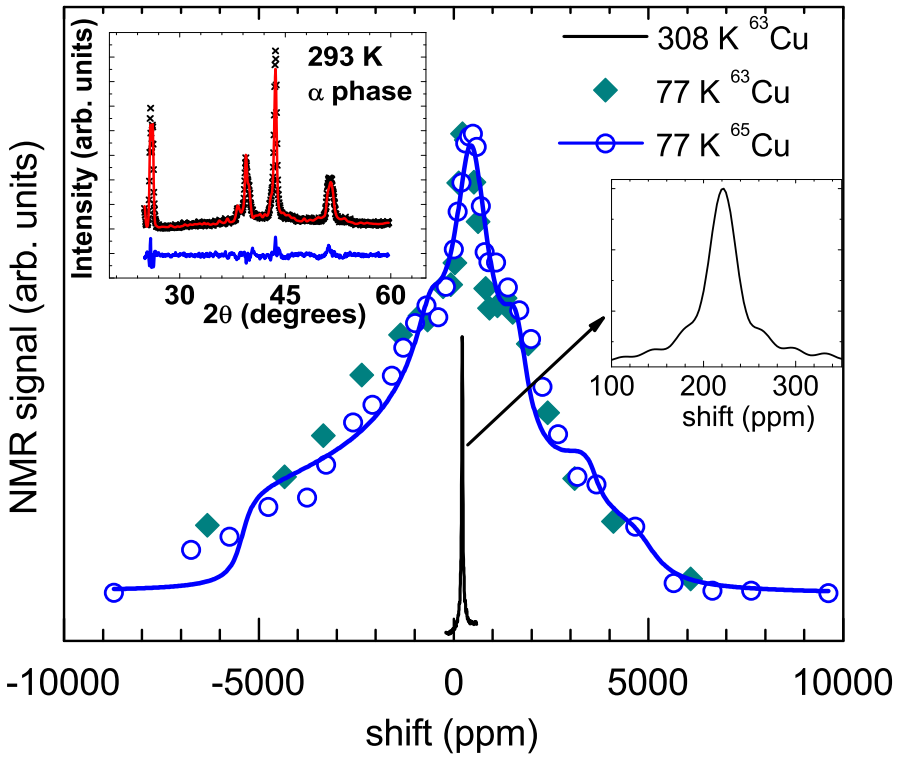

Figure 4.17: ^{63}Cu and ^{65}Cu NMR spectra at T = 77 K (symbols), with fitted ^{65}Cu spectrum (solid curve). Motionally-narrowed 308 K spectrum also shown for comparison (sharp feature with expanded view at right). Left inset: powder XRD spectrum at ambient temperature (α phase), along with results from refinement and difference plot. Reprinted with permission from [140]. Copyright (2015) American Chemical Society.

4.4.2 Results and Analysis

4.4.2.1 NMR Spectra

Figure 4.17 shows static ^{63}Cu and ^{65}Cu NMR spectra measured at 77 K. Also shown for comparison is the line observed near room temperature (expanded at right), motionally narrowed by hopping of Cu ions. The motionally narrowed Cu NMR line has been a subject of previous investigation [160, 161] at higher temperatures in the superionic β phase. In our study, free-induction decays were used to measure the motionally narrowed lines down to about 260 K, below which the signals measured this way disappeared due to the slowing of ionic motions. However, standard spin-echo methods could be used to observe the static NMR line shapes below T = 150 K, giving the static spectra such as shown in Figure 4.17. The low-temperature line width is due to a combination of magnetic and quadrupole shifts, the latter due to interactions with static electric field gradients (EFGs). The spectra represent m = 1/2 to $-1/2$ transitions for the I = 3/2 Cu nuclei, and thus the shifts ($\Delta\nu/\nu_o$, relative to the reference frequency ν_o) include large second-order electric quadrupole contributions.

To identify parts of the line shape associated with different Cu sites, we measured spin-lattice relaxation times (T_1) at 77 K at several positions on the line. Results are shown in Figure 4.18 along with the modeled line shape described below. The relatively narrow peak near the center exhibits a shorter T_1 (= 303 ms) than its immediate surroundings, so we fitted this peak using one set of NMR parameters (labeled “site A"). For smaller shifts down to -5000 ppm, based on the nearly identical T_1 values we used a second set of parameters (“site B") with larger quadrupole broadening to fit the intensity covering this range. The combination of two sites according to this model provided a reasonable accounting for the 77 K line shape, but with a deficit in intensity at large positive shift. A third site with large magnetic shift was thus added to the fit in the region of the shoulder

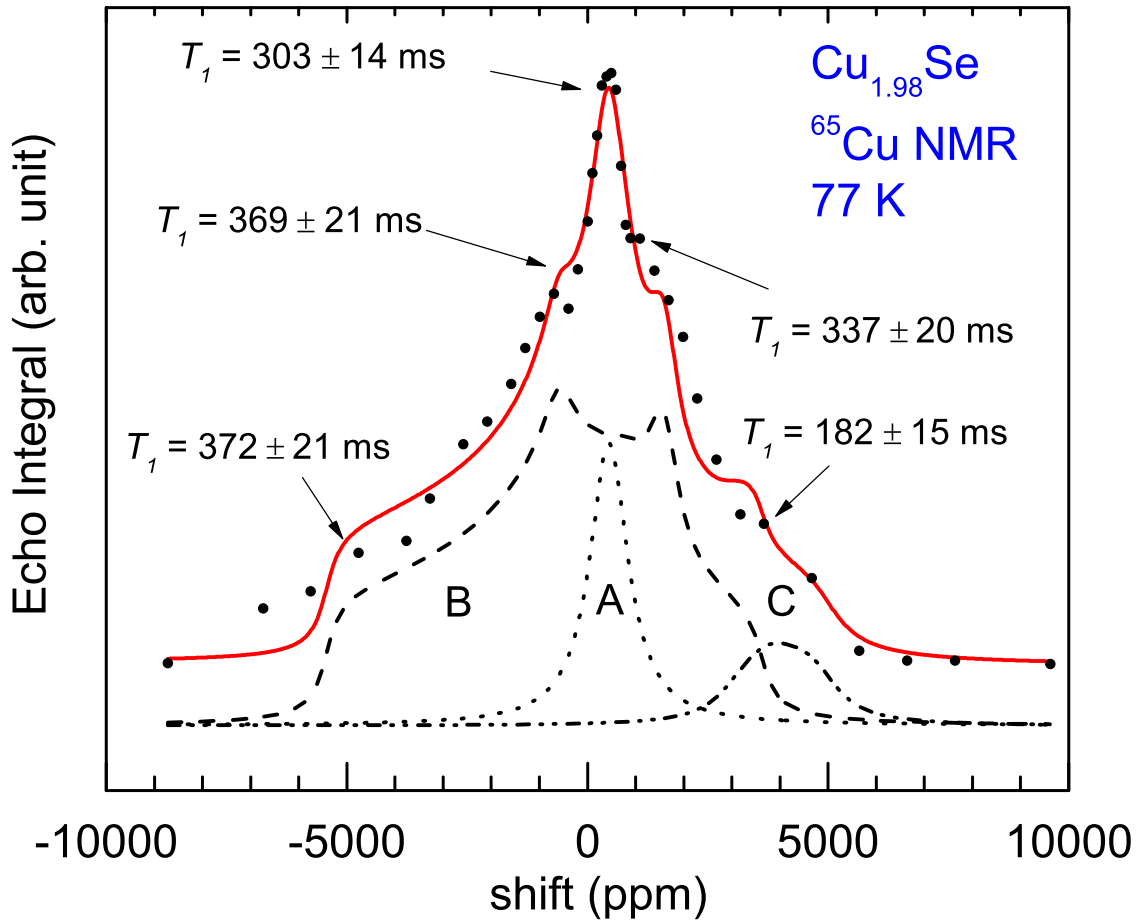

Figure 4.18: ^{65}Cu spin-echo line shape measured at 77 K, fitted to superposition of 3 powder patterns, labeled A, B, C. Fitted spectrum (solid curve) and data (symbols) displaced upward for clarity. Also indicated: $^{65}T_1$ values measured at 77 K at locations shown. Reprinted with permission from [140]. Copyright (2015) American Chemical Society.

near +4000 ppm, where a significantly smaller T_1 was also observed.

From least-squares minimization starting with these assignments, we obtained the solid curve in Figure 4.18, where spectra for the three individual fitted sites are also shown as separate curves. In the fitting results site B has 76% of the spectral weight, EFG parameters ν_Q = 11.2 MHz and η = 0.67, and isotropic shift δ_{iso} = +588 ppm. Site A (16% of spectral weight), fitted with ν_Q set to zero, has δ_{iso} = +446 ppm, while site C (8% of spectral

weight) has δ_{iso} = +4300 ppm. Note that sites A and B include EFGs similar to those of Cu_2S, which has 2 sites [162] exhibiting ν_Q = 14.9 MHz and 1.9 MHz.

Site C has a larger magnetic shift (δ_{iso}) than the others, in the range of conduction-electron mediated Knight shifts in metals. We assign this feature to Cu sites adjoining positions of Cu vacancies, with the enhanced paramagnetic shift attributed to an enhanced density of holes on an acceptor state surrounding the vacancy. Note that the composition $Cu_{1.974}Se$ obtained by associating the measured hole density to Cu vacancies as described above corresponds to a mean density of 0.013 vacancies per Cu site in the Cu_2Se cubic phase. Also in the recently described low-temperature structure of Ref. [56] the two Cu sites have a mean Cu-Cu coordination number of 7, hence for this composition 9% of Cu sites would have a vacancy within the 1st neighbor shell. (In the ambient-temperature α structure of Ref. [62] the Cu-Cu second-neighbor shell has mean coordination number 5.8 giving 7.5% of Cu sites adjacent to a vacancy.) Compared to the fitted 8% spectral weight for site C, this assignment seems reasonable.

Further information is obtained by partitioning the T_1 into contributions due to electric quadrupole (Q) and magnetic (M) mechanisms. For this, we performed measurements at 77 K both for ^{63}Cu and ^{65}Cu (denoted $^{63}T_1$ and for $^{65}T_1$, respectively) at the positions shown in Figure 4.18. The contributions $(T_1)^{-1} = (T_{1Q})^{-1} + (T_{1M})^{-1}$ can be separated [47] since $(T_{1Q})^{-1} \propto Q^2$ and $(T_{1M})^{-1} \propto \gamma^2$. Results are shown in Table 4.7. For +3400 ppm, the single-T_1 fit was improved significantly by using a superposition of sites with two sets of T_1 values, consistent with the overlap of sites at this point in the line shape model. One of the corresponding $(T_1)^{-1}$ sets, labeled +3400(C) in Table 4.7, was assigned to site C because its large magnetic contribution matches the large paramagnetic shift for this site. The other set [labeled +3400(B)], has $(T_1)^{-1}$ values matching those of the other site B positions. On the other hand, at the resonance maximum, dominated by site A, a distinct set of $(T_1)^{-1}$ values is observed, with a mechanism almost entirely attributable to

Table 4.7: Partitioned magnetic (M) and electric quadrupole (Q) ^{63}Cu spin-lattice relaxation rate contributions at T = 77 K, measured for positions on NMR line specified, along with identification according to 3 fitted sites as decribed in text. Reprinted with permission from [140]. Copyright (2015) American Chemical Society.

	position (ppm)	$^{63}T_{1M}^{-1}(\mathrm{s}^{-1})$	$^{63}T_{1Q}^{-1}(\mathrm{s}^{-1})$
Site A	+507	0.6±0.6	3.3±1.0
Site B	−5000	1.5±0.6	1.1±0.7
	−920	2.0±0.6	0.6±0.6
	+1180	1.7±0.8	1.1±1.0
	+3400(B)	1.44±0.01	1.09±0.01
Site C	+3400(C)	13.7±0.1	0

a quadrupole mechanism. These results help to validate the model for partitioning among sites in the 77 K spectrum.

4.4.2.2 Phase Transitions and Motional Narrowing

Figure 4.19 shows a set of motionally narrowed ^{63}Cu spectra obtained at higher temperatures. The vertical line shows the δ_{iso} = 220 ppm line position for the α phase, a shift which is purely magnetic in origin due to motional averaging of the quadrupole contribution. The single narrowed line indicates that mobile Cu ions sample all Cu sites in the complex structure at these temperatures. As can be seen, there is a small increase in line position near the $\alpha - \beta$ transition temperature. This is seen more clearly in Figure 4.20 where extracted δ_{iso} values are plotted vs temperature along with the corresponding line widths (lower plot of same graph). Note for comparison, δ_{iso} was previously reported [139] for Cu_2Se at a temperature of 860 K, as a slightly increased value of 290 ppm, using the NMR shift reference CuI for which the NMR shift is reported to vary by only a few ppm from the standard used here, CuCl.

The $\alpha - \beta$ transition appears to commence near 355 K, where the NMR shift begins to increase, leading to a cusp at 385 K. A recent report examined calorimetric and XRD

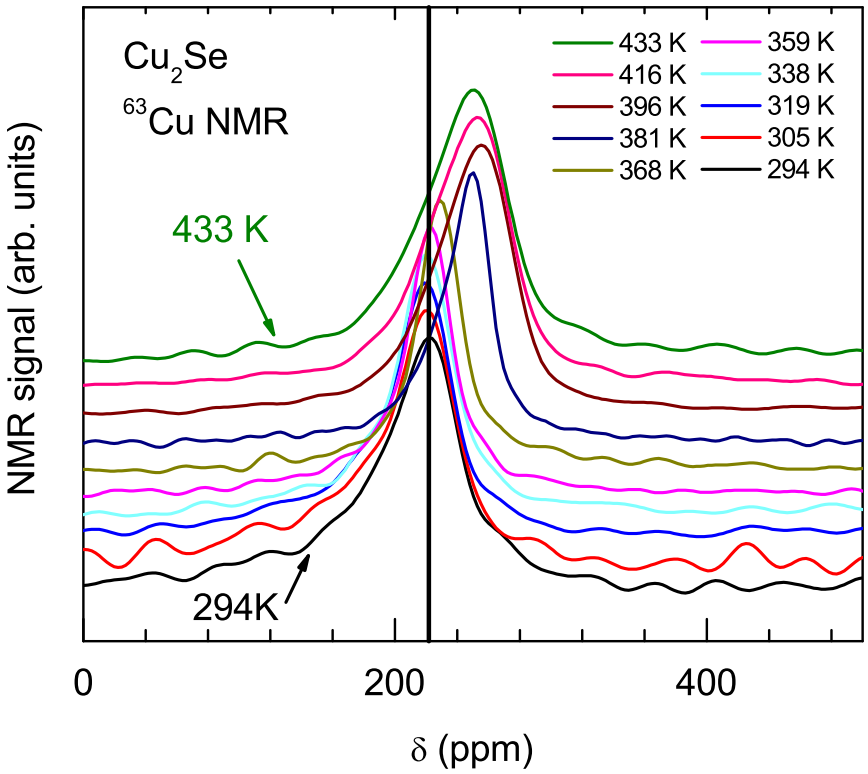

Figure 4.19: ^{63}Cu spectra at selected temperatures from 294 K to 433 K, with vertical separation for visibility. Results bracket the $\alpha - \beta$ transition at ∼355–385 K. Vertical line marks α-phase shift, δ = 220 ppm. Reprinted with permission from [140]. Copyright (2015) American Chemical Society.

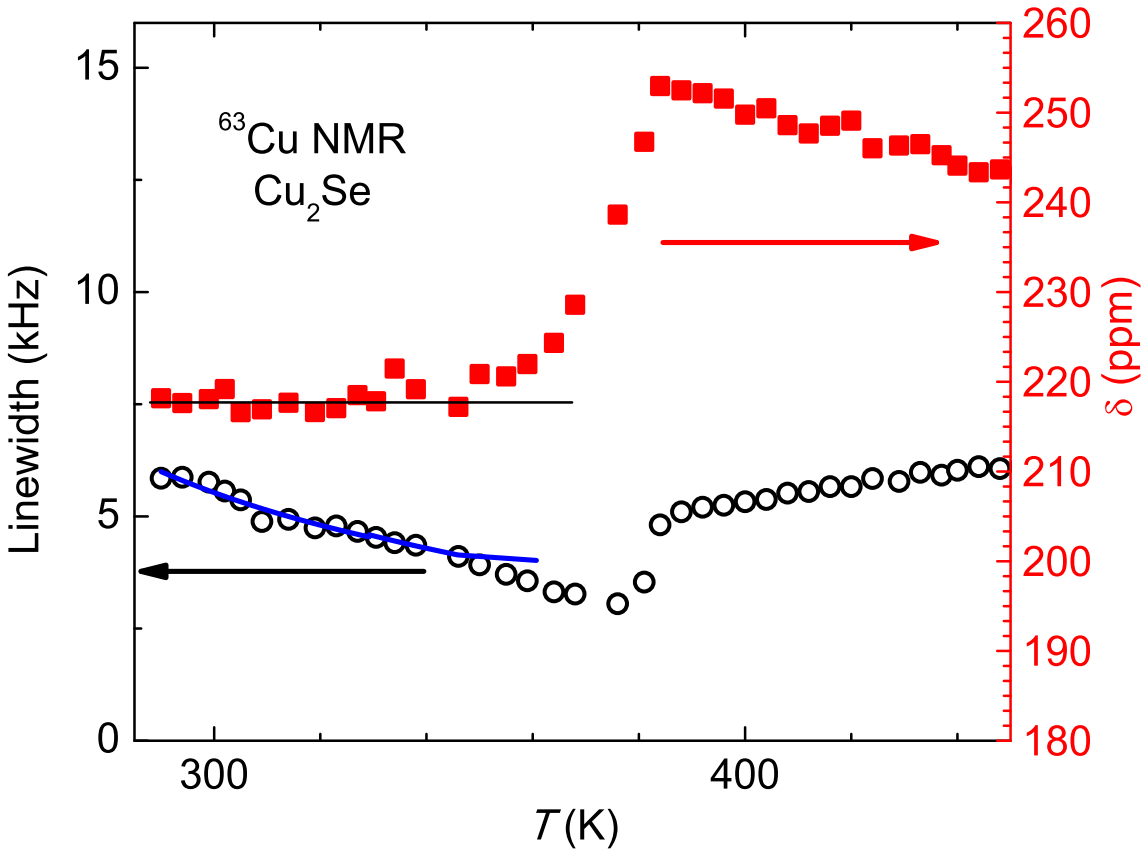

Figure 4.20: ^{63}Cu NMR shifts (squares, right axis) and linewidths (circles, left axis) vs temperature. Solid curve in lower plot: thermally activated fit described in text. Mean α-phase shift indicated by horizontal line. Reprinted with permission from [140]. Copyright (2015) American Chemical Society.

evidence [66] and indicated that the observed transformation covers a temperature range of about 40 K and should be considered second-order rather than first-order. The present results are in accord with the presence of a second order transition. Examining the NMR lines in the transformation region, it can be seen clearly that there is a progressive increase in frequency, not a bifurcation as would be expected if there were a phase coexistence as the $\alpha - \beta$ transformation progresses. However, as pointed out in the introduction an alternative view has been expressed for the $\alpha - \beta$ phase transition, as a mixture of two 1st and 2nd order phase transitions [78, 70]. Vučić [70] *et al.* showed that as the number of vacancies increases, the phase transitions will happen at two separate temperatures. In our sample [52] (with 0.05 vacancies in formula unit) the beginning of the lower temperature phase transition (continuous) can be seen as a gradual change in shift and also linewidth at 345 K in Figure 4.20 . Note that the electrical conductivity also has the same kink at 355 K. Meanwhile, the first-order phase transition can be seen from the NMR to happen at 385 K which is in accordance with the electrical conductivity [52]. These NMR data show clearly that there is gradual change in properties corresponds to a second-order transformation, however, the sudden change in properties at the 385 K transformation indicates that a mixed transformation provides the best picture from the results.

The widths plotted in Figure 4.20 are full widths at half maximum obtained by fitting a Lorentzian to each spectrum. The values show a small increase in the β phase, which we also found to have a small variation from run to run in the region just above the transition. Tentatively we assume this to indicate differences in the Cu vacancy distribution between crystallites within the β phase. However, below the transition the decrease in width vs temperature follows the expected behavior for thermally activated Cu-ion hopping. In this case the linewidth follows [163]

$$\Delta\nu = [(\Delta\nu_o)^2/\nu_{\rm a}] \times \exp(E_a/k_BT) + C, \tag{4.8}$$

where E_a is the activation energy for ionic motion, $\nu_{\rm a}$ the attempt frequency, and $\Delta\nu_o$ the NMR linewidth in absence of motion.

A fit to Eq. 4.8 over the narrow α-phase temperature range up to 340 K gives the solid curve in Figure 4.20, with parameters E_a = 0.08$\pm$0.07 eV, and prefactor $[(\Delta\nu_o)^2/\nu_{\rm a}]$ = 160$\pm$60 Hz. This is in the range of what has been measured by ion transport [164, 165]. For comparison, note that in the β phase, a corresponding fit yielded [160] E_a = 0.23 eV. The static α-phase NMR width ($\Delta\nu_o$) is unknown because of the ionic motion, however if we assume its width to be equal to the fitted low-temperature full-quadrupole width, $\Delta\nu_o \simeq$ 11 MHz as described above, the fitted curve yields an attempt frequency $\nu_{\rm a} \sim 0.8 \times 10^{12}$ Hz. In light of the large quadrupole-based NMR width identified here, the attempt frequency obtained for the α-phase is in the range of phonon frequencies (although with large uncertainty), corresponding to ion motion in Cu_2Se matching, the standard picture for thermally activated hopping. This is in contrast to the anomalous attempt frequencies derived from NMR results in some cases, thought to indicate departures from simple single-exponential hopping [49, 163, 166].

4.4.2.3 Low-Temperature Phase and Cu Dynamics

The Cu NMR spectrum for the lower temperature phase appears below about 150 K, as shown in Figure 4.21. These data were observed with a two-pulse spin echo sequence with fixed 100 μs delay between pulses, and the disappearance of the signal can be understood as the initiation of slow Cu ion hopping at these temperatures. Note that the data have been multiplied by T, since this product gives a temperature-independent measure of total NMR spectral weight. (Amplitudes are affected to a small extent by the temperature dependence of the receiving coil Q-factor, but these changes are small relative to the observed drop in signal above 90 K.)

In order to quantify the results, we fitted the line shapes of Figure 4.21 over the range

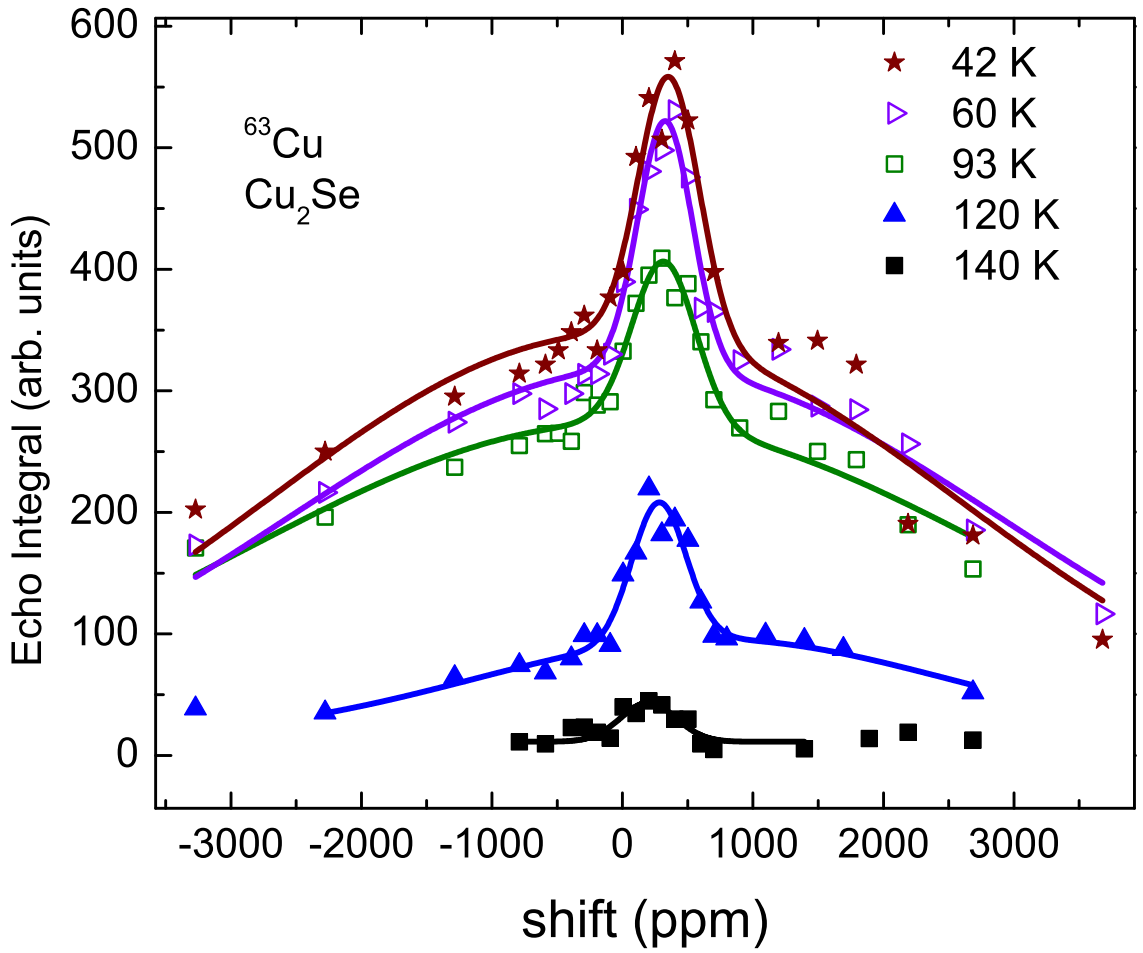

Figure 4.21: ^{63}Cu spin-echo line shapes vs temperature, with fitting results (solid curves). Amplitudes are normalized by multiplying by T. Reprinted with permission from [140]. Copyright (2015) American Chemical Society.

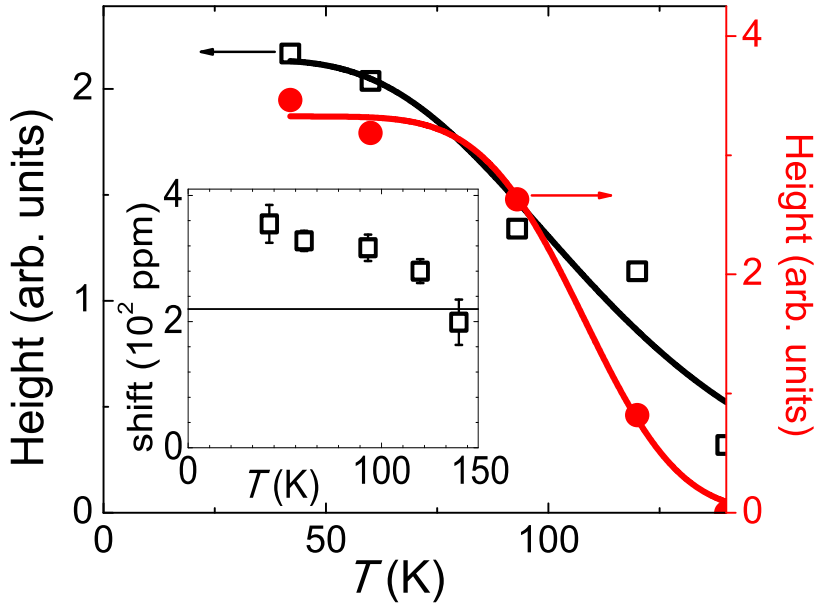

Figure 4.22: Fitted amplitudes from 2-peak fit, including fitted ^{63}Cu site A (squares, left axis) and site B (circles; right axis) results. Solid curves: activated fits described in text. Inset: Fitted site A positions, with horizontal line marking α phase line position. Reprinted with permission from [140]. Copyright (2015) American Chemical Society.

$\pm$2500 ppm using a simplified fitting scheme consisting of two Gaussian curves, one representing the narrow site A peak from our analysis of the line shape described above, and the other representing site B. The small-amplitude site C falls out of range of most of these measurements so we neglected to fit for this peak. The fitted curves are displayed in Figure 4.21, with resulting fitted parameters are shown in Figure 4.22.

To understand the disappearance of the signal near 100 K, note that for the echo experiment, changes in the resonance frequency of a Cu nucleus, caused for example by motion of the ion or one of its neighbors, will cause the loss of the echo signal if occurring during the 100 μs time scale of the echo experiment since a static frequency for each nucleus is required for the echo to refocus. This loss of signal will occur until the hopping rate be-

comes much larger; until finally when the rate becomes equivalent to the static linewidth [90] the motionally narrowed line will appear.

In terms of the quantities defined in Eq. 4.8, the mean hopping time for an activated process will be $\tau = (1/\nu_{\rm a}) \times \exp(E_a/k_BT)$. Taking fitted values from the α phase measurement yields an extrapolated hopping time 0.05 μs at 90 K, which remains fast on the time-scale of the echo experiment. On the other hand, fitting the echo amplitudes to obtain activation parameters, giving the solid curves in Figure 4.22, with echo decay according to $\exp[-t_{echo}/\tau]$, gives unphysically small attempt frequencies 0.2×10^6 and 8×10^6 s^{-1} for the two sites. Thus the results in Figure 4.21 indicate that stabilization of the Cu ion motion is associated with the α to α' structure change at these temperatures, not simply the slowing down of the α phase dynamics. The transformation proceeds gradually, leading to a low temperature state in which the Cu ions and vacancy positions become stable. The Gaussian-fitted position for site A (inset, Figure 4.22) similarly shows such behavior, with the shift gradually approaching the α phase value of δ_{iso} = 220 ppm (horizontal line) as the transformation proceeds. Thus the results point to the initiation of ion hopping at these temperatures coinciding with the change to the α phase structure.

4.4.3 Discussion

Regarding the low-temperature structure, we equate the two sites labeled A and B from the NMR fit to the main part of the structure, since as described above site C was associated with sites neighboring Cu vacancies. The recently described low-temperature α' structure [56] identified on the basis of *ab initio* results has 2 Cu sites, however with equal occupancy, which does not match the balance of assigned NMR spectral weights observed here. Note for comparison the α-phase (room temperature) structure of Ref. [62] has 12 Cu sites and a relatively large unit cell, with Cu ions segregated in two-dimensional stacks. By analogy it seems likely that the sites fitted in the NMR results represent multiple

crystallographic sites separated into two distinct types, perhaps as a superstructure based on the layered configuration [56] identified with the α' phase. More investigation appears to be needed to definitively understand these structures.

Examining the observed shifts and T_1 results also gives information about the local carrier behavior. At high temperatures, the shifts are magnetic in origin, since as noted above the quadrupole contribution is averaged to zero in the motional narrowing process. However the magnetic shift can be separated as $\delta_{iso} = \delta_{cs} + K$, where the former represents the chemical shift due to the orbital susceptibility of filled and empty bands, and the latter is the Knight shift associated with the spin susceptibility of charge carriers [92].

To estimate the size of the expected Knight shift, we take the measured hole concentration, which is $p = 6.6 \times 10^{20}\mathrm{cm}^{-3}$ at 473 K in the β phase. A hole effective mass m^*/m_o = 1.5 can be obtained by extrapolating the reported values [167] to this temperature. With these values the Fermi temperature will be $T_F = (3\pi^2 p)^{2/3}\hbar^2/(2m^* k_B)$ = 1900 K, and we see that the carriers are in the degenerate regime. In this case the density of states is $g(E_F) = 3E_F/(2p)$ = 0.13 states/eV per Cu ion, using the XRD results refined as described above to obtain the per-ion volume. The Knight shift will be [92] $K = \mu_B g_s(E_F) H_s^{HF}$, where H_s^{HF} is the contact hyperfine field for s-states (typically the dominant contribution), and $g_s(E_F)$ is the Cu s-partial contribution to $g(E_F)$. If all states corresponding to $g(E_F)$ were Cu s-states, and using [92] H_s^{HF} = 260 T we obtain K = 2000 ppm. The much smaller observed β phase shift indicates that in fact $K \approx 0$, representative of the p-state symmetry of the valence band edge. This is similar to other cubic direct-gap semiconductors and in agreement with DFT calculations [168] indicating such a band symmetry for cubic Cu_2Se.

It is interesting that in the α phase the NMR shift remains small, so that apparently $K \approx 0$ also, though the measured carrier density remains little changed, and here the corresponding estimate of K described above will be large if s-states dominate. While

features of the band structure are unknown in the more complicated structure, it appears that the α phase must also have negligible weight in Cu s-states at the valence band edge.

In contrast, the increased isotropic shifts in the α' phase at 77 K can be understood as largely due to an increase in Knight shift. Assuming the chemical shift to be the same as that of the α phase, $\delta_{cs} = 220$ ppm and subtracting from the measured shift, for site B we obtain $K = 588 - 220 = 368$ ppm. Using the measured magnetic relaxation rate for site B, $^{63}T_{1M}^{-1} = 1.7$ s^{-1} (Table 4.7, least squares mean of fitted values) we obtain a Korringa product $K^2T_{1M}T \approx 6.1 \times 10^{-6}$ sK. This is quite close to the value [92] 3.7×10^{-6} sK for ^{63}Cu in simple metals without strong exchange enhancement. Similarly for site A we obtain $K = 226$ ppm and $K^2T_{1M}T \approx 6.6 \times 10^{-6}$ sK, also within the expected range. This helps to confirm that indeed the enhanced shift is largely a Knight shift, signaling a change in electronic behavior in the low-temperature phase.

A calculation identical to the above for site C yields $K^2T_{1M}T \approx 57 \times 10^{-6}$ sK, with a larger Korringa enhancement of $\sim$16. Recalling that site C was associated with states localized near acceptors (Cu vacancies), we find that the situation is similar to that of P doped Si, which when heavily doped above $n \approx 10^{18}$ cm^{-3} forms an impurity band, with transport dominated by states near the donors. NMR studies in this regime [169] show that states near the donors exhibit a large Knight shift with Korringa product enhanced by $\sim$5-10, while states away from the donors exhibit a much weaker but nonzero Knight shift. The observed situation in Cu_2Se is quite similar, with our results indicating a small fraction of the sites having about 10 times the local density of states as compared to the rest of the material, and large Korringa enhancement. However, these regions are coupled together through the more weakly metallic behavior of the intervening material.

One of the features which has thus far prevented further application of Cu_2Se as a thermoelectric material is the mobility of the Cu ions, which affects the material's stability. Our results show that the α phase maintains Cu-ion dynamics down to about 100 K,

however below the α' structure change the ions become static. If this structure could be stabilized to higher temperatures there may be significant benefit for such applications. However the impurity band behavior identified in this temperature range may have significant consequences for the thermoelectric efficiency, as has been indicated by recent studies [22, 24].

4.5 Cu_2Te

Similar to Cu_2Se just described in the last section, Cu_2Te finds itself as a component of efficient solar cells in which Cu_2Te is used as a back contact for CdTe [51], and there has recently been enhanced interest due to high thermoelectric efficiency. These and related materials also include well known topological insulators due in part to the presence of heavy atoms [170, 171, 172]. In this work, we used NMR along with heat capacity measurements, to obtain physical insight into features of $Cu_{2-x}Te$ and $Cu_{2-x}Ag_{0.2}Te$. Ag substitution is shown to have a substantial effect on the activated hopping processes. Furthermore, identification of the charge-carrier contributions to the NMR shifts and relaxation behavior provides understanding of the hole bands contributing to the transport. Starting with these results, we also identify large negative chemical shifts in these materials, we show to be consistent with an inversion of the orbital occupation of the hole bands. A report of this work was already published and parts are reprinted with permission from [173].

4.5.1 Sample Preparation

Samples with the nominal compositions Cu_2Te and $Cu_{1.98}Ag_{0.2}Te$ studied here are from the same preparation batches as described in Ref. [52], using a combination of solid-state reaction and annealing followed by spark plasma sintering. Room temperature XRD and WDS measurements [52] showed that the Cu_2Te sample forms a single phase which can be fitted to the space group $P\bar{6}m2$ (#187). Similar to the behavior of $Cu_{2-x}Ag_xSe$,

Ag in Cu_2Te is well known to partially segregate to form the CuAgTe phase at ambient temperature [52], and the $Cu_{1.98}Ag_{0.2}Te$ sample was found from XRD to be composed of two phases: Cu_2Ag_xTe ($0.01 \leq x \leq 0.03$) and a small amount of CuAgTe. The Hall coefficients, thermal conductivities, and electrical conductivities were reported below 400 K in Ref. [52], showing that both samples are heavily-doped p-type semiconductors, with $p = 2.84 \times 10^{21}$ and 1.25 $\times 10^{21}$ cm^{-3} for Cu_2Te and $Cu_{1.98}Ag_{0.2}Te$ at room temperature, respectively. Note that in Ref. [54] in a comparison of different samples the carrier density of this Cu_2Te sample was misreported by a factor of about 3. Assuming all holes to be due to Cu vacancies the measured carrier density gives the composition $Cu_{1.85}Te$ for the Cu_2Te sample which is in good agreement with the phase diagram [85] according to the hexagonal structure fitted in PXRD. The same calculation for the Ag-doped sample gives 0.08 vacancies per formula unit, based on its reduced hole density.

4.5.2 Results and Analysis

4.5.2.1 Cu NMR

Figure 4.23(a) shows ^{63}Cu spectra for Cu_2Te versus temperature. The overall features are similar for ^{65}Cu spectra and for the $Cu_{1.98}Ag_{0.2}Te$ sample, shown in the inset of Figure 4.23(b). These line shapes are $m = 1/2$ to $-1/2$ transitions for $I = 3/2$ Cu nuclei. The gradual decrease of signal with temperature (Figure 4.23a) corresponds to the development of Cu-ion dynamics similar to Cu_2Se [103], discussed in Section 4.4.2.3.

Spin-lattice relaxation times (T_1) were obtained at several positions at 77 K to help distinguish distinct Cu sites. At 0 ppm (the narrow center of the spectrum), a single T_1 curve was found to give a good fit. For other positions, the recovery curves were best fitted to two T_1 curves, with similar results for several positions on the broader part of the spectrum, for which the fitted amplitudes for the shorter T_1 are more than 7 times larger than the long T_1. We assumed the latter to be a low-occupation site which we ignored

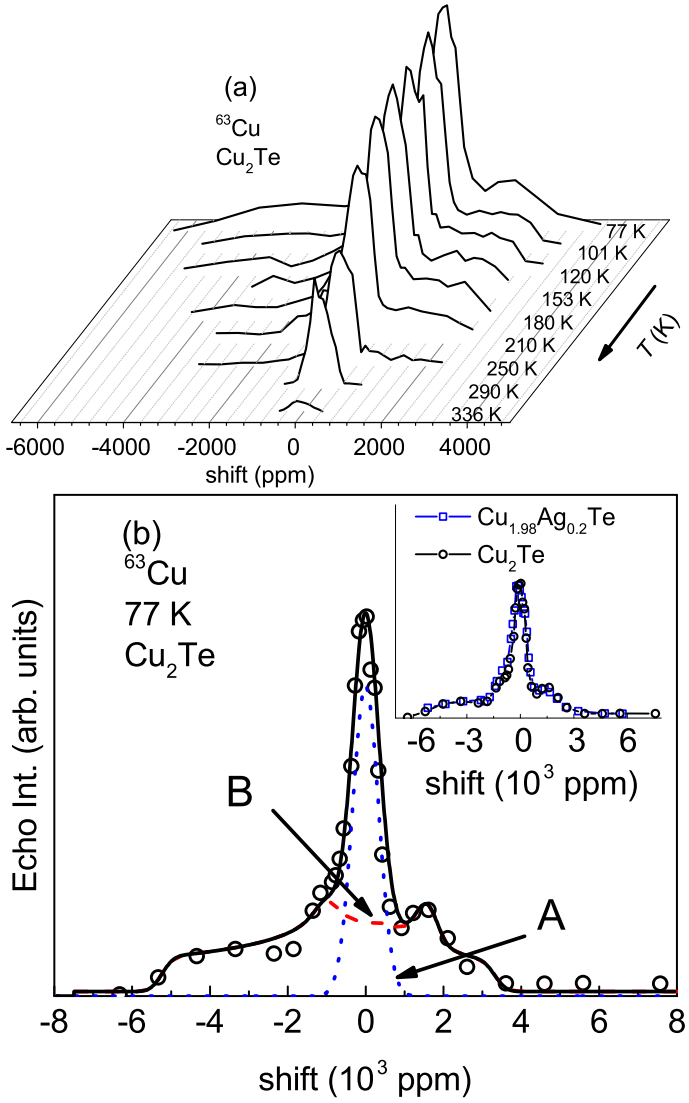

Figure 4.23: (a) ^{63}Cu spectra (echo integral $\times T$) vs temperature; (b) 77 K ^{63}Cu spectrum with fit (solid curve) including the narrow (dotted) and broad (dashed) resonances denoted sites A and B, respectively. Inset: ^{63}Cu spectra of both samples at 77 K. Positive shifts corresponds to paramagnetic sign, with shift including both the magnetic and quadrupole parts. Reprinted with permission from [173]. Copyright (2016) American Chemical Society.

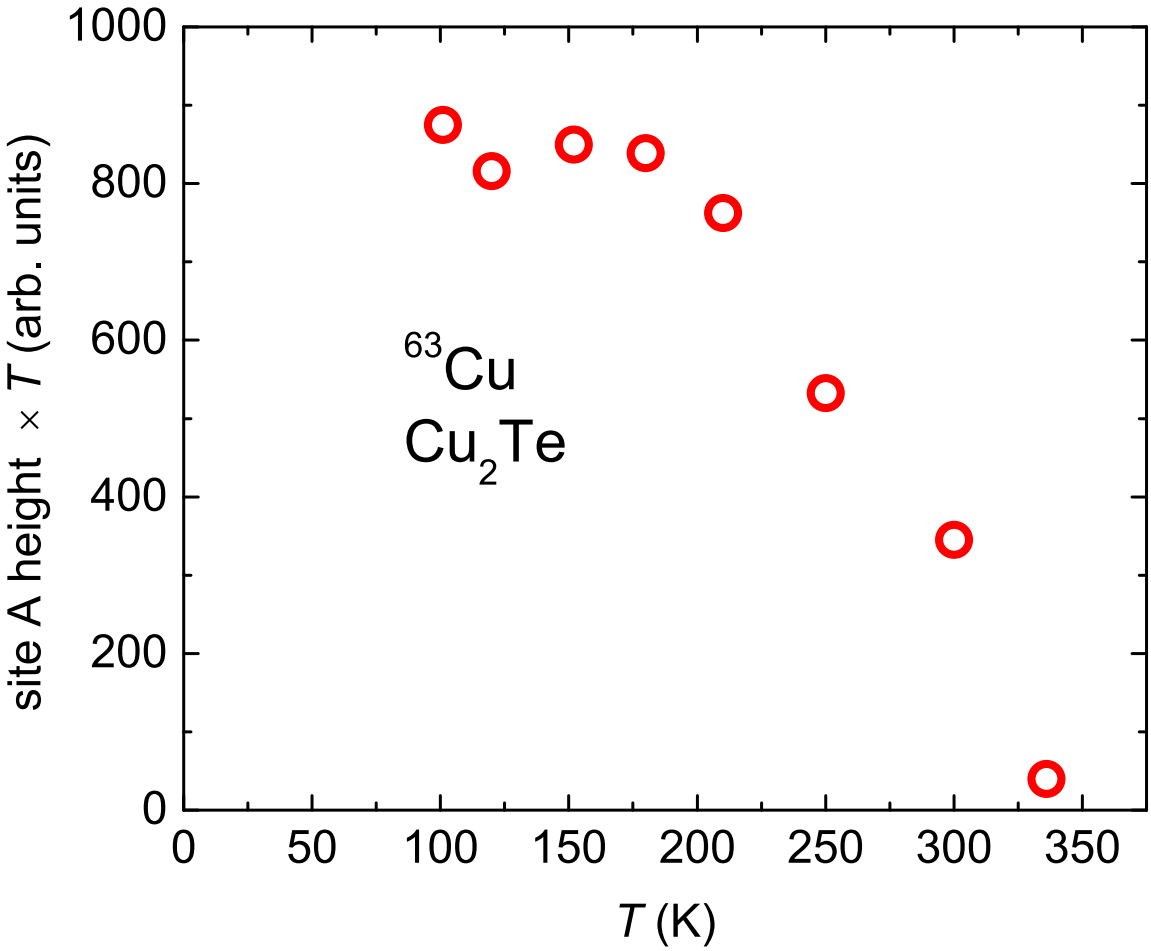

Figure 4.24: Fitted height of fitted ^{63}Cu NMR site A line, multiplying by T, for Cu_2Te. Reprinted with permission from [173]. Copyright (2016) American Chemical Society.

Table 4.8: 77 K T_1 values for ^{65}Cu and ^{63}Cu, and the separated magnetic ($^{63}T_{1M}^{-1}$) and quadrupole ($^{63}T_{1Q}^{-1}$) contributions obtained from measurements at positions indicated. Reprinted with permission from [173]. Copyright (2016) American Chemical Society.

Cu_2Te site	$^{63}T_1$ (ms)	$^{65}T_1$ (ms)	$^{63}T_{1M}^{-1}$ (s^{-1})	$^{63}T_{1Q}^{-1}$ (s^{-1})
site A (measured at 0 ppm)	172±4	166±4	4.02±0.68	1.67±0.77
site B (measured at 1300 ppm)	99±11	65±8	10.1±1.1	–

in the T_1 analysis. Table 4.8 shows resulting T_1 values with magnetic and quadrupole contributions separated.

Based on these results we fitted the spectra at 77 K as a sum of two sites [Figure 4.23(b)]. The narrow middle resonance (labeled site A) has found to have a magnetic shift $\delta_{total} = -50$ ppm (dotted line), while site B in the fitting has $\delta_{total} = 450$ ppm (dashed line). Site A could be fitted with no quadrupole contribution, while the broad portion of the line was fitted with quadrupole parameters $\nu_q = 10.5$ MHz and $\eta = 0.59$. The resulting spectral weights are 30% for site A and 70% for site B. The observation of two Cu NMR sites (and three Te NMR sites as shown below) is consistent with the Cu_2Te structure measurements; the hexagonal cell contains six Cu_2Te units, with detailed crystallographic positions not known.

The inset of Figure 4.23(b) compares the Cu spectra of the two samples. The fitting performed for $Cu_{1.98}Ag_{0.2}Te$ was similar to Cu_2Te with the resulting shifts of sites A and B reduced to $\delta_{total} = -90$ and 400 ppm, respectively. The smaller shifts for $Cu_{1.98}Ag_{0.2}Te$ result from its lower carrier density, hence smaller Knight shift contribution. It is also noted that we did not identify a separate CuAgTe peak for $Cu_{1.98}Ag_{0.2}Te$. The number of Cu nuclei in the CuAgTe phase should be around 8% of the total, based on the WDS compositions, and this signal is assumed to be hidden under the overall resonance line.

The effects of atomic dynamics can be seen in the temperature dependence of the spectra as shown in Figure 4.23(a). Similar to the Cu_2Se measurements reported earlier, these spectra were obtained using a spin-echo sequence with $t_{delay} = 100\ \mu$s between pulses. We multiplied the spectra by T since the total spectral weight is proportional to T^{-1}. Hopping during the time delay causes the echo signal to be reduced. To quantify these changes, we fitted for each temperature using the same shift parameters obtained for 77 K. Figure 4.24 displays the resulting site A height vs temperature. The decrease above 200 K is accompanied by the disappearance of site B [Figure 4.23(a)]. A similar temperature dependence was observed for $Cu_{1.98}Ag_{0.2}Te$ (not shown). The spectra disappear above 340 K for both samples and cannot be detected by spin-echo or free-induction decay sequences. Similar features were seen in Cu_2Se (discussed in Section 4.4.2.3), however, the Cu_2Se signal reappears as a motionally-narrowed line above 260 K indicating faster motion.

Further results showing development of atomic dynamics are shown through the spin-spin relaxation time (T_2). Confirmation of the dynamical basis of the results comes from spin-echo relaxation curves, shown here for the fitted Cu site A. The spin-echo integration vs $2t_{delay}$ is shown in Figure 4.25. The data were fitted to $C[(1-\alpha)\exp(-(2t_{delay}/T_{2g})^2)+ \alpha\exp(-2t_{delay}/T_{2e})]$ in which T_{2e} and T_{2g} are exponential and Gaussian decays, respectively. Exponential decay curves generally imply motional behavior, while Gaussian decay shapes are characteristic of dipolar interactions [90] among nuclei in a static lattice. The fitted parameters are given in Table 4.9. The reduction in T_{2e} and T_{2g} values and enhanced α at 290 K indicate Cu atomic motion.

^{63}Cu T_1 versus temperature is shown in Figure 4.26, measured at the center position of the line shape. Korringa behavior ($T_1T = \text{constant}$) is seen at low temperatures consistent with the metallic behavior of these samples. $1/T_1$ could be fitted over the full range to an activation formula, $f\exp(-\Delta E/K_BT) + BT$. The solid curves in Figure 4.26 show the results with activation energies $\Delta E = 0.35$ and 0.5 eV for Cu_2Te and $Cu_{1.98}Ag_{0.2}Te$,

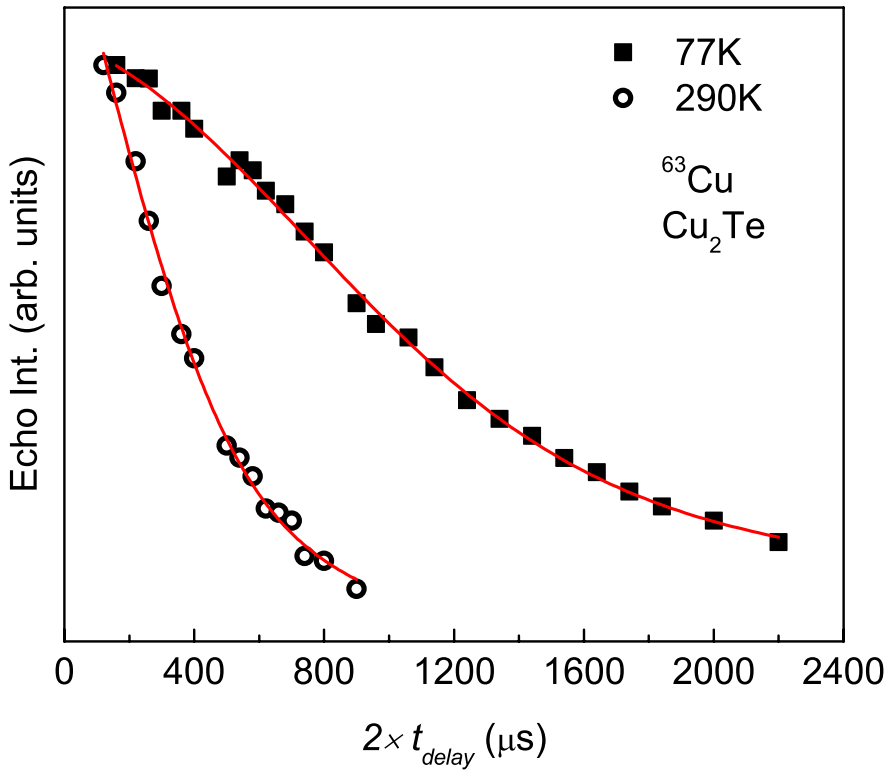

Figure 4.25: Echo integral vs $2t_{delay}$ at 77 K and 290 K for site A, showing T_2 behavior as described in the text. Reprinted with permission from [173]. Copyright (2016) American Chemical Society.

Table 4.9: T_2 fitting parameters for site A. Reprinted with permission from [173]. Copyright (2016) American Chemical Society.

T(K)	α	T_{2e} (μs)	T_{2g} (μs)
77	0.44	4440	2200
290	0.74	818	800

respectively.

We also measured ^{65}Cu as well as ^{63}Cu T_1 at selected temperatures, and separated the magnetic and quadrupole contributions using a procedure similar to what was demonstrated for other materials earlier in this thesis. Results are given in Table 4.8 for Cu_2Te at 77 K. Site B exhibited only a magnetic contribution, and for both sites we find that the magnetic contributions dominate at 77 K, not unexpected since the compounds are metallic [80, 82]. On the other hand, at room temperature, $^{65}T_1/^{63}T_1$ at site A is almost identical to $(^{63}Q/^{65}Q)^2$, indicating a switch to a quadrupole mechanism as a result of ionic motion.

4.5.2.2 Te NMR Results

Figure 4.27 shows a ^{125}Te NMR spectrum for the Cu_2Te sample. Measurements at 77 K, at 918, 1172, and 1504 ppm (squares in Figure 4.27) yielded $T_1 = 7.2 \pm 0.2$ ms, $T_1 = 6.7 \pm 0.2$ ms, and $T_1 = 4.7 \pm 0.2$ ms, respectively. Given these results and the observed shape, we fitted the spectrum to the three Gaussian curves labeled as C, D and E in Figure 4.27, with the results having almost identical spectral weights. The inset of Figure 4.27 shows $1/T_1T$ of site D vs temperature. The constant $1/T_1T$ follows Korringa-like metallic behavior [92] with no hopping behavior since spin 1/2 ^{125}Te is much less sensitive to atomic motion than the quadrupolar Cu nuclei.

For $Cu_{1.98}Ag_{0.2}Te$ the ^{125}Te spectrum also has obvious features similar to Cu_2Te and it was fitted in the same way. We obtained $T_1 = 7.2$, 7.3, and 6 ms at 77 K, at positions corresponding to sites C (901 ppm), D (1177 ppm), and E (1498 ppm), respectively. The decrease of ^{125}Te T_1 with increasing shift in both samples is consistent with the Korringa behavior, showing that the Knight shift is the main factor responsible for shifted parts of the Te spectrum, and thus the overall line shape.

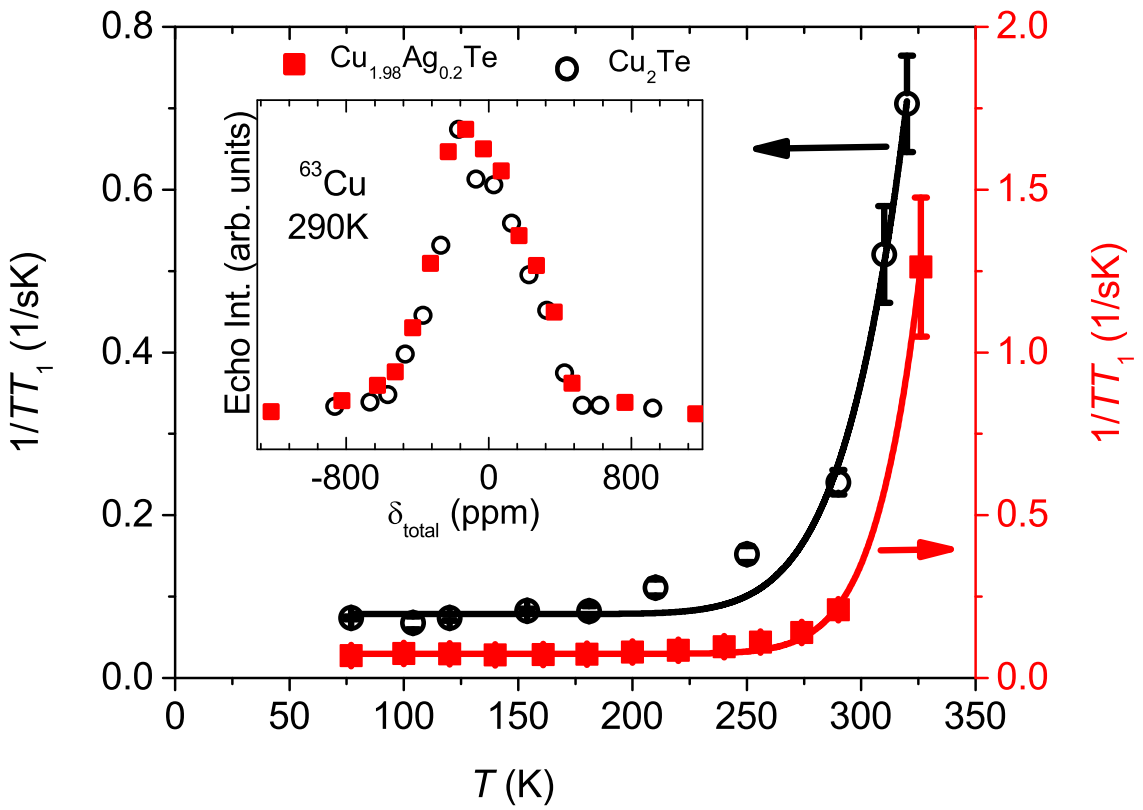

Figure 4.26: ^{63}Cu $1/TT_1$ vs temperature for Cu_2Te (circles) and $Cu_{1.98}Ag_{0.2}Te$ (squares) measured at the spectral maxim a solid curves are fits as explained in the text. Inset: ^{63}Cu spectra at 290 K, with the same symbols. Reprinted with permission from [173]. Copyright (2016) American Chemical Society.

4.5.2.3 Heat capacity of Cu_2Te

Heat capacity results for Cu_2Te are shown in Figure 4.28. At high temperatures the results exceed the classical Dulong-Petit value due to metastable occupation of Cu sites, as well established for superionic conductors. The inset shows C_p/T^3 vs T. The peak around 10 K indicates low-energy excitation modes, comparable to peaks also observed in amorphous and clathrate materials [29] corresponding to local oscillators. Therefore, we modeled the phonon contributions as described by Eqns. 4.7 with the additional of an

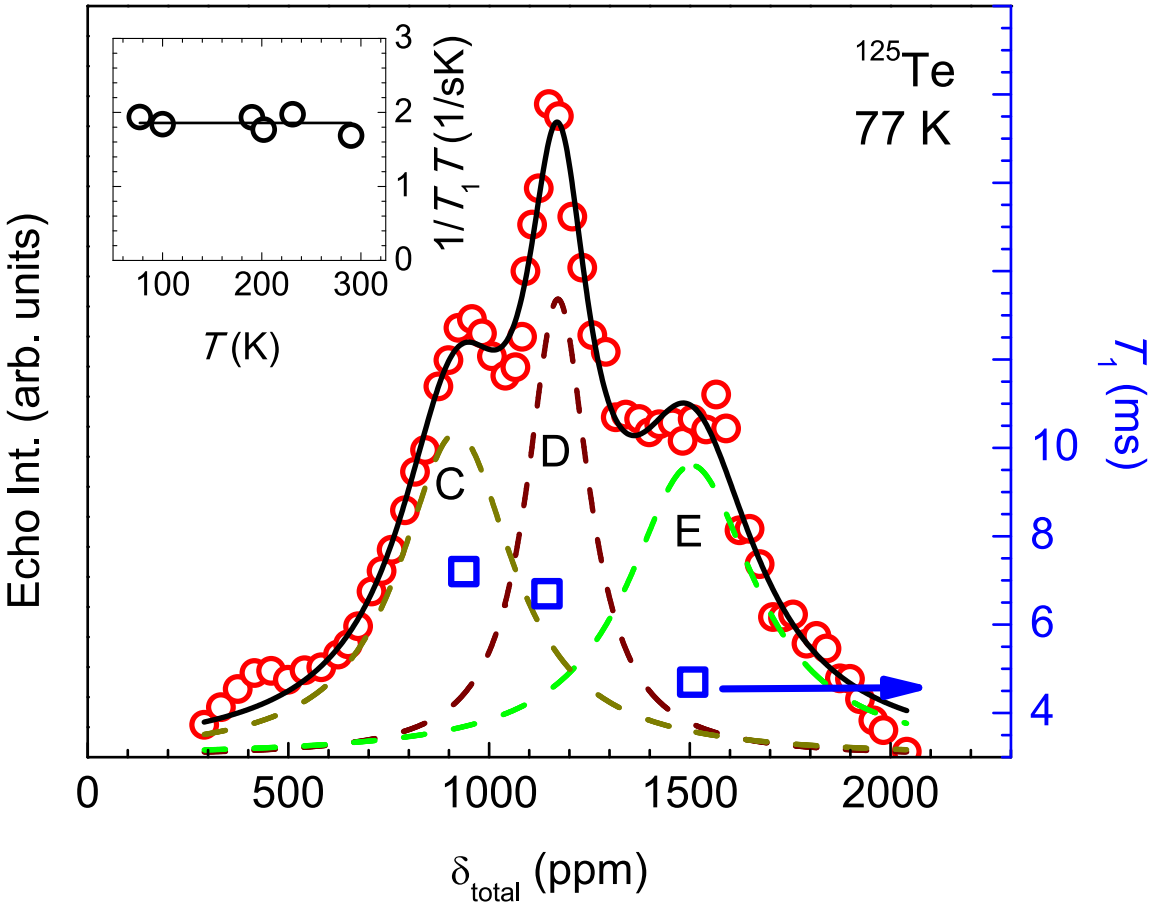

Figure 4.27: ^{125}Te spectra for the Cu_2Te sample. Dashed curves: Gaussian peaks fitted as explained in the text. The solid curve is the sum of these curves. Right axis: relaxation times (T_1) at three distinct positions (squares, with error bars smaller than symbols). Inset: $1/T_1T$ vs temperature at the peak position corresponding to site D, with Korringa fit given by solid line. Reprinted with permission from [173]. Copyright (2016) American Chemical Society.

electronic term ($C_\gamma = \gamma T$). We fixed the value $\gamma = 0.44$ mJ/mol K^2 obtained by fitting the low-T data (below 3 K) to $C_P/T = \gamma + \beta T^2$. Then we used this value with Eqns. 4.7 in a fit below 20 K to obtain the Einstein oscillator number $N_E = 0.12$ per formula unit, $\Theta_E = 47$ K, and $\Theta_D = 185$ K (see Table 4.10) for the remaining oscillators ($N_D = 2.73$ per formula unit). The total oscillator number is this fitted to 2.95 per f. u., very close to

Table 4.10: Heat capacity fitting parameters. Reprinted with permission from [173]. Copyright (2016) American Chemical Society.

γ(mJ/mol K^2)	N_D	N_E	Θ_D(K)$_{(<20\text{K})}$	Θ_D(K)	Θ_E(K)
0.44	2.73	0.12	185	220	47

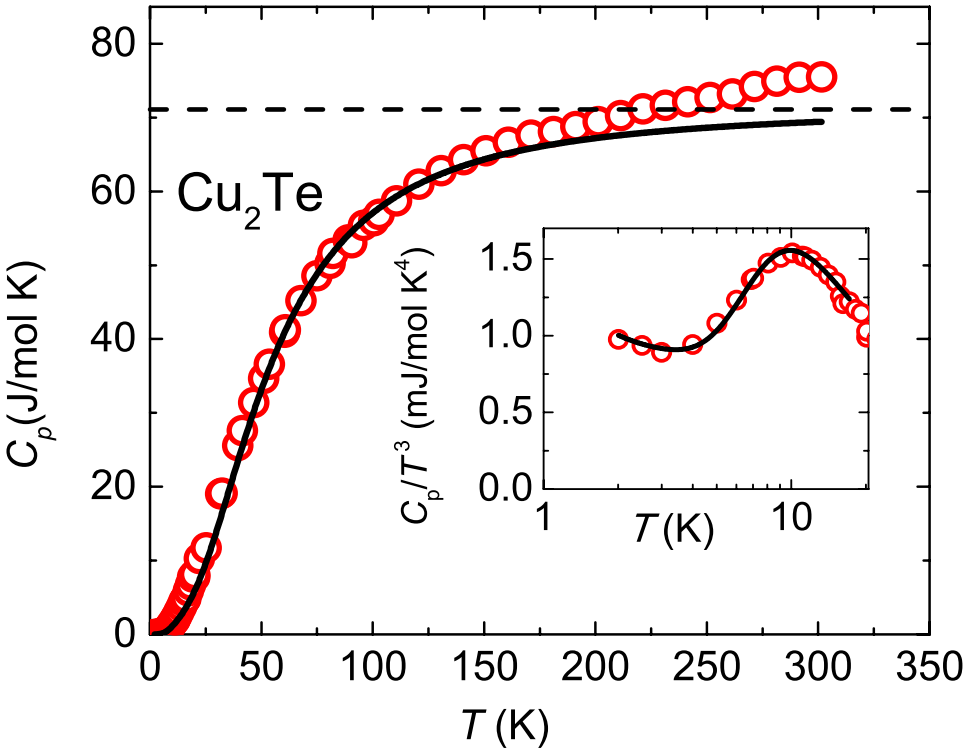

Figure 4.28: C_p vs temperature for the Cu_2Te sample. The solid curve us the fit explained in the text and the dashed line is the classical Dulong-Petit value. The inset shows C_p/T^3 vs T. Reprinted with permission from [173]. Copyright (2016) American Chemical Society.

the actual atomic composition. The solid curve in the inset of Figure 4.28 shows the fit. We also fitted over a wider range up to 200 K keeping the parameters unchanged except Θ_D. The solid line in Figure 4.28 exhibits the result with $\Theta_D = 220$ K obtained from the fit corresponding to, a small change of Θ_D with temperature, typical behavior of materials.

Einstein oscillators are localized vibrational modes and may be partially responsible for the low thermal conductivity [52] of Cu_2Te. It can be seen also that above 200 K the heat capacity gradually increases above the fitting curve (solid line) and Dulong-Petit value (dashed line) as noted this is due to additional degrees of freedom developing due to ionic motions. The onset of this rise coincides with the decrease of the NMR signal.

4.5.3 Discussion

For Cu NMR in Cu_2Te the fitting for $1/T_1$ vs T to the activation formula for Cu motion yielded $\Delta E = 0.35$ eV and $f = 7 \times 10^7$ s^{-1}. Likewise the fit gave $\Delta E = 0.5$ eV and $f = 2 \times 10^{10}$ s^{-1}for the Ag-doped sample. Both activation energies are larger than the result, $\Delta E = 0.23$ eV, for Cu_2Se [140] (see section 4.4.2.2). Transport measurements [174] on $Cu_{2-x}Te$ give $\Delta E = 0.4 \pm 0.03$ eV, in good agreement with the NMR results reported here.

The prefactor f in the T_1 fits corresponds in standard Bloembergen, Purcell, and Pound theory [175] to $f = f_0(\omega_{loc}/\omega_L)^2$, where f_0 is the atomic hopping attempt frequency and the ratio is that of the linewidth to the center frequency of the NMR spectrum. This is for the situation where the population of mobile ions is fixed [49], which should be the case here due to the large density of vacancies. Because Cu ions hop between sites with different quadrupole widths this ratio is difficult to determine precisely, however, using $\omega_{loc}/\omega_L \approx 0.007$ based on the observed spectrum width of Figure 4.23, the fitted prefactors correspond to an attempt frequency $f_0 = 1 \times 10^{12}$ Hz for Cu_2Te. This is comparable to ordinary phonon frequencies as expected for single-ion hopping processes [49]. The

larger f for $Cu_{1.98}Ag_{0.2}Te$ presumably reflects sampling of sites with larger ω_{loc} due to Ag alloying.

The Cu NMR spin-echo results demonstrate that the hopping mechanism in unsubstituted Cu_2Te remains unchanged below room temperature. Expressing the Arrhenius hopping rate as $1/\tau = f_0 \exp[-\Delta E/k_B T]$, and using $f_0 = 10^{12}$ Hz and the fitted $\Delta E = 0.35$ eV, τ is reduced to 200 μs (equal to the spin-echo time-scale of twice the separation between pulses) when the temperature drops to 220 K, the same as the temperature below which static behavior takes hold in Figure 4.24. The Te NMR Korringa behavior (Figure 4.27), which remains constant vs temperature, also shows that during the slowing down process, the electronic behavior remains unchanged. These results are in contrast to Cu_2Se which exhibits a structure change [52] as described in Section 4.4.2. In Cu_2Te the ions remain mobile, but with a much reduced hopping time at low-T. On the other hand, the enhanced activation energy of the Ag-substituted sample indicates that substitution is a way to stabilize the material against ionic motion, as may be needed for electronic applications.

The resonance shift (δ_{total}) is a sum of chemical shift (δ_{cs}) and Knight shift (K) contributions for each nucleus. Knight shifts can be obtained approximately from the Korringa relation [92]: since at 77 K both samples are in the metallic regime the Korringa product $[K^2 T_{1M} T = \hbar \gamma_e^2/(4\pi k_B \gamma_n^2)]$ is realized. For Cu nuclei, T_{1M} is the partitioned magnetic contribution described above, while for Te we assume T_1 due entirely to a magnetic mechanism. Using this method to calculate K and partition δ_{total}, The results are shown in Table 4.11 for the Cu_2Te sample, along with $(K^2 T_{1M} T)$ values. The same procedure for Cu site B yields K = 700 ppm and $\delta_{cs} = -250$ ppm, however the δ_{total} fit for this site includes a large model-dependent uncertainty due to the large quadrupole contribution, so we did not include that site in Table 4.11. We also did not make the dense set of Cu NMR measurements needed to isolate T_{1M} for Cu nuclei in the Ag-doped sample, however its

somewhat reduced Te relaxation rates yield a mean $\delta_{cs} = -1040$ ppm for the Te sites. For both samples, a striking result of this analysis is the large and negative chemical shifts obtained in all cases.

The Cu_2Te Knight shift can also be estimated from the measured electronic part of the heat capacity ($\gamma = 0.44$ mJ/mol K^2) with the assumption of a single hole pocket. The Knight shift is [92] $K = \mu_B g_s(E_F) H_s^{HF}$, where H_s^{HF} is the contact hyperfine field, and $g_s(E_F)$ is the s-partial contribution. The value $g(E_F) = 0.19$ states/(eV formula unit) was extracted from the specific heat, as noted above. If all states were s-states, equally distributed between Cu and Te, and using [92] H_s^{HF} = 260 and 1720 T for Cu and Te, respectively, we obtain $K = 930$ ppm for Cu, and 6190 ppm for Te. The observed Cu and Te Knight shifts (Table 4.11) are smaller than these estimates by a factor of 0.47 for Cu, and 0.38 for Te (taking the mean value for the latter). These results correspond to a 9 times larger s-fraction than the calculated results described above, for which $g_s(E)$ is about 5% of the total $g(E)$. Note that the ratio $g_s(E)/g_{\mathrm{total}}(E)$ is also essentially the same as Knight's ξ factor [92], indicating the fraction of electrons in *s*-orbitals contributing to the Knight shift. While ξ can cover a large range, when properly considering only the *s* electrons, estimates using standard values of H_s^{HF} have been established to provide good estimates of K and T_1, within a range of about 20% [121, 122]. Thus there is some uncertainty in using such values to estimate $g_s(E)$ from T_1, but it is much smaller than the factor of 9 difference from the calculated value.

Further, note that the Korringa product can also have a contribution due to electron-electron interactions; this term would enhance the susceptibility (and hence the Knight shift) over the free-electron value. This factor can be very significant for semiconductors near the metal-insulator transition, but it should be closer to unity for the present case, doped well into the metallic regime (as shown by the constant $1/[^{125}T_1T]$, Figure 4.27) but with relatively small carrier density compared to that of a metal. In most cases this

Table 4.11: Theoretical Korringa product [$K^2T_{1M}T$ in 10^{-6} sK], total fitted shift (δ_{total}), and chemical shift (δ_{cs}) and Knight shift (K) at 77 K drived from data for the Cu_2Te sample as explained in the text. Reprinted with permission from [173]. Copyright (2016) American Chemical Society.

	site A (^{63}Cu)	site C (^{125}Te)	site D (^{125}Te)	site E (^{125}Te)
$K^2T_{1M}T$	3.7	2.6	2.6	2.6
δ_{total} (ppm)	-50	918	1172	1504
K (ppm)	440	2170	2240	2710
δ_{cs} (ppm)	-490	-1250	-1070	-1200

effect leads to an enhancement of K relative to the Korringa value, but for example in P-doped silicon [132] the P NMR Korringa product approaches a value of about 62% of the free-electron value for carrier densities well into the metallic regime (e.g. K would be multiplied by a factor of 0.8). Comparing values in Table 4.11, we see that if K were reduced in this way, δ_{cs} for Cu becomes -400 ppm, while the smaller K yields δ_{cs} values for the three ^{125}Te sites with mean value -700 ppm. On the other hand, with an enhanced K^2T_1T the δ_{cs} results become correspondingly more negative. This indicates the range of negative chemical shifts implied by the measured results.

The Korringa T_1 results thus point to a relatively large *s*-contribution in the Cu_2Te valence band, approximately 9 times larger than the contribution obtained in the calculation. The smaller result approximately corresponds to a normal band structure with a *p*-dominated valence band edge and thus small g_s/g_{total} in these states, for both Cu and Te. In contrast to Cu_2Te, the Cu Knight shift and $1/T_{1M}$ in *p*-type Cu_2Se was shown [140] to be much smaller, and in good agreement with a set of DFT calculations reported [173]. Thus, there appears to be a qualitative difference between the band-edge behavior of Cu_2Te as opposed to the selenium analog.

In addition to the reduced density of *s*-states at the band edge the observed negative chemical shifts in Cu_2Te are also characteristic of systems with an inverted band structure. The Cu main for Cu_2Te peak falls in a chemical shift range outside of what is normally expected [176] for Cu, and the negative ^{125}Te shift is also at the far end of the reported range. For comparison, recent reports have identified [177, 178] PbTe to have a ^{125}Te shift corresponding to $\delta = -1150$ ppm, more positive than Cu_2Te, and other rock-salt- structure tellurides of which we are aware are reported to have more paramagnetic shifts. It was previously identified [179] that negative chemical shifts tend to be observed in topological insulators. The hexagonal Cu_2Te structure is believed to be a superstructure of the Nowotny structure [84], akin to hexagonal Ag_2Te and Ag_2Se, also known as topological insulators [170, 171, 172]. Thus there are several indicators that Cu_2Te may have a topologically interesting electronic structure. Clearly the band ordering and its orbital composition is significantly different from that of the parent cubic phase, as evidenced both by Knight shifts for both nuclei and by the chemical shifts.

5. SUMMARY AND CONCLUSIONS*

In summary, the metallic shifts and spin-lattice relaxation results for $Ba_8Ga_{16}Ge_{30}$ show the presence of a pseudogap in Ga states within the conduction band, superposed upon a large Ba *s*-electron contribution to the conduction band density of states compared to other type-I clathrates. Meanwhile the quadrupole contributions to the Ga relaxation rates are large and increasing more rapidly with temperature than in typical semiconductors. These results provide evidence for enhanced anharmonicity of the propagative phonon modes, a result with considerable importance for the reduction of thermal conductivity for thermoelectric applications.

In $Ba_8Cu_5Si_xGe_{41-x}$, we determined separately the chemical shifts and carrier-related Knight shifts. Surprisingly, the Cu NMR indicates that the band-edge behavior and distribution of states within the valence and conduction band remains essentially constant up to nearly complete Si substitution, at least from the perspective of Cu local orbitals. However for compositions close to $Ba_8Cu_5Si_{41}$ a rapid increase in shifts is observed, as well as an increase in Ba metallic shifts, which we connected to a greater hybridization and more

*Part of this section is reprinted with permission from "Pseudogap and anharmonic phonon behavior in $Ba_8Ga_{16}Ge_{30}$: An NMR study," A. A. Sirusi and J. H. Ross, Jr., *J. Chem. Phys.*, vol. 145, p. 054702, 2016. Right managed by AIP publishing LLC.

*Part of this section is reprinted with permission from "NMR study of $Ba_8Cu_5Si_xGe_{41-x}$ clathrate semiconductors," A. A. Sirusi *et al.*, *Phys. Chem. Chem. Phys.*, vol. 17, p. 16991, 2015. Reproduced by permission of the PCCP Owner Societies.

*Part of this section is reprinted with permission from "Synthesis, transport and magnetic properties of Ba-Co-Ge clathrates," A. A. Sirusi and J. H. Ross, Jr., *J. Electron. Mater.*, vol. 45, p. 1094, 2016. Copyright (2015), The Minerals, Metals & Materials Society.

*Part of this section is reprinted with permission from "Low-temperature structure and dynamics in Cu_2Se," A. A. Sirusi *et al.*, *J. Phys. Chem. C*, vol. 119, p. 20293, 2015. Copyright (2015) American Chemical Society.

*Part of this section is reprinted with permission from "Band ordering and dynamics of $Cu_{2-x}Te$ and $Cu_{1.98}Ag_{0.2}Te$," A. A. Sirusi *et al.*, *J. Phys. Chem. C*, vol. 120, p. 14549, 2016. Copyright (2016) American Chemical Society.

metallic behavior of the framework at this composition.

In the study of Type-I $Ba_8Co_xGe_{46-y}$ the results demonstrate vacancy formation similar to that of unsubstituted Ba_8Ge_{43}, but with the vacancy-ordering suppressed. Similar to other compositions close to Ba_8Ge_{43}, however, the vacancies appear not to moderate the carrier density, and instead the physical properties point to a complex Fermi surface property with a large effective carrier density. In chiral $Ba_6Co_xGe_{25-x}$ clathrates, the low-temperature structural transition transformation has a transition temperature that is significantly reduced, while the upper transformation temperature remains nearly unchanged. However the magnetic, calorimetric, and transport behavior demonstrate that the effect of these transitions on the electron density of states is strongly suppressed, in contrast to the behavior of unsubstituted material.

NMR studies of Cu_2Se were performed both near the 390 K $\alpha - \beta$ transition and at low temperatures. The spin echo results show the development of slow Cu-ion dynamics just above the α' transition near 100 K, while the motionally narrowed lines observed near room temperature and above correspond to more rapid activated Cu-ion hopping in both the α to β phases. Changes in line position signal a transformation from the α to β phase over the temperature range 355-385 K. The low-temperature phase exhibits a larger NMR shift than the room temperature α phase, identified as a Knight shift due to the native hole density. Fitting of the spectra in this temperature range gives a picture of Cu site occupations, and also indicates a significant local variation of hole density, with an enhanced density in positions associated with Cu vacancies.

In Cu_2Te, we identified an inverted band behavior in the low-temperature hexagonal phase of Cu_2Te; the NMR studies combined with specific heat and DFT calculations exhibit very large Knight shifts characteristic of such an inverted structure, and in addition the anomalous large negative chemical shifts are characteristic of what has been observed in topologically inverted systems. Based on these results, such a material may also show

potentially interesting transport behavior, such as the high mobilities Dirac carriers recently discovered in such systems. Additional measurements are currently proceeding as follow-up to these results.

REFERENCES

[1] T. J. Seebeck, "Magnetische polarisation der metalle und erze durch temperaturdifferenz," *Abh. K. Akad. Wiss. Berlin*, p. 265, 1822-1823.

[2] T. J. Seebeck, "Ueber die magnetische polarisation der metalle und erze durch temperaturdifferenz," *Ann. Phys.*, vol. 82, p. 253, 1826.

[3] J. Peltier, "Nouvelles experiences sur la caloricité des courants electrique," *Ann. Chim. Phys.*, vol. 56, p. 371, 1834.

[4] A. F. Ioffe, *Semiconductor thermoelements and thermoelectric cooling*. London : Infosearch Ltd., 1957.

[5] H. J. Goldsmid, *Introduction to Thermoelectricity*. Springer, 2010.

[6] C. Zhou, S. Birner, Y. Tang, K. Heinselman, and M. Grayson, "Driving perpendicular heat flow: $(p \times n)$-type transverse thermoelectrics for microscale and cryogenic peltier cooling," *Phys. Rev. Lett.*, vol. 110, p. 227701, 2013.

[7] G. J. Snyder and E. S. Toberer, "Complex thermoelectric materials," *Nat. Mater.*, vol. 7, pp. 105–114, 2008.

[8] J. R. Sootsman, D. Y. Chung, and M. G. Kanatzidis, "New and old concepts in thermoelectric materials," *Angew. Chem. Int. Ed.*, vol. 48, p. 8616, 2009.

[9] G. Chen, M. S. Dresselhaus, G. Dresselhaus, J. P. Fleurial, and T. Caillat, "Recent developments in thermoelectric materials," *Int. Mater. Rev.*, vol. 48, p. 45, 2003.

[10] B. Poudel, Q. Hao, Y. Ma, Y. Lan, A. Minnich, B. Yu, X. Yan, D. Wang, A. Muto, D. Vashaee, X. Chen, J. Liu, M. S. Dresselhaus, G. Chen, and Z. Ren, "High-thermoelectric performance of nanostructured bismuth antimony telluride bulk alloys," *Science*, vol. 320, p. 634, 2008.

[11] K. F. Hsu, S. Loo, F. Guo, W. Chen, J. S. Dyck, C. Uher, T. Hogan, E. K. Polychroniadis, and M. G. Kanatzidis, "Cubic $AgPb_mSbTe_{2+m}$: Bulk thermoelectric materials with high figure of merit," *Science*, vol. 303, p. 818, 2004.

[12] R. Venkatasubramanian, E. Siivola, T. Colpitts, and B. O'Quinn, "Thin film thermoelectric devices with high room-temperature figures of merit," *Nature*, vol. 413, p. 597, 2001.

[13] C. J. Vineis, A. Shakouri, A. Majumdar, and M. G. Kanatzidis, "Nanostructured thermoelectrics: Big efficiency gains from small features," *Adv. Mater.*, vol. 22, p. 3970, 2010.

[14] K. Biswas, J. He, , C.-I. Wu, T. P. Hogan, D. N. Seidman, V. P. Dravid, and M. G. Kanatzidis, "High-performance bulk thermoelectrics with all-scale hierarchical architectures," *Nature*, vol. 489, p. 414, 2012.

[15] J. S. Rhyee, K. H. Lee, S. M. Lee, E. Cho, S. I. Kim, E. Lee, Y. S. Kwon, J. H. Shim, and G. Kotliar, "Peierls distortion as a route to high thermoelectric performance in $In_4Se_{3-\delta}$ crystals," *Nature*, vol. 459, p. 965, 2009.

[16] E. J. Skoug and D. T. Morelli, "Role of lone-pair electrons in producing minimum thermal conductivity in nitrogen-group chalcogenide compounds," *Phys. Rev. Lett.*, vol. 107, p. 235901, 2011.

[17] X. Lu, D. T. Morelli, Y. Xia, and V. Ozolins, "Increasing the thermoelectric figure of merit of Tetrahedrites by Co-doping with nickel and zinc," *Chem. Mat.*, vol. 27, pp. 408–413, 2015.

[18] L.-D. Zhao, S.-H. Lo, Y. Zhang, H. Sun, G. Tan, C. Uher, C. Wolverton, V. P. Dravid, and M. G. Kanatzidis, "Ultralow thermal conductivity and high thermoelectric figure of merit in SnSe crystals," *Nature*, vol. 508, pp. 373–377, 2014.

[19] O. Delaire, J. Ma, K. Marty, A. F. May, M. A. McGuire, M.-H. Du, D. J. Singh, A. Podlesnyak, G. Ehlers, M. D. Lumsden, and B. C. Sales, "Giant anharmonic phonon scattering in PbTe," *Nat. Mater.*, vol. 10, pp. 614–619, 2011.

[20] G. A. Slack, "New materials and performance limits for thermoelectric cooling," in *CRC Handbook of Thermoelectrics* (D. M. Rowe, ed.), CRC Press, 1995.

[21] H. Liu, X. Shi, F. Xu, L. Zhang, W. Zhang, L. Chen, Q. Li, C. Uher, T. Day, and G. J. Snyder, "Copper ion liquid-like thermoelectrics," *Nat. Mater.*, vol. 11, p. 422, 2012.

[22] H. J. Goldsmid, "Improving the power factor and the role of impurity bands," *J. Electron. Mater.*, vol. 42, pp. 1482–1489, 2013.

[23] N. W. Ashcroft and N. Mermin, *Solid State Physics*. Philadelphia: Saunders College, 1976.

[24] J. P. Heremans, B. Wiendlocha, and A. M. Chamoire, "Resonant levels in bulk thermoelectric semiconductors," *Energy Environ. Sci.*, vol. 5, pp. 5510–5530, 2012.

[25] Y. Pei, X. Shi, A. LaLonde, H. Wang, L. Chen, and G. J. Snyder, "Convergence of electronic bands for high performance bulk thermoelectrics," *Nature*, vol. 473, pp. 66–69, 2011.

[26] G. S. Nolas, J. L. Cohn, G. A. Slack, and S. B. Schujman, "Semiconducting Ge clathrates: Promising candidates for thermoelectric applications," *Appl. Phys. Lett.*, vol. 73, p. 178, 1998.

[27] N. P. Blake, L. Mo/llnitz, G. Kresse, and H. Metiu, "Why clathrates are good thermoelectrics: A theoretical study of $Sr_8Ga_{16}Ge_{30}$," *J. Chem. Phys.*, vol. 111, p. 3133, 1999.

[28] B. B. Iversen, A. E. C. Palmqvist, D. E. Cox, G. S. Nolas, G. D. Stucky, N. P. Blake, and H. Metiu, "Why are clathrates good candidates for thermoelectric materials?," *J. Solid State Chem.*, vol. 149, p. 455, 2000.

[29] T. Takabatake, K. Suekuni, T. Nakayama, and E. Kaneshita, "Phonon-glass electron-crystal thermoelectric clathrates: Experiments and theory," *Rev. Mod. Phys.*, vol. 86, p. 669, 2014.

[30] E. S. Toberer, M. Christensen, B. B. Iversen, and G. J. Snyder, "High temperature thermoelectric efficiency in $Ba_8Ga_{16}Ge_{30}$," *Phys. Rev. B*, vol. 77, p. 075203, 2008.

[31] A. Saramat, G. Svensson, A. E. C. Palmqvist, C. Stiewe, E. Mueller, D. Platzek, S. G. K. Williams, D. M. Rowe, J. D. Bryan, and G. D. Stucky, "Large thermoelectric figure of merit at high temperature in Czochralski-grown clathrate $Ba_8Ga_{16}Ge_{30}$," *J. Appl. Phys.*, vol. 99, p. 023708, 2006.

[32] J. Martin, H. Wang, and G. S. Nolas, "Optimization of the thermoelectric properties of $Ba_8Ga_{16}Ge_{30}$," *Appl. Phys. Lett.*, vol. 92, p. 222110, 2008.

[33] G. S. Nolas, ed., *The Physics and Chemistry of Inorganic Clathrates*. Springer Netherlands, 2014.

[34] K. Suekuni, M. A. Avila, K. Umeo, and T. Takabatake, "Cage-size control of guest vibration and thermal conductivity in $Sr_8Ga_{16}Si_{30-x}Ge_x$," *Phys. Rev. B*, vol. 75, p. 195210, 2007.

[35] X. Yan, E. Bauer, P. Rogl, and S. Paschen, "Structural and thermoelectric properties of $Ba_8Cu_5Si_xGe_{41-x}$ clathrates," *Phys. Rev. B*, vol. 87, p. 115206, 2013.

[36] K. Suekuni, S. Yamamoto, M. A. Avila, and T. Takabatake, "Universal relation between guest free space and lattice thermal conductivity reduction by anharmonic rattling in type-I clathrates," *J. Phys. Soc. Jpn.*, vol. 77, p. 61, 2008.

[37] B. C. Sales, B. C. Chakoumakos, R. Jin, J. R. Thompson, and D. Mandrus, "Structural, magnetic, thermal, and transport properties of $X_8Ga_{16}Ge_{30}$ (X = Eu, Sr, Ba) single crystals," *Phys. Rev. B*, vol. 63, p. 245113, 2001.

[38] B. C. Chakoumakos, B. C. Sales, and D. G. Mandrus, "Structural disorder and magnetism of the semiconducting clathrate $Eu_8Ga_{16}Ge_{30}$," *J. Alloys Compd.*, vol. 322, p. 127, 2001.

[39] M. Christensen, S. Johnsen, and B. B. Iversen, "Thermoelectric clathrates of type I," *Dalton Trans.*, vol. 39, p. 978, 2010.

[40] M. A. Avila, K. Suekuni, K. Umeo, H. Fukuoka, S. Yamanaka, and T. Takabatake, "$Ba_8Ga_{16}Sn_{30}$ with type-I clathrate structure: Drastic suppression of heat conduction," *Appl. Phys. Lett.*, vol. 92, p. 041901, 2008.

[41] A. Bentien, M. Christensen, J. D. Bryan, A. Sanchez, S. Paschen, F. Steglich, G. D. Stucky, and B. B. Iversen, "Thermal conductivity of thermoelectric clathrates," *Phys. Rev. B*, vol. 69, p. 045107, 2004.

[42] A. Bentien, S. Johnsen, and B. B. Iversen, "Strong phonon charge carrier coupling in thermoelectric clathrates," *Phys. Rev. B*, vol. 73, p. 094301, 2006.

[43] J. L. Cohn, G. S. Nolas, V. Fessatidis, T. H. Metcalf, and G. A. Slack, "Glasslike heat conduction in high-mobility crystalline semiconductors," *Phys. Rev. Lett.*, vol. 82, pp. 779–782, 1999.

[44] M. Christensen, A. B. Abrahamsen, N. B. Christensen, F. Juranyi, N. H. Andersen, K. Lefmann, J. Andreasson, C. R. H. Bahl, and B. B. Iversen, "Avoided crossing of rattler modes in thermoelectric materials," *Nat. Mater.*, vol. 7, pp. 811–815, 2008.

[45] S. Pailhés, H. Euchner, M. Giordano, V., R. Debord, A. Assy, S. Gomes, A. Bosak, D. Machon, S. Paschen, and M. de Boissieu, "Localization of propagative phonons

in a perfectly crystalline solid," *Phys. Rev. Lett.*, vol. 113, p. 025506, 2014.

[46] T. Tadano, Y. Gohda, and S. Tsuneyuki, "Impact of rattlers on thermal conductivity of a thermoelectric clathrate: A first-principles study," *Phys. Rev. Lett.*, vol. 114, p. 095501, 2015.

[47] X. Zheng, S. Y. Rodriguez, and J. H. Ross Jr., "NMR relaxation and rattling phonons in the type-I $Ba_8Ga_{16}Sn_{30}$ clathrate," *Phys. Rev. B*, vol. 84, p. 024303, 2011.

[48] W. Gou, Y. Li, J. Chi, J. H. Ross, Jr., M. Beekman, and G. S. Nolas, "NMR study of slow atomic motion in $\mathrm{Sr_8Ga_{16}Ge_{30}}$ clathrate," *Phys. Rev. B*, vol. 71, p. 174307, 2005.

[49] J. B. Boyce and B. A. Huberman, "Superionic conductors: Transitions, structures, dynamics," *Phys. Rep.*, vol. 51, p. 189, 1979.

[50] D. R. Brown, T. Day, K. A. Borup, S. Christensen, B. B. Iversen, and G. J. Snyder, "Phase transition enhanced thermoelectric figure-of-merit in copper chalcogenides," *APL Mater.*, vol. 1, p. 052107, 2013.

[51] J. H. Yun, K. H. Kim, D. Y. Lee, and B. T. Ahn, "Back contact formation using Cu_2Te as a Cu-doping source and as an electrode in CdTe solar cells," *Sol. Energ. Mat. Sol. Cells*, vol. 75, p. 203, 2003.

[52] S. Ballikaya, H. Chi, J. R. Salvador, and C. Uher, "Thermoelectric properties of Ag-doped Cu_2Se and Cu_2Te," *J. Mater. Chem. A*, vol. 1, p. 12478, 2013.

[53] H. Liu, X. Yuan, P. Lu, X. Shi, F. Xu, Y. He, Y. Tang, S. Bai, W. Zhang, L. Chen, Y. Lin, L. Shi, H. Lin, X. Gao, X. Zhang, H. Chi, and C. Uher, "Ultrahigh thermoelectric performance by electron and phonon critical scattering in $Cu_2Se_{1-x}I_x$," *Adv. Mater.*, vol. 25, p. 6607, 2013.

[54] Y. He, T. Zhang, X. Shi, S.-H. Wei, and L. Chen, "High Thermoelectric Performance in Copper Telluride," *NPG Asia Mater.*, vol. 7, p. e210, 2015.

[55] Y. Tashiro, K. Taniguchi, and H. Miyasaka, "Copper selenide as a new cathode material based on displacement reaction for rechargeable magnesium batteries ," *Electrochimica Acta*, vol. 210, pp. 655 – 661, 2016.

[56] H. Chi, H. Kim, J. C. Thomas, G. Shi, K. Sun, M. Abeykoon, E. S. Bozin, X. Shi, Q. Li, X. Shi, E. Kioupakis, A. Van der Ven, M. Kaviany, and C. Uher, "Low-temperature structural and transport anomalies in Cu_2Se," *Phys. Rev. B*, vol. 89, p. 195209, 2014.

[57] S. Kashida and J. Akai, "X-ray diffraction and electron microscopy studies of the room-temperature structure of Cu_2Se," *J. Phys. C: Solid State Phys.*, vol. 21, p. 5329, 1988.

[58] S. A. Danilkin, "An investigation of the structural dynamics in the fast ionic conductor $Cu_{2-\delta}Se$ using neutron scattering," *J. Alloys Compd.*, vol. 467, p. 509, 2009.

[59] A. N. Skomorokhov, D. M. Trots, M. Knapp, N. N. Bickulova, and H. Fuess, "Structural behaviour of β-$Cu_{2-\delta}$ (δ =0, 0.15, 0.25) in dependence on temperature studied by synchrotron powder diffraction," *J. Alloys Compd.*, vol. 421, p. 64, 2006.

[60] T. Ohtani and M. Shohno, "Room temperature formation of Cu_3Se_2 by solid-state reaction between α-Cu_2Se and α-CuSe," *J. Solid State Chem.*, vol. 177, p. 3886, 2004.

[61] R. D. Heyding, "The copper/selenium system," *Can. J. Chem.*, vol. 44, p. 1233, 1966.

[62] L. Gulay, M. Daszkiewicz, O. Strok, and A. Pietraszko, "Crystal structure of Cu_2Se," *Chem. Met. Alloys*, vol. 4, p. 200, 2011.

[63] M. C. Nguyen, J.-H. Choi, X. Zhao, C.-Z. Wang, Z. Zhang, and K.-M. Ho, "New layered structures of cuprous chalcogenides as thin film solar cell materials: Cu_2Te and Cu_2Se," *Phys. Rev. Lett.*, vol. 111, p. 165502, 2013.

[64] R. D. Heyding and R. M. Murray, "The crystal structures of $Cu_{1.8}Se$, Cu_3Se_2 , α-and $\gamma-$CuSe, $CuSe_2$, and $CuSe_2$II," *Can. J. Chem.*, vol. 54, pp. 841–848, 1976.

[65] K. Yamamoto and S. Kashida, "X-ray study of the average structures of Cu_2Se and $Cu_{1.8}S$ in the room temperature and the high temperature phases," *J. Solid State Chem.*, vol. 93, pp. 202–211, 1991.

[66] H. Liu, X. Shi, M. Kirkham, H. Wang, Q. Li, C. Uher, W. Zhang, and L. Chen, "Structure-transformation-induced abnormal thermoelectric properties in semiconductor copper selenide," *Mater. Lett.*, vol. 93, p. 121, 2013.

[67] N. Frangis, C. Manolikas, and S. Amelinckx, "Vacancy-ordered superstructures in Cu_2Se," *Phys. Status Solidi A*, vol. 126, pp. 9–22, 1991.

[68] W. Borchart, "Gitterumwandlungen im system $Cu_{2-x}Se$," *Z. Kristallogr.*, vol. 106, p. 5, 1945.

[69] R. M. Murray and R. D. Heyding, "The copper–selenium system at temperatures to 850 K and pressures to 50 kbar," *Can. J. Chem.*, vol. 53, pp. 878–887, 1975.

[70] Z. Vučić, O. Milat, V. Horvatić, and Z. Ogorelec, "Composition-induced phase-transition splitting in cuprous selenide," *Phys. Rev. B*, vol. 24, pp. 5398–5401, 1981.

[71] O. Milat, Z. Vučić, and B. Ružžiź, "Superstructural ordering in low-temperature phase of superionic Cu_2Se," *Solid State Ionics*, vol. 23, pp. 37–47, 1987.

[72] P. Lu, H. Liu, X. Yuan, F. Xu, X. Shi, K. Zhao, W. Qiu, W. Zhang, and L. Chen, "Multiformity and fluctuation of Cu ordering in Cu_2Se thermoelectric materials," *J. Mater. Chem. A*, vol. 3, pp. 6901–6908, 2015.

[73] T. Ishikawa and S. Miyatani, "Electronic and ionic conduction in $Cu_{2-\delta}Se$, $Cu_{2-\delta}S$ and $Cu_{2-\delta}(Se,S)$," *J. Phys. Soc. Jpn.*, vol. 42, pp. 159–167, 1977.

[74] A. Tonejc, "Phase diagram and some properties of $Cu_{2-x}Se$ ($2.01 \geq 2-x \geq 1.75$)," *J. Mater. Sci.*, vol. 15, pp. 3090–3094, 1980.

[75] T. W. Day, K. A. Borup, T. Zhang, F. Drymiotis, D. R. Brown, X. Shi, L. Chen, B. B. Iversen, and G. J. Snyder, "High-temperature thermoelectric properties of $Cu_{1.97}Ag_{0.03}Se_{1+y}$," *Mater. Renew. Sustain. Energy*, vol. 3, pp. 1–7, 2014.

[76] G. D. Mahan, "The Seebeck coefficient of superionic conductors," *J. Appl. Phys.*, vol. 117, p. 045101, 2015.

[77] Y. Wang, N. S. Rogado, R. J. Cava, and N. P. Ong, "Spin entropy as the likely source of enhanced thermopower in $Na_xCo_2O_4$," *Nature*, vol. 423, pp. 425–428, 2003.

[78] S. D. Kang, S. A. Danilkin, U. Aydemir, M. Avdeev, A. Studer, and G. J. Snyder, "Apparent critical phenomena in the superionic phase transition of $Cu_{2-x}Se$," *New J. Phys.*, vol. 18, p. 013024, 2016.

[79] D. R. Brown, T. Day, T. Caillat, and G. J. Snyder, "Chemical stability of $(Ag,Cu)_2Se$: a historical overview," *J. Electron. Mater.*, vol. 42, p. 2014, 2013.

[80] S.-Y. Miyatani, S. Mori, and M. Yanagihara, "Phase diagram and electrical properties of $Cu_{2-\delta}Te$," *J. Phys. Soc. Jpn.*, vol. 47, pp. 1152–1158, 1979.

[81] S.-Y. Miyatani, "Electronic and ionic conduction in $(Ag_xCu_{1-x})_2Se$," *J. Phys. Soc. Jpn.*, vol. 34, pp. 423–432, 1973.

[82] X. Wu, J. Zhou, A. Duda, Y. Yan, G. Teeter, S. Asher, W. K. Metzger, S. Demtsu, S.-H. Wei, and R. Noufi, "Phase control of Cu_xTe film and its effects on CdS/CdTe solar cell," *Thin Solid Films*, vol. 515, pp. 5798–5803, 2007.

[83] G. Sorokin, Y. M. Papshev, and P. Oush, "Photoconductivity of Cu_2S, Cu_2Se and Cu_2Te," *Sov. Phys. Solid State*, vol. 7, p. 1810, 1966.

[84] H. Nowotny, "Die kristallstructur von Cu_2Te," *Z. MetaIlkd.*, vol. 37, p. 40, 1946.

[85] R. Blachnik, M. Lasocka, and U. Walbrecht, "The system copper-tellurium," *J. Solid State Chem.*, vol. 48, pp. 431–438, 1983.

[86] Patzak, "Uber die struktur und die lage der phasen im system kupfer-tellur," *Z. Metallkd.*, vol. 47, p. 418, 1956.

[87] N. Vouroutzis, N. Frangis, and C. Manolikas, "The double modulation superstructure of the room temperature stable phase of stoichiometric Cu_2Te," *phys. status solidi A*, vol. 202, pp. 271–280, 2005.

[88] Y. G. Asadov, S. Y. Asadova, A. I. Movlamverdieva, and F. K. Isaev, "Effect of zinc doping on the phase-transition temperatures of Cu_2Te," *Inorg. Mater.*, vol. 38, pp. 1103–1108, 2002.

[89] B. Yu, W. Liu, S. Chen, H. Wang, H. Wang, G. Chen, and Z. Ren, "Thermoelectric properties of copper selenide with ordered selenium layer and disordered copper layer," *Nano Energy*, vol. 1, p. 472, 2012.

[90] C. P. Slichter, *Principles of Magnetic Resonance*. Springer Science & Business Media, 1996.

[91] M. H. Levitt, *Spin Dynamics, Basics of Nuclear Magnetic Resonance*. Wiely, second ed., 2008.

[92] G. C. Carter, L. H. Bennett, and D. J. Kahan, "Metallic shifts in NMR," *Prog. Mater. Sci.*, vol. 20, p. 1, 1976.

[93] C. Kittle, *Introduction to Solid State Physics*. Wiley, 7th ed., 1996.

[94] J.-H. Chen, A. Sirusi Arvij, X. Zheng, S. Y. Rodriguez, and J. H. Ross, Jr., "NMR and computational study of $Ba_8Cu_xGe_{46-x}$ clathrate semiconductors," *J. Alloys Compd.*, vol. 593, p. 261, 2014.

[95] B. H. Toby, "EXPGUI, a graphical user interface for GSAS," *J. Appl. Crystallogr.*, vol. 34, pp. 210–213, 2001.

[96] A. C. Larson and R. B. V. Dreele, "General structure analysis system (GSAS)," Tech. Rep. LAUR 86-748 (2000), Los Alamos National Laboratory, 2000.

[97] K. Schwarz and P. Blaha, "Solid state calculations using WIEN2k," *Comput. Mater. Sci.*, vol. 28, pp. 259–273, 2003.

[98] D. Massiot, F. Fayon, M. Capron, I. King, S. Le Calvé, B. Alonso, J.-O. Durand, B. Bujoli, Z. Gan, and G. Hoatson, "Modelling one- and two-dimensional solid-state NMR spectra," *Magn. Reson. Chem.*, vol. 40, p. 70, 2002.

[99] T. Kemp and M. Smith, "QuadFit-a new cross-platform computer program for simulation of NMR line shapes from solids with distributions of interaction parameters," *Solid State Nucl. Mag.*, vol. 35, pp. 243 – 252, 2009.

[100] K. Momma and F. Izumi, "*VESTA3* for three-dimensional visualization of crystal, volumetric and morphology data," *J. Appl. Crystallogr.*, vol. 44, pp. 1272–1276, 2011.

[101] A. A. Sirusi and J. H. Ross, Jr., "Pseudogap and anharmonic phonon behavior in $Ba_8Ga_{16}Ge_{30}$: An NMR study," *J. Chem. Phys.*, vol. 145, p. 054702, 2016.

[102] E. Zintl, "Intermetallische verbindungen," *Angew. Chem.*, vol. 52, pp. 1–6, 1939.

[103] A. A. Sirusi, J. H. Ross, Jr., X. Yan, and S. Paschen, "NMR study of $Ba_8Cu_5Si_xGe_{41-x}$ clathrate semiconductors," *Phys. Chem. Chem. Phys.*, vol. 17, pp. 16991–16996, 2015.

[104] M. Kaupp, M. Bühl, and V. G. Malkin, eds., *Calculation of NMR and EPR Parameters: Theory and Applications*. Wiley-VCH, 1 ed., 2004.

[105] D. Arčon, A. Zorko, P. Jeglič, J. Xu, J. Tang, Y.Tanabe, S. Heguri, and K. Tanigaki, "Rattler site selectivity and covalency effects in type-I clathrates," *J. Phys. Soc. Jpn.*, vol. 82, p. 014703, 2013.

[106] J. Dolinšek, M. Klanjšek, T. Apih, A. Smontara, J. C. Lasjaunias, J. M. Dubois, and S. J. Poon, "Searching for sharp features in the pseudogap of icosahedral quasicrystals by NMR," *Phys. Rev. B*, vol. 62, pp. 8862–8870, 2000.

[107] X.-P. Tang, E. A. Hill, S. K. Wonnell, S. J. Poon, and Y. Wu, "Sharp feature in the pseudogap of quasicrystals detected by NMR," *Phys. Rev. Lett.*, vol. 79, pp. 1070–1073, 1997.

[108] J. Winter, *Magnetic resonance in metals*. Clarendon Press Oxford, 1971.

[109] X. Zheng, *NMR and transport studies on group IV clathrates and related intermetallic materials*. PhD thesis, Texas A&M University, 2012.

[110] D. Kölbl, D. M. Zumbühl, A. Fuhrer, G. Salis, and S. F. Alvarado, "Breakdown of the Korringa law of nuclear spin relaxation in metallic GaAs," *Phys. Rev. Lett.*, vol. 109, p. 086601, 2012.

[111] H. Tou, K. Sonoda, K. Furumoto, H. Kotegawa, K. Suekuni, M. A. Avila, and T. Takabatake, "Strong coupling of rattling phonon to conduction electrons in semimetallic type-i clathrate $Ba_8Ga_{16}Sn_{30}$," *J. Phys. Soc. Jpn.*, vol. 82, p. 114603, 2013.

[112] A. Abragam, *Principles of Nuclear Magnetism*. London: Oxford University Press, 1982.

[113] J. V. Kranendonk and M. B. Walker, "Theory of spin-lattice relaxation in anharmonic crystals," *Can. J. Phys.*, vol. 46, pp. 2441–2461, 1968.

[114] R. C. Zamar and C. E. González, "Nuclear quadrupole spin-lattice relaxation in anharmonic molecular crystals," *Phys. Rev. B*, vol. 51, pp. 932–944, 1995.

[115] G. R. Khutsishvili, "Nuclear magnetic relaxation in ionic crystals," *Sov. Phys. JETP*, vol. 4, p. 382, 1957.

[116] B. Tasche and H. Richtering, "Kernspin-Gitter-Relaxation von 115In und 75As in InAs zwischen 300 und 1000 K und die diffusion von kupfer in InAs," *Phys. Status Solidi A*, vol. 95, pp. 565–571, 1986.

[117] J. A. McNeil and W. G. Clark, "Nuclear quadrupolar spin-lattice relaxation in some III-V compounds," *Phys. Rev. B*, vol. 13, pp. 4705–4713, 1976.

[118] M. Corti, A. Gabetta, M. Fanciulli, A. Svane, and N. E. Christensen, "$^{69,71}\mathrm{Ga}$ NMR spectra and relaxation in wurtzite GaN," *Phys. Rev. B*, vol. 67, p. 064416, 2003.

[119] I. L. Moudrakovski, "Recent advances in solid-state NMR of Alkaline Earth Elements," in *Annual Reports on NMR Spectroscopy*, pp. 129–240, Elsevier BV, 2013.

[120] R. E. Watson and L. H. Bennett, "Calculation of atomic hyperfine-field coupling constants," *Phys. Rev. B*, vol. 15, pp. 502–503, 1977.

[121] J. J. van der Klink and H. Brom, "NMR in metals, metal particles and metal cluster compounds," *Prog. Nucl. Magn. Reson. Spectrosc.*, vol. 36, pp. 89–201, 2000.

[122] M. Saeed, T. Wazumi, K.-i. Kumagai, Y. Nakajima, and T. Tamegai, "NMR study of two-gap superconductivity in $Lu_2Fe_3Si_5$," *J. Phys. Soc. Jpn.*, vol. 82, p. 064705, 2013.

[123] C. Gatti, L. Bertini, N. P. Blake, and B. B. Iversen, "Guest–framework interaction in type I inorganic clathrates with promising thermoelectric properties: On the ionic

versus neutral nature of the alkaline-earth metal guest a in $A_8Ga_{16}Ge_{30}$ (A = Sr, Ba)," *Chem.-Eur. J.*, vol. 9, pp. 4556–4568, 2003.

[124] G. K. H. Madsen, K. Schwarz, P. Blaha, and D. J. Singh, "Electronic structure and transport in type-I and type-VIII clathrates containing strontium, barium, and europium," *Phys. Rev. B*, vol. 68, p. 125212, 2003.

[125] D. C. Li, L. Fang, S. K. Deng, H. B. Ruan, M. Saleem, W. H. Wei, and C. Y. Kong, "Structural and electronic properties of type-I clathrates $M_8Ga_{16}Ge_{30}$ (M = Ba, Sr, Yb) from first-principles calculations," *J. Electron. Mater.*, vol. 40, pp. 1298–1303, 2011.

[126] G. T. de Laissardiere, D. Nguyen-Manh, and D. Mayou, "Electronic structure of complex Hume-Rothery phases and quasicrystals in transition metal aluminides," *Prog. Mater. Sci.*, vol. 50, pp. 679 – 788, 2005.

[127] G. K. H. Madsen, A. Katre, and C. Bera, "Calculating the thermal conductivity of the silicon clathrates using the quasi-harmonic approximation," *Phys. Status Solidi A*, vol. 213, pp. 802–807, 2016.

[128] H. Euchner, S. Pailhès, L. T. K. Nguyen, W. Assmus, F. Ritter, A. Haghighirad, Y. Grin, S. Paschen, and M. de Boissieu, "Phononic filter effect of rattling phonons in the thermoelectric clathrate $Ba_8Ge_{40+x}Ni_{6-x}$," *Phys. Rev. B*, vol. 86, p. 224303, 2012.

[129] Y. He, F. Sui, S. M. Kauzlarich, and G. Galli, "Si-based earth abundant clathrates for solar energy conversion," *Energy Environ. Sci.*, vol. 7, p. 2598, 2014.

[130] S. Johnsen, A. Bentien, G. K. H. Madsen, M. Nygren, and B. B. Iversen, "Crystal structure and transport properties of nickel containing germanium clathrates," *Phys. Rev. B*, vol. 76, p. 245126, 2007.

[131] R. K. Harris and E. D. Becker, "NMR nomenclature: Nuclear spin properties and conventions for chemical shifts—IUPAC recommendations," *J. Magn. Reson.*, vol. 156, p. 323, 2002.

[132] M. J. R. Hoch and D. F. Holcomb, "^{31}P knight shifts and spin dynamics in Si:P at temperatures comparable to the Fermi temperature," *Phys. Rev. B*, vol. 71, p. 035115, 2005.

[133] F. Shimizu, Y. Maniwa, K. Kume, H. Kawaji, S. Yamanaka, and M. Ishikawa, "NMR study in the superconducting silicon clathrate compound $Na_xBa_ySi_{46}$," *Phys. Rev. B*, vol. 54, p. 13242, 1996.

[134] F. Kanetake, A. Harada, H. Mukuda, Y. Kitaoka, T. Rachi, K.Tanigaki, K. M. Itoh, and E. E. Haller, "73Ge- and 135/137Ba-NMR studies of clathrate superconductor $Ba_{24}Ge_{100}$," *J. Phys. Soc. Jpn.*, vol. 78, p. 104710, 2009.

[135] T. J. Rowland, "Knight shift measurements for Ba^{135}, Ba^{137}, Cd^{111}, and Cd^{113}," *Phys. Rev.*, vol. 103, p. 1670, 1956.

[136] G. A. Styles and G. Tranfield, "The Knight shift of barium," *Phys. Lett. A*, vol. 48, p. 471, 1974.

[137] S. Johnsen, A. Bentien, G. K. H. Madsen, B. B. Iversen, and M. Nygren, "Crystal structure, band structure, and physical properties of $Ba_8Cu_{6-x}Ge_{40+x}$ ($0 \leq x \leq 0.7$)," *Chem. Mater.*, vol. 18, p. 4633, 2006.

[138] R. J. Goodfellow, "Group VIII transition metals," in *Multinuclear NMR* (J. Mason, ed.), Springer US, 1987.

[139] K. D. Becker and H. P. Schäfgen, "NMR chemical shifts in copper (I) chalcogen compounds," *Solid State Commun.*, vol. 32, p. 1107, 1979.

[140] A. A. Sirusi, S. Ballikaya, C. Uher, and J. H. Ross, Jr., "Low-temperature structure and dynamics in Cu_2Se," *J. Phys. Chem. C*, vol. 119, pp. 20293–20298, 2015.

[141] A. A. Sirusi and J. H. Ross, Jr., "Synthesis, transport and magnetic properties of Ba-Co-Ge clathrates," *J. Electron. Mater.*, vol. 45, pp. 1094–1100, 2016.

[142] S. Paschen, V. H. Tran, M. Baenitz, W. Carrillo-Cabrera, Y. Grin, and F. Steglich, "Clathrate Ba_6Ge_{25}: Thermodynamic, magnetic, and transport properties," *Phys. Rev. B*, vol. 65, p. 134435, 2002.

[143] U. Aydemir, C. Candolfi, H. Borrmann, M. Baitinger, A. Ormeci, W. Carrillo-Cabrera, C. Chubilleau, B. Lenoir, A. Dauscher, N. Oeschler, F. Steglich, and Y. Grin, "Crystal structure and transport properties of $Ba_8Ge_{43}\square_3$," *Dalton Trans.*, vol. 39, pp. 1078–1088, 2010.

[144] A. Grytsiv, N. Melnychenko-Koblyuk, N. Nasir, P. Rogl, A. Saccone, and H. Schmid, "Formation of clathrates Ba–M–Ge (M = Mn, Fe, Co)," *Int. J. Mater. Res.*, vol. 100, pp. 189–202, 2009.

[145] Y. Li, J. Chi, W. Gou, S. Khandekar, and J. H. Ross, Jr., "Structure and stability of Ba-Cu-Ge type-I clathrates," *J. Phys.: Condens. Matter*, vol. 15, p. 5535, 2003.

[146] U. Aydemir, C. Candolfi, A. Ormeci, M. Baitinger, N. Oeschler, F. Steglich, and Y. Grin, "High temperature thermoelectric properties of the type-I clathrate Ba_8 $Ni_xGe_{46-x-y}\ \square_y$," *J. Phys.: Condens. Matter*, vol. 26, p. 485801, 2014.

[147] X. Shi, J. Yang, S. Bai, H. Yang, J.and Wang, M. Chi, J. R. Salvador, W. Zhang, L. Chen, and W. Wong-Ng, "On the design of high-efficiency thermoelectric clathrates through a systematic cross-substitution of framework elements," *Adv. Funct. Mater.*, vol. 20, pp. 755–763, 2010.

[148] S. Y. Rodriguez, L. Saribaev, and J. H. Ross, Jr., "Zintl behavior and vacancy formation in type-I Ba-Al-Ge clathrates," *Phys. Rev. B*, vol. 82, p. 064111, 2010.

[149] C. Candolfi, A. Ormeci, U. Aydemir, M. Baitinger, N. Oeschler, Y. Grin, and F. Steglich, "Multiband conduction in the type-I clathrate $Ba_8Ge_{43}\square_3$," *Phys. Rev. B*, vol. 84, p. 205118, 2011.

[150] S.-J. Kim, S. Hu, C. Uher, T. Hogan, B. Huang, J. D. Corbett, and M. G. Kanatzidis, "Structure and thermoelectric properties of Ba_5Ge_{25-x}, $Ba_6Ge_{23}Sn_2$, and $Ba_6Ge_{22}In_3$: Zintl phases with a chiral clathrate structure," *J. Solid State Chem.*, vol. 153, pp. 321–329, 2000.

[151] I. Zerec, A. Yaresko, P. Thalmeier, and Y. Grin, "Band-structure calculations for Ba_6Ge_{25} and $Ba_4Na_2Ge_{25}$ clathrates," *Phys. Rev. B*, vol. 66, p. 045115, 2002.

[152] D. Schopf, H. Euchner, and H.-R. Trebin, "Effective potentials for simulations of the thermal conductivity of type-I semiconductor clathrate systems," *Phys. Rev. B*, vol. 89, p. 214306, 2014.

[153] L. N. Mulay and E. A. Boudreaux, eds., *Theory and applications of molecular diamagnetism*. Wiley New York, 1976.

[154] I. Zerec, W. Carrillo-Cabrera, V. Voevodin, J. Sichelschmidt, F. Steglich, Y. Grin, and S.-I. Yaresko, A.and Kimura, "Influence of cage distortions on the electronic structure and optical properties of $Ba_{24}Ge_{100}$," *Phys. Rev. B*, vol. 72, p. 045122, 2005.

[155] T. Rachi, M. Kitajima, K. Kobayashi, F. Guo, T. Nakano, Y. Ikemoto, K. Kobayashi, and K. Tanigaki, "Soft x-ray spectroscopy of $Ba_{24}Ge_{100}$: Electronic phase transition and Ba-atom rattling," *J. Chem. Phys.*, vol. 123, p. 074503, 2005.

[156] H. Q. Yuan, F. M. Grosche, W. Carrillo-Cabrera, V. Pacheco, G. Sparn, M. Baenitz, U. Schwarz, Y. Grin, and F. Steglich, "Interplay of superconductivity and structural phase transition in the clathrate Ba_6Ge_{25}," *Phys. Rev. B*, vol. 70, p. 174512, 2004.

[157] W. Carrillo-Cabrera, H. Borrmann, S. Paschen, M. Baenitz, F. Steglich, and Y. Grin, "Ba_6Ge_{25}: Low-temperature Ge-Ge bond breaking during temperature-induced structure transformation," *J. Solid State Chem.*, vol. 178, pp. 715 – 728, 2005.

[158] H. Kou, Y. Jiang, J. Li, S. Yu, and C. Wang, "Enhanced photoelectric performance of $Cu_{2-x}Se$ nanostructure by doping with In3+," *J. Mater. Chem.*, vol. 22, pp. 1950–1956, 2012.

[159] V. Glazov, A. Pashinkin, and V. Fedorov, "Phase equilibria in the Cu-Se system," *Inorg. Mater.*, vol. 36, pp. 641–652, 2000.

[160] T. Kanashiro, T. Ohno, M. Satoh, K. Okamoto, A. Kojima, and F. Akao, "Nuclear magnetic resonance and electrical conduction of copper chalcogenides," *Solid State Ionics*, vol. 3–4, pp. 327– 330, 1981.

[161] T. Kanashiro, Y. Kishimoto, T. Ohno, and Y. Michihiro, "NMR study of mobile ions in Cu_xSe and Cu_xS," *Solid State Ionics*, vol. 40–41, Part 1, pp. 308– 311, 1990.

[162] R. R. Gainov, A. V. Dooglav, I. N. Pen'kov, I. R. Mukhamedshin, N. N. Mozgova, I. A. Evlampiev, and I. A. Bryzgalov, "Phase transition and anomalous electronic behavior in the layered superconductor CuS probed by NQR," *Phys. Rev. B*, vol. 79, p. 075115, 2009.

[163] D. Brinkmann, "NMR studies of superionic conductors," *Prog. Nucl. Magn. Reson. Spectrosc.*, vol. 24, pp. 527–552, 1992.

[164] M. Horvatić and Z. Vučić, "Dc ionic conductivity measurements on the mixed conductor $Cu_{2-x}Se$," *Solid State Ionics*, vol. 13, pp. 117–125, 1984.

[165] Z. Vučić, D. Lovrić, J. Gladić, and B. Etlinger, "Copper and silver selenide crystal growth rate measurements as a method for determination of ionic conductivity," *J. Crystal Growth*, vol. 263, pp. 590–599, 2004.

[166] R. Bömer, K. Jeffrey, and M. Vogel, "Solid-state Li NMR with applications to the translational dynamics in ion conductors," *Prog. Nucl. Magn. Reson. Spectrosc.*, vol. 50, pp. 87–174, 2007.

[167] A. A. Voskanyan, P. N. Inglizyan, S. P. Lalykin, I. A. Plyutto, and Y. M. Shevchenko, "Electrical properties of copper selenide," *Sov. Phys. Semicond.*, vol. 12, pp. 1251–1253, 1978.

[168] Y. Zhang, Y. Wang, L. Xi, R. Qiu, X. Shi, P. Zhang, and W. Zhang, "Electronic structure of antifluorite Cu_2X (X = S, Se, Te) within the modified Becke-Johnson potential plus an on-site coulomb U," *J. Chem. Phys.*, vol. 140, p. 074702, 2014.

[169] D. Jerome, C. Ryter, H. J. Schulz, and J. Friedel, "Si:P revisited: Electronic structure observed by magnetic resonance," *Philos. Mag. B*, vol. 52, pp. 403–417, 1985.

[170] X.-L. Qi and S.-C. Zhang, "Topological insulators and superconductors," *Rev. Mod. Phys.*, vol. 83, pp. 1057–1110, 2011.

[171] M. Z. Hasan and C. L. Kane, " Colloquium : Topological insulators," *Rev. Mod. Phys.*, vol. 82, pp. 3045–3067, 2010.

[172] S. Lee, J. In, Y. Yoo, Y. Jo, Y. C. Park, H.-J. Kim, H. C. Koo, J. Kim, B. Kim, and K. L. Wang, "Single crystalline β-Ag_2Te nanowire as a new topological insulator," *Nano Lett.*, vol. 12, pp. 4194–4199, 2012.

[173] A. A. Sirusi, S. Ballikaya, J.-H. Chen, C. Uher, and J. H. Ross, Jr., "Band ordering and dynamics of $Cu_{2-x}Te$ and $Cu_{1.98}Ag_{0.2}Te$," *J. Phys. Chem. C*, vol. 120, pp. 14549–14555, 2016.

[174] R. A. Yakshibaev, N. N. Mukhamadeeva, and R. F. Almukhametov, "Phase transformations and ionic transport in the $Cu_{2-\delta}Te$ superionic conductor," *Phys. Status Solidi (a)*, vol. 108, pp. 135–141, 1988.

[175] N. Bloembergen, E. M. Purcell, and R. V. Pound, "Relaxation effects in nuclear magnetic resonance absorption," *Phys. Rev.*, vol. 73, pp. 679–712, 1948.

[176] H. Günther, *NMR spectroscopy: Basic Principles, Concepts and Applications in Chemistry*. Siegen, Germany: Wiley-VCH, 2013.

[177] D. Koumoulis, T. C. Chasapis, B. Leung, R. E. Taylor, C. C. Stoumpos, N. P. Calta, M. G. Kanatzidis, and L.-S. Bouchard, "Site-specific contributions to the band inversion in a topological crystalline insulator," *Adv. Electron. Mater.*, vol. 1, p. 1500117, 2015.

[178] B. Njegic, E. Levin, and K. Schmidt-Rohr, "^{125}Te NMR chemical-shift trends in PbTe–GeTe and PbTe–SnTe alloys," *Solid State Nucl. Mag.*, vol. 55-56, pp. 79–83, 2013.

[179] B. Nowak and D. Kaczorowski, "NMR as a probe of band inversion in topologically nontrivial half-Heusler compounds," *J. Phys. Chem. C*, vol. 118, pp. 18021–18026, 2014.

APPENDIX A

FIRST APPENDIX

A.1 Hall Measurements

In this thesis, for some of the materials instead of using the PPMS, I used our superconducting NMR magnet to measure the Hall coefficients. The magnetic field was measured by a calibrated Hall sensor. The calibration was done by measuring the voltage for 3 different external fields. The results showed a clear linear dependence of voltage vs field. I found that using this strong field could be an efficient and accurate way to do such measurements.

Figure A.1 shows the schematic instrumentation of the system. To remove the longitudinal voltage due to the misalignment of wires for measuring the Hall voltage (V), we used a decade resistance box. In this system, the currents were sent in both directions and the averaged-voltage was used to calculate the Hall coefficient. The voltages were recorded using a Keithley 181 Nanovoltmeter. Moreover, by changing the sample position vertically in the NMR magnet, we were able to apply different magnetic fields. Since we have a persistent superconducting magnet, by knowing the position of the sample in the magnet we don't need to measure the field again. Thereby, the Hall voltages were obtained in different fields. Having a sample thickness (t), and plotting V vs B we can derive the Hall coefficient ($R_H = Vt/(IB)$), where I is the current.

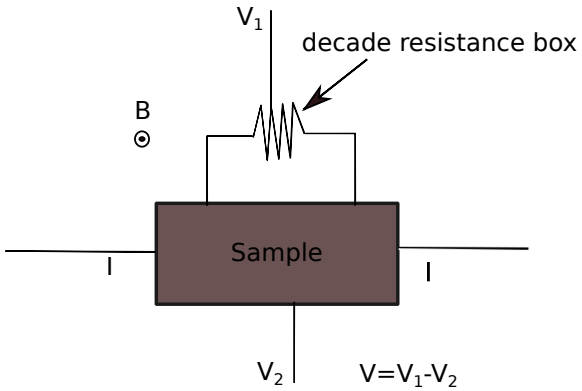

Figure A.1: Schematic depiction of the Hall coefficient measurement system.